Josephson effects in topological superconductors

Inaugural-Dissertation

zur Erlangung des Doktorgrades
der Mathematisch-Naturwissenschaftlichen Fakultät
der Heinrich-Heine-Universität Düsseldorf

vorgelegt von

Albert Iks
aus Alekseewka

Düsseldorf, Oktober 2021

Aus dem Institut für Theoretische Physik, Lehrstuhl IV
der Heinrich-Heine-Universität Düsseldorf

Gedruckt mit der Genehmigung der
Mathematisch-Naturwissenschaftlichen Fakultät
der Heinrich-Heine-Universität Düsseldorf

Berichterstatter:

1. Prof. Dr. Reinhold Egger

2. PD Dr. Hermann Kampermann

Tag der mündlichen Prüfung: 07.12.2021

Abstract

In the last decades major progress in experimental solid state physics was achieved, which kindled increasing interest in research and possible applications. Topological superconductors present a platform to observe Majorana fermions and offer various interesting applications, one of them being quantum computers.

We introduce the concept of topological superconductors, this includes superconductivity, topology and their creation. Additionally a formalism to analyze various junctions is introduced.

We are going to use this formalism for various junctions and models for topological superconductors. We start with a junction of a topological and non topological superconductor, a quantum dot is put in between to allow a supercurrent through the junction. For the topological superconductor a model, that allows analytical insights, is used. Afterwards we use a model for the topological superconductor, that is closer to experiments, but needs numerical calculations. Before we check the changes to the junction with this model, we discuss some general properties of the model and analyze a simpler junction first.

The next junction we discuss, has a different focus. Instead of the supercurrent we are going to focus on the states of the boundary of the wires, configurations with even and odd parity are connected through the topological superconductor and give us an interesting platform to study bound states.

Afterwards we dive deeper into models closer to experiments for topological superconductors. We look at our approach to analyze the junctions and summarize interesting and useful properties. Using these properties we try to get some analytical understanding beyond the numerical calculations. We apply this method on different models and discuss some junctions including these models afterwards.

Zusammenfassung

In den letzten Jahrzehnten wurde großer Fortschritt in der experimentellen Festkörperphysik erreicht, dies entfachte ein wachsendes Interesse in der Forschung und für mögliche Anwendungen. Topologische Supraleiter bieten eine Plattform, um Majorana Fermionen zu beobachten and bieten verschiedene interessante Anwendungen, eine davon sind Quantencomputer.

Das Konzept von topologischen Supraleitern wird eingeführt, dies beinhaltet Supraleitung, Topologie und ihre Umsetzung. Zusätzlich wird ein Formalismus, zum analysieren von Kontakten, eingeführt.

Dieser Formalismus wird für verschiedene Kontakte und Modelle für topologische Supraleiter angewendet. Es wird mit einem Kontakt zwischen einem topologischen und nicht topologischen Supraleiter begonnen, ein Quantenpunkt wird zwischen den beiden Leitern eingefügt, um einen supraleitenden Strom durch den Kontakt zu erlauben. Für den topologischen Supraleiter wird ein Modell, dass analytische Erkenntnisse erlaubt, verwendet. Danach wird ein Modell für den topologischen Supraleiter verwendet, dass näher an Experimenten is, jedoch numerisch gelöst werden muss. Bevor die Änderungen im Kontakt durch das Modell untersucht werden, werden zuerst einige allgemeine Eigenschaften des Modells besprochen und ein einfacherer Kontakt analysiert.

Der darauf folgende Kontakt, der besprochen wird, hat einen anderen Fokus. Anstelle des supraleitenden Stromes wird sich auf die Grenzzustände der Drähte konzentriert, Konfigurationen mit gerader und ungerader Parität sind durch den topologischen Supraleiter verbunden und liefern eine interessante Plattform zur Untersuchung von Grenzzuständen.

Danach wird sich mehr in Modelle näher an Experimenten für topologische Supraleiter vertieft. Es wird die Herangehensweise zur Analyse der Kontakte betrachtet und interessante und nützliche Eigenschaften werden zusammengefasst. Unter Verwendung dieser Eigenschaften wird versucht analytische Erkenntnisse, die über die numerischen Berechnungen hinausgehen, zu erhalten. Diese Methode wird für verschiedene Modelle angewendet und anschließend werden Kontakte, die diese Modelle enthalten, besprochen.

Contents

Chapter 1

Introduction

In this work we are going to discuss various topological Josephson junctions, this includes different models describing topological superconductors and various junctions utilizing them. In the last decades major progress in experimental solid state physics was achieved, this kindled increasing interest in research and possible applications. One of those applications is quantum computation and topological superconductors present a possibility to realize a quantum computer.

We are going to introduce the concept of superconductivity and it's special properties, the two big phenomena are that electrical resistance disappears and the magnetic field inside the superconductor is ejected. The theoretical description of superconductivity has evolved over time, the BCS (Bardeen-Cooper-Schrieffer) theory proposed in 1957, still describes the phenomenon of superconductivity well. Electrons form so called Cooper pairs because of electron lattice interactions and are effectively bosons. Additional to the BCS theory we introduce the Ginzburg-Landau theory. It doesn't contradict the BCS theory, instead they compliment each other.

The fundamental properties of a superconductor itself are interesting and serve different possible applications. the properties of superconductors are rather strong, for example Cooper pairs outside a superconducting material do not immediately break down, instead they slowly break down through scattering processes. A Josephson junction is a junction of two superconducting wires, which are separated by a small insulating layer. Even without an applied voltage Cooper pairs can tunnel between the two superconductors. The Josephson effect is separated between the DC Josephson effect without an applied voltage and the AC Josephson effect with an applied voltage. We will focus on the DC Josephson effect in this work. After introducing the Josephson effect, we introduce a theoretical description for tunneling processes between junctions of different leads.

After introducing superconductivity, we describe the concept of topology in physics. In mathematics topology engages with objects, that under continuous deformation preserve certain properties. This concept can be transferred to physics. For this we first introduce the adiabatic theorem, which describes, that the state of a system stays in the same state, as long as the Hamilton operator changes slowly in time. Next we introduce the Berry phase. The completion of a full cycle of an adiabatic transport results in a geometric phase, the so called Berry phase. With the Berry phase we define the Berry potential and Berry curvature. Finally we define a topological invariant, the Chern number, which is defined as a surface integral of the Berry curvature.

In Sec. 2.3 we introduce Topological superconductors, to describe them we need to introduce Majorana fermions. Majorana fermions are quasi particles, that are their own anti particles. A normal fermion can be described as a combination of two Majorana fermions. The Kitaev chain is a simple model proposed by Kitaev, where one can intuitively observe Majorana fermions. It is a simple 1D chain of spinless fermions, which can be described as pairs of Majorana fermions. Changing the parameters of the system, the Majorana fermions prefer different pairings. The Majorana fermions at the ends of the chain end up unpaired, they can be combined to a non localized zero energy Majorana mode. A possible way to realize this chain is the proximity effect, a superconductor is placed next to a semiconducting wire, the Cooper pairs can move to the semiconductor and don't immediately break down, as a result the semiconductor shows superconducting properties. Applying a Zeeman field allows us to separate the spins and we end up with an effectively spinless topological superconductor.

To analyze our Josephson junctions, we introduce the Keldysh formalism. It is a strong method, that allows the study of systems in non equilibrium. Part of this method is the determination of Green's functions. As we are going to focus on Josephson junctions in equilibrium, we introduce the Matsubara Green's functions, which are more compact. It is easy to switch between Matsubara and Keldysh Green's functions.

After finishing the introduction of concepts, we are going to need, we start the discussion of various topological Josephson junctions.

The first junction we start with in Sec. 3.1, is a junction made of a conventional superconductor, a spinless topological superconductor and a quantum dot in between. A local magnetic field is on the quantum dot to allow spin flipping. For the analysis of the interactions in the junction different perturbative approximations are used, including a Schrieffer-Wolff transformation. To compare our results, a mean field approximation is used, which we then numerically analyze.

The next section, Sec. 3.2, engages with spinful topological superconductors. We introduce a model for the spinful topological superconductor and take a look at the conditions, that determine if the superconductor is in the topological phase. Afterwards we go back to the Josephson junction made out of a conventional superconductor and a topological superconductor. Now with the spinful topological superconductor we observe, how the junction behaves during the transition from the topological trivial phase to the topological non trivial phase. Finally we take a look at the S-QD-TS junction again, but this time with a spinful topological superconductor.

The next junction we discuss, is the S-TS-S junction in Sec. 3.3. A spinless topological superconductor is coupled to a conventional S-S Josephson junction. As in the previous parts discussed, the current between a superconducting lead and a spinless topological superconducting lead is going to be suppressed, but because of the different parities of topological trivial and non trivial leads, interesting and useful things might be observed in this setup, specifically the reflections at the surfaces, which can resonate and form a standing wave, the so called Andreev bound states. We do an approximation to the atomic limit, to analyze this model. We look at the dynamics of the system in regards to the largest energy scale of interest. After rescaling the equations, we calculate the energy of the Andreev bound states and evaluate the equations.

In Sec. 4 we focus on spinful Josephson junctions and introduce more models for their description. The calculations for the spinful model are done numerically, we try to get some analytical understanding of the models. For this we first summarize interesting and useful properties of the boundary Green's function method. Afterwards we take a look at the model for the spinful topological superconductor and try to get some analytical insights.

In Sec. 4.3 we expand the model for the spinful topological superconductor from a single channel nanowire to a multi channel nanowire, specifically a two channel wire. As previously mentioned, calculations with the spinful model tend to be done numerically, restricting our observations to the two channel model, allows us to observe multichannel behavior, while preventing polynomials from getting too large, allowing us to still work with the model similarly as in the part for the single channel model.

After working with proximity effect induced topological superconductors, we also introduce a model for TRITOPS nanowires, time reversal invariant topological superconducting nanowires, it is a variation of the previously discussed model, where during the creation of the nanowire, time reversal symmetry is not broken. Models for a single channel and a two channel wire are introduced and analyzed with the same method as in the previous parts.

Finally in Sec. 4.5 we discuss different junctions using the introduced models. The first junction we study is a junction formed of three spinful topological superconductors with a variable angle for the third lead. Using the boundary Green's function, we rewrite the Hamiltonian and using the previously gained insights into the model, we further simplify the problem. We determine the Andreev bound states and gain insight into the current phase relation corresponding to the angle between the leads. The second junction we discuss, is a junction made out of a TRITOPS and a spinful topological superconductor. We allow a relative angle between the directions of the spin-orbit fields and similar to the previous junctions we discuss our results corresponding to this angle. We assume the wires are deep in the topological regime and are therefore able to do some simplifications. We calculate the Andreev bound states again and are able to gain insights for the junction related to the angle between the spin-orbit couplings.

Chapter 2

Fundamental principles

In this chapter we introduce fundamental principles required to understand the procedures and interpretations in the following chapters. Specifically we want to be able to discuss topological superconducting junctions. For this we introduce the concept of superconductivity first, this includes general phenomena and theoretical descriptions. The Josephson effect is one of them and a major reason for our interest in topological superconducting junctions. The other major reason are Majorana fermions, they possess unique properties and topological superconductors provide a platform to observe them, combine this with the general progress in solid state physics in the last decades and the possible applications like quantum computing, the importance and general interest in topological superconductors is explained. We introduce the concept of topology in physics, afterwards we introduce topological superconductors and also the formalism to examine topological junctions. For the topological superconductors we introduce the basic model of the Kitaev chain and discuss how to realize it. For the formalism we start with the extensive Keldysh formalism and introduce the simpler Matsubara formalism afterwards. For the problems we are going to examine, the Matsubara formalism is enough, the reason to introduce both is how easy it is to switch between both of them. This allows us to use known results for both. To examine the interaction in Josephson junction, perturbation theory and related concepts are introduced.

2.1 Superconductors

The effect of superconductivity was first observed in 1911 by H. Kamerlingh Onnes and has been the research subject of many scientists since then [5]. In the 1950s and 1960s the theoretical picture started to become satisfactory and sufficiently complete. We take a look at the phenomena of superconductivity and their theoretical description.

2.1.1 Phenomena

There are two major phenomena that can be observed. The phenomena that K. Onnes observed [5], was that the electrical resistance of different metals disappeared, when the temperature falls below a critical temperature T_c dependent on the material. Therefore one property of superconductivity is perfect conductivity.

The other phenomena was observed by Meissner and Ochsenfeld in 1933 [6]. they observed that additionally to the perfect conductivity, magnetic fields are prevented from entering the superconductor. When the temperature falls below T_c,

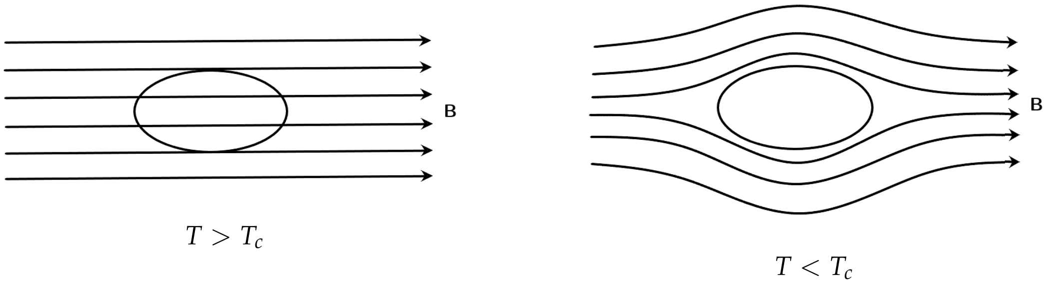

FIGURE 2.1: Figures show the Meissner effect. In the left figure the temperature T is above the critical temperature T_c and the sample is not superconducting and the magnetic field goes normally through the sample. In the right figure the temperature T is below the critical temperature T_c and the sample is superconducting and the magnetic field is stopped from entering the sample and goes around it.

the magnetic field inside the sample is ejected. This also implies, that the superconductivity can be destroyed with a sufficiently strong magnetic field. The second property of superconductivity is perfect diamagnetism.

2.1.2 BCS Theory

The theoretical description of superconductivity evolved over the decades following the initial discovery. The BCS (Bardeen-Cooper-Schrieffer) theory was proposed in 1957 by Bardeen, Cooper and Schrieffer [7], it is the first microscopic theory for the description of superconductivity after its discovery. Once the temperature is low, fermions will start to form phase coherent pairs, if an attractive potential is present. The theory is valid for a general attractive potential, this attractive potential in superconductors is usually a result of electron lattice interactions and it is strong enough to overcome the repulsive Coulomb interaction. These so called Cooper pairs are either made of fermions with anti parallel spin, singlet, or with parallel spin, triplet. They have integer spin and are effectively bosons, this means they can occupy the same ground state and form a condensate. The operator for a singlet is

$$b_{\mathbf{k}} = c_{\mathbf{k}\downarrow} c_{-\mathbf{k}\uparrow} \tag{2.1}$$

with fermionic destruction operators c, wave vector $\mathbf{k}$, spins $\uparrow$,$\downarrow$ and the effective BCS Hamiltonian is [1]

$$H = \sum_{\mathbf{k}\sigma} \xi_{\mathbf{k}} c^\dagger_{\mathbf{k}\sigma} c_{\mathbf{k}\sigma} + \sum_{\mathbf{k}\mathbf{k}'} V_{\mathbf{k}\mathbf{k}'} c^\dagger_{\mathbf{k}\uparrow} c^\dagger_{-\mathbf{k}\downarrow} c_{-\mathbf{k}'\downarrow} c_{\mathbf{k}'\uparrow} \tag{2.2}$$

with $\xi_{\mathbf{k}} = \hbar^2 k^2 / 2m - \mu$, reduced Planck constant $\hbar$, chemical potential μ, electron mass m and

$$V_{\mathbf{k}\mathbf{k}'} = \begin{cases} -V_0 & , |\xi_{\mathbf{k}}|, |\xi_{\mathbf{k}'}| \leq \hbar\omega_c \\ 0 & , else \end{cases} \tag{2.3}$$

This is a simplified model for the attractive force induced by electron phonon interaction, which are below the limit energy $\hbar\omega_c$ corresponding to the Debye energy and constant field $V_0 > 0$. The mean field Hamiltonian is given by [2]

$$\begin{aligned} H_{MF} &= \sum_{\mathbf{k}\sigma} \xi_{\mathbf{k}} c^\dagger_{\mathbf{k}\sigma} c_{\mathbf{k}\sigma} - \sum_{\mathbf{k}} \Delta_{\mathbf{k}} c^\dagger_{\mathbf{k}\uparrow} c^\dagger_{-\mathbf{k}\downarrow} \\ &\quad - \sum_{\mathbf{k}} \Delta^*_{\mathbf{k}} c_{\mathbf{k}\downarrow} c_{-\mathbf{k}\uparrow} + \sum_{\mathbf{k}\mathbf{k}'} V_{\mathbf{k}\mathbf{k}'} \langle c^\dagger_{\mathbf{k}\uparrow} c^\dagger_{-\mathbf{k}\downarrow} \rangle \langle c_{\mathbf{k}'\downarrow} c_{-\mathbf{k}'\uparrow} \rangle, \qquad (2.4) \\ \Delta_{\mathbf{k}} &= - \sum_{\mathbf{k}\mathbf{k}'} V_{\mathbf{k}\mathbf{k}'} \langle c_{-\mathbf{k}'\downarrow} c_{\mathbf{k}'\uparrow} \rangle. \qquad (2.5) \end{aligned}$$

This mean field can be solved by a Bogoliubov transformation, for this the Hamiltonian is rewritten in matrix notation

$$\begin{aligned} H_{MF} &= \sum_{\mathbf{k}} \begin{pmatrix} c^\dagger_{\mathbf{k}\uparrow} & c_{-\mathbf{k}\downarrow} \end{pmatrix} \begin{pmatrix} \xi_{\mathbf{k}} & \Delta_{\mathbf{k}} \\ \Delta^*_{\mathbf{k}} & -\xi_{\mathbf{k}} \end{pmatrix} \begin{pmatrix} c_{\mathbf{k}\uparrow} \\ c^\dagger_{-\mathbf{k}\downarrow} \end{pmatrix} \\ &\quad + \sum_{\mathbf{k}} \xi_{\mathbf{k}} + \sum_{\mathbf{k}\mathbf{k}'} V_{\mathbf{k}\mathbf{k}'} \langle c^\dagger_{\mathbf{k}\uparrow} c^\dagger_{-\mathbf{k}\downarrow} \rangle \langle c_{\mathbf{k}'\downarrow} c_{-\mathbf{k}'\uparrow} \rangle \\ &= \sum_{\mathbf{k}} \mathbf{A}^\dagger_{\mathbf{k}} \mathbf{H}_{\mathbf{k}} \mathbf{A}_{\mathbf{k}} + const., \qquad (2.6) \end{aligned}$$

with

$$\mathbf{A}_{\mathbf{k}} = \begin{pmatrix} c_{\mathbf{k}\uparrow} \\ c^\dagger_{-\mathbf{k}\downarrow} \end{pmatrix}, \quad \mathbf{H}_{\mathbf{k}} = \begin{pmatrix} \xi_{\mathbf{k}} & \Delta_{\mathbf{k}} \\ \Delta^*_{\mathbf{k}} & -\xi_{\mathbf{k}} \end{pmatrix}. \qquad (2.7)$$

Using the unitary transformation

$$\mathbf{U}_{\mathbf{k}} = \begin{pmatrix} u_{\mathbf{k}} & -v_{\mathbf{k}} \\ v^*_{\mathbf{k}} & u^*_{\mathbf{k}} \end{pmatrix} \qquad (2.8)$$

diagonalizes the Hamiltonian with following condition

$$\mathbf{U}^\dagger_{\mathbf{k}} \mathbf{H}_{\mathbf{k}} \mathbf{U}_{\mathbf{k}} = \begin{pmatrix} E_{\mathbf{k}} & 0 \\ 0 & \tilde{E}_{\mathbf{k}} \end{pmatrix}. \qquad (2.9)$$

The solutions for u,v are

$$|u_{\mathbf{k}}|^2 = \frac{1}{2}\left(1 + \frac{\xi_{\mathbf{k}}}{E_{\mathbf{k}}}\right), \quad |v_{\mathbf{k}}|^2 = \frac{1}{2}\left(1 - \frac{\xi_{\mathbf{k}}}{E_{\mathbf{k}}}\right) \qquad (2.10)$$

and we get for the energies

$$E_{\mathbf{k}} = \sqrt{\xi^2_{\mathbf{k}} + |\Delta_{\mathbf{k}}|^2} = -\tilde{E}_{\mathbf{k}}. \qquad (2.11)$$

2.1.3 Ginzburg-Landau theory

The Ginzburg-Landau theory was initially proposed in 1950 and focuses on the superconducting electrons in contrast to the BCS theory [3]. A complex pseudo wave function ψ is introduced as a order parameter in Landau's general theory of second order phase transitions. This ψ describes the superconducting electrons and the local density of superconducting electrons is given by

$$n_S = |\psi(x)|^2, \qquad (2.12)$$

using a variation principle and an assumed series expansion of free energy in powers of ψ and $\nabla\psi$ with expansion coefficients α and β we get following differential equation for ψ [4]

$$\frac{1}{2m}\left(\frac{\hbar}{i}\nabla - \frac{e}{c}\mathbf{A}\right)^2 \psi + \beta|\psi|^2\psi = -\alpha(T)\psi, \tag{2.13}$$

which is analogous to the Schrödinger equation for a free particle with a non linear term with speed of light c, magnetic vector potential $\mathbf{A}$, electron mass and charge m,e and $\alpha(T)$ is temperature dependent. The corresponding supercurrent is given by

$$\mathbf{J}_S = \frac{e\hbar}{i2m}(\psi^*\nabla\psi - \psi\nabla\psi^*) - \frac{e^2}{mc}|\psi|^2\mathbf{A} \tag{2.14}$$

which corresponds to the quantum mechanical current expression of a particle with charge e and mass m. This formalism allows us to examine non linear effects of fields, which are strong enough to change n_S, and the spatial variation of n_S.

It is possible to derive the Ginzburg-Landau theory from the BCS theory, when the temperature T is close to the critical temperature T_c. The function ψ is directly proportional to the gap parameter Δ. Further ψ can be thought as a wave function of the center of mass motion of the Cooper pairs.

The Ginzburg-Landau theory introduces a characteristic length, the so called Ginzburg-Landau coherence length

$$\psi(T) = \frac{\hbar}{|2m\alpha(T)|^{1/2}}, \tag{2.15}$$

characterizing the distance over which $\psi(\mathbf{r})$ can vary without inordinate energy increase.

2.1.4 Josephson current

We consider a tunnel junction with two superconducting wires, which are separated by a small insulating layer and observe the superconducting current. We can observe even without an applied voltage, Cooper pairs can tunnel between the two superconductors and we can measure a current, which is dependent on the phase difference $\Delta\phi = \phi_L - \phi_R$ of the Ginzburg-Landau-phases of both superconductors [8]. The Josephson effect is separated into two cases, the DC Josephson effect without an applied voltage and the AC Josephson effect with an applied voltage. The DC Josephson current is given by [4]

$$I = I_c \sin(\Delta\phi) \tag{2.16}$$

with critical current I_c being the maximum possible supercurrent. Applying a voltage V results in a time dependent phase difference

$$\frac{d(\Delta\phi)}{dt} = \frac{2eV}{\hbar} \equiv \omega_J, \tag{2.17}$$

therefore we have a time dependent supercurrent with amplitude I_c and frequency ω_J where $\hbar\omega_J$ is the energy difference needed to transfer a cooper pair.

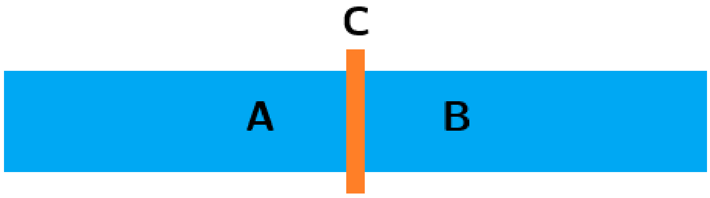

FIGURE 2.2: Diagram of a Josephson junction. The junction is made of two superconducting wires A and B, which are separated by an insulating layer C.

The free energy of the junction follows from this relation by integrating the work and we get

$$F = \int I_S V dt = \int I_S \frac{\hbar}{2e} d(\Delta\phi) = F_0 - E_j \cos(\Delta\phi), \tag{2.18}$$

where F_0 is a constant and $E_J = \hbar I_c/(2e)$ is the Josephson energy. We note, that we can only observe a super current, if the temperature scale is small compared to E_J/k_B because of thermal noise.

2.1.5 Tunnel Hamiltonian

We introduce a tunnel Hamiltonian describing junctions of different leads, we use gauge II, where chemical potential differences enter through time dependent phase factors in H_T.

We start with a single junction and generalize it afterwards. The tunnel Hamiltonian for a single junction is [9]

$$H_T(t) = \lambda e^{i\phi(t)/2} c_1^\dagger c_2 + h.c., \tag{2.19}$$

where $c_{j=1,2}$ are operators for the electrons near the left or right side of the junction, the hopping amplitude λ is assumed to be real valued without loss of generality, the phase difference is

$$\phi(t) = [\phi_1 - \phi_2](t) = \phi_0 + 2eVt/\hbar \tag{2.20}$$

with an applied current $eV = \mu_1 - \mu_2$. The normal transmission probability of the junction is given by

$$\tau = \frac{4\lambda^2}{(1+\lambda^2)^2} \tag{2.21}$$

with $0 \leq \tau \leq 1$.

To generalize it for an arbitrary number of leads $j = 1, ..., M$ we switch to Nambu representation. We describe the tunneling Hamiltonian with a time dependent tunnel Matrix $W(t)$, the diagonal elements don not contribute, $W_{jj} = 0$, and the off diagonal elements are given by

$$W_{jj'}(t) = \lambda_{jj'} \sigma_z e^{i\sigma_z[\phi_j(t) - \phi_{j'}(t)]/2} \tag{2.22}$$

with Pauli matrix σ_z and

$$W_{j'j}(t) = W_{jj'}^\dagger(t) \tag{2.23}$$

and we can write the Hamiltonian in Nambu representation as follows

$$H_T(t) = \frac{1}{2}\sum_{jj'}^{M} \Psi_j^\dagger W_{jj'}(t)\Psi_{j'}, \tag{2.24}$$

$$\Psi_j = \begin{pmatrix} c_j \\ c_j^\dagger \end{pmatrix}. \tag{2.25}$$

The current operator, describing the current through lead j, is

$$\hat{I}_j(t) = \frac{2e}{\hbar}\frac{\partial H_T(t)}{\partial \phi_j(t)} = i\sum_{j'\neq j} \Psi_j^\dagger(t)\sigma_z W_{jj'}(t)\Psi_{j'}(t). \tag{2.26}$$

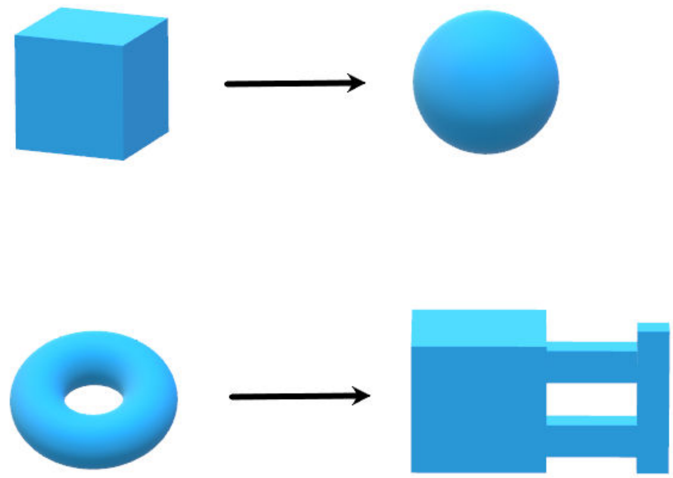

FIGURE 2.3: Example for a topological invariant. The figure shows objects that are continuously deformed into other objects. The topological invariant of the objects is the amount of holes, the objects in the upper panel have zero holes and the objects in the lower panel have one hole. The corresponding Cern numbers are zero and one.

2.2 Topology

Topology in mathematics engages with objects, that under continuous deformation, preserve certain properties, see Fig. 2.3. This concept can be applied to physics and as long as a material is not significantly changed, for example the material is broken, it will keep this topological property. We introduce in this part a method to calculate the topological invariant, namely the Chern number.

2.2.1 Adiabatic theorem

The first necessary foundation to introduce topological invariants is the adiabatic theorem. The adiabatic theorem in quantum mechanics states, that the state of a system stays in the same state, as long as the Hamilton operator $H(t)$ changes slowly in time. A state $\phi(t) = e^{i\alpha(t)}|n(t)\rangle$ in a system stays in the same state for

$$\left|\left\langle m(t) \left| \frac{d}{dt} H(t) \right| k(t) \right\rangle\right| \ll \frac{|E_k(t) - E_m(t)|}{\Delta T_{km}}, \tag{2.27}$$

with $m \neq k$, ΔT_{km} is the time needed to transition from state $|k(t)\rangle$ to state $|m(t)\rangle$, $E_k(t)$, $E_m(t)$ are the energies of the corresponding states and $\alpha(t)$ is a phase. The first proof for this theorem was given by Born and Fock in 1928 [17]. A descriptive example for this would be a pendulum that is slowly moved from one place to another place, as long as the pendulum is moved slow enough, the swinging motion of the pendulum won't be affected.

2.2.2 Berry phase

The completion of a full cycle of an adiabatic transport in a classic quantum mechanical system results in a geometric phase, the so called Berry phase [18]. We take a look at the phase $\alpha(t)$ introduced in the adiabatic theorem, we consider a time dependent Hamiltonian in the n-th eigenstate $\psi_n(x)$

$$H\psi_n(x) = E_n\psi_n(x), \tag{2.28}$$

with following phase factor

$$\Psi_n(x,t) = \psi_n(x)e^{-iE_nt/\hbar}. \tag{2.29}$$

The time dependent Hamiltonian has time dependent eigenvalues and eigenfunctions

$$H(t)\psi_n(x,t) = E_n(t)\psi_n(x,t). \tag{2.30}$$

Using the adiabatic theorem for a slowly changing Hamiltonian H, the particle in the n-th eigenstate will stay in the same state and get an additional phase

$$\Psi_n(x,t) = \psi_n(x,t)e^{-\frac{i}{\hbar}\int_0^t E_n(t')dt'}e^{i\gamma_n(t)}. \tag{2.31}$$

Additional to the geometric phase $\gamma_n(t)$, we get a dynamic phase

$$\theta_n(t) \equiv -\frac{1}{\hbar}\int_0^t E_n(t')dt', \tag{2.32}$$

which generalizes the factor $-E_nt/\hbar$ from a time independent case to a time dependent factor.

If we take the time dependent Schrödinger equation

$$i\hbar\frac{\partial\Psi}{\partial t} = H(t)\Psi \tag{2.33}$$

and insert the eigenfunctions, we get an expression for the time evolution of the geometric phase

$$\begin{aligned} i\hbar\left[\frac{\partial\psi_n}{\partial t}e^{i\theta_n}e^{i\gamma_n} - \frac{i}{\hbar}E_n\psi_n e^{i\theta_n}e^{i\gamma_n} + i\frac{d\gamma_n}{dt}\psi_n e^{i\theta_n}e^{i\gamma_n}\right] &= [H\psi_n]e^{i\theta_n}e^{i\gamma_n} \\ &= E_n\psi_n e^{i\theta_n}e^{i\gamma_n} \end{aligned} \tag{2.34}$$

with $\frac{\partial\psi_n}{\partial t} + i\psi_n\frac{d\gamma_n}{dt} = 0$. The scalar product with ψ_n results in

$$\frac{d\gamma_n}{dt} = i\left\langle \psi_n \middle| \frac{\partial\psi_n}{\partial t}\right\rangle. \tag{2.35}$$

We make the assumption, that the time dependency of $\psi_n(x,t)$ is the result of a parameter $R(t)$, which changes the equations as follows

$$\frac{\partial\Psi_n}{\partial t} = \frac{\partial\Psi_n}{\partial R}\frac{dR}{dt} \tag{2.36}$$

and

$$\frac{d\gamma_n}{dt} = i\left\langle \psi_n \middle| \frac{\partial\psi_n}{\partial R}\right\rangle\frac{dR}{dt} \tag{2.37}$$

and as a result we get for the geometric phase

$$\gamma_n(t) = i \int_0^t \left\langle \psi_n \middle| \frac{\partial \psi_n}{\partial R} \right\rangle \frac{dR}{dt'} dt' = i \int_{R_i}^{R_f} \left\langle \psi_n \middle| \frac{\partial \psi_n}{\partial R} \right\rangle dR, \tag{2.38}$$

with initial and final values R_i, R_f of $R(t)$. Because we are in the adiabatic regime, the Hamiltonian will be in it's initial state after a full cycle and $\gamma_n(T) = 0$ with period T. We generalize the assumption from a single time dependent parameter to N time dependent parameters

$$\frac{\partial \Psi_n}{\partial t} = \frac{\partial \Psi_n}{\partial R_1}\frac{dR_1}{dt} + \frac{\partial \Psi}{\partial R_2}\frac{dR_2}{dt} + ... + \frac{\partial \Psi_n}{\partial R_N}\frac{dR_N}{dt} = (\nabla_{\mathbf{R}} \Psi_N) \cdot \frac{d\mathbf{R}}{dt}, \tag{2.39}$$

with $\mathbf{R} \equiv (R_1, R_2, ..., R_N)$ and the corresponding gradient $\nabla_{\mathbf{R}}$. This changes the geometric phase to

$$\gamma_n(t) = i \int_{\mathbf{R}_i}^{\mathbf{R}_f} \langle \psi_n | \nabla_{\mathbf{R}} \psi_n \rangle \cdot d\mathbf{R}. \tag{2.40}$$

If we look at a full cycle, where the Hamiltonian returns to it's initial state, we get a closed line integral

$$\gamma_n(T) = i \oint \langle \psi_n | \nabla_{\mathbf{R}} \psi_n \rangle \cdot d\mathbf{R} \tag{2.41}$$

and this integral is in general non zero and is the so called Berry phase [19].

2.2.3 Berry potential and Berry curvature

We can rewrite the Berry phase as follows [19]

$$\gamma_n(T) = \oint d\mathbf{R} A_n(\mathbf{R}), \tag{2.42}$$

with the Berry potential

$$A_n(\mathbf{R}) = i \langle \psi_n | \nabla_{\mathbf{R}} | \psi_n \rangle. \tag{2.43}$$

This potential is dependent on the gauge and a tensor can be derived from it, the so called Berry curvature

$$\Omega^n_{\mu\nu}(\mathbf{R}) = \frac{\partial}{\partial R^\mu} A^n_\nu(\mathbf{R}) - \frac{\partial}{\partial R^\nu} A^n_\mu(\mathbf{R}) \tag{2.44}$$

and it is gauge invariant in contrast to the Berry potential. The vector Ω_n and tensors $\Omega^n_{\mu\nu}$ are related through the Levi-Cevita tensor $\Omega^n_{\mu\nu} = \epsilon_{\mu\nu\xi}\Omega^n_\xi$. For the three dimensional case we get following simple expression

$$\Omega_n(\mathbf{R}) = \nabla_{\mathbf{R}} \times A_n(\mathbf{R}). \tag{2.45}$$

If we compare this expression with a magnetic field, then Ω_n would be a magnetic flux density.

2.2.4 Chern number

We can now define a topological invariant, the Chern number is defined as a surface integral of the Berry curvature [21]

$$n_m = \frac{1}{2\pi} \int d^2\mathbf{k}\Omega_m. \tag{2.46}$$

This number corresponds to the number of monopoles and is an integer number. We get the total Chern number from summing up all occupied states

$$n = \sum_{m=1}^{N} n_m, \tag{2.47}$$

this number is invariant even with impurities between the bands, as long as the energy gap between the occupied and empty bands is finite.

2.3 Topological superconductors

Topological superconductors are interesting for various reasons. A topological property is a strong property that can't be removed without severely changing the material. With the possibility to observe Majorana fermions, they offer a potent platform to study them. The combination of Majorana fermions and topology offer an interesting platform for possible applications, one of them is quantum computing. In this part we introduce the concept of topological superconductors and how to realize them.

2.3.1 Majorana fermions

Majorana fermions were proposed by Ettore Majorana in 1937 [20], they are fermionic quasi particles which are their own anti particles. Majorana fermions are half fermions in a way, we get a fermionic state through the superposition of two Majorana fermions. This also works the other way around and we can write any fermion as a combination of two fermions.

Majorana fermions can appear as states in the middle of the energy gap and are called Majorana zero energy modes.These Majorana modes show non abelian statistics. Spinless topological superconductors, they only have one type of spin as active charge carriers, are suitable for the observation of Majorana fermions.

Majorana fermions are described by hermitian operators γ_j for quantum state j with $\gamma_j^\dagger = \gamma_j$, because they are also their own antiparticles the operators follow following relation $\gamma\gamma = 1$ [10].

Two Majorana fermions combined result in a fermion and the fermionic operators are as follows

$$
\begin{aligned}
c_j &= \frac{1}{2}(\gamma_{j,1} + i\gamma_{j,2}), \\
c_j^\dagger &= \frac{1}{2}(\gamma_{j,1} - i\gamma_{i,2}).
\end{aligned} \tag{2.48}
$$

We can invert these operators and get following Majorana operators

$$
\begin{aligned}
\gamma_{j,1} &= c_j^\dagger + c_j, \\
\gamma_{j,2} &= i(c_j^\dagger - c_j).
\end{aligned} \tag{2.49}
$$

These operators follow the anti commutation relation

$$
\{\gamma_i, \gamma_r\} = 2\delta_{ij}. \tag{2.50}
$$

2.3.2 Kitaev chain

The Kitaev chain is a simple model proposed by Kitaev, where we can intuitively observe Majorana modes [11]. The model describes a 1D tight binding chain with following Hamiltonian

$$H_{chain} = -\mu \sum_{i=1}^{N} n_i - \sum_{i=1}^{N-1} \left(t c_i^\dagger c_{i+1} + \Delta c_i c_{i+1} + h.c. \right), \tag{2.51}$$

with $h.c.$ hermitian conjugate, μ chemical potential, c_i electron annihilation operator at position i and $n_i = c_i^\dagger c_i$ the corresponding occupation operator. We assume that the superconducting gap Δ and the nearest neighbor hopping amplitude t are equal on every position. We have a chain of fermions, each composed of two Majorana fermions, where the fermions are coupled to their nearest neighbors. In this case we have a trivial superconductor. If we change the parameters $\mu = 0$ and $t = \Delta$, the Majorana fermions prefer a different pairing. Inserting Eq. (2.48) into our Hamiltonian results in the diagonalized Hamiltonian

$$H_{chain} = -it \sum_{i=1}^{N-1} \gamma_{i,2}\gamma_{i+1,1}. \tag{2.52}$$

The new fermions, the coupled Majorana fermions result in, are described as follows

$$\tilde{c}_i = \frac{1}{2}(\gamma_{i+1,1} + i\gamma_{i,2}) \tag{2.53}$$

and we get in the end for the Hamiltonian

$$H_{chain} = 2t \sum_{i=1}^{N-1} \tilde{c}_i^\dagger \tilde{c}_i. \tag{2.54}$$

This Hamiltonian also describes a 1D tight binding chain, where the fermions are described with pairs of Majorana fermions, the energy cost to create a fermion is $2t$. In this new chain the first and last Majorana operators $\gamma_{1,1}$ and $\gamma_{N,2}$ are missing from the Hamiltonian. We can combine them to a new non localized fermionic state

$$\tilde{c}_M = \frac{1}{2}(\gamma_{N,2} + i\gamma_{1,1}). \tag{2.55}$$

As this state doesn't contribute to the Hamiltonian, the energy required to occupy it is zero. This allows an odd number of electrons and therefore odd parity, which differs from conventional superconductors requiring an even number of electrons to form Cooper pairs and having a non degenerate ground state. The ground state of this new Hamiltonian is two fold degenerate and corresponds to the parity.

We used the special case $t = \Delta$ and $\mu = 0$ for the new pairing, this can be generalized, as long as the chemical potential is inside the energy gap $|\mu| < 2t$ the effect of new pairing still happens. In this generalized case the fermions are not fully localized and the localization of the Majorana edge states decays exponentially from the ends away. The two Majorana fermions form a zero energy mode only if the wire is long enough, such that they do not overlap.

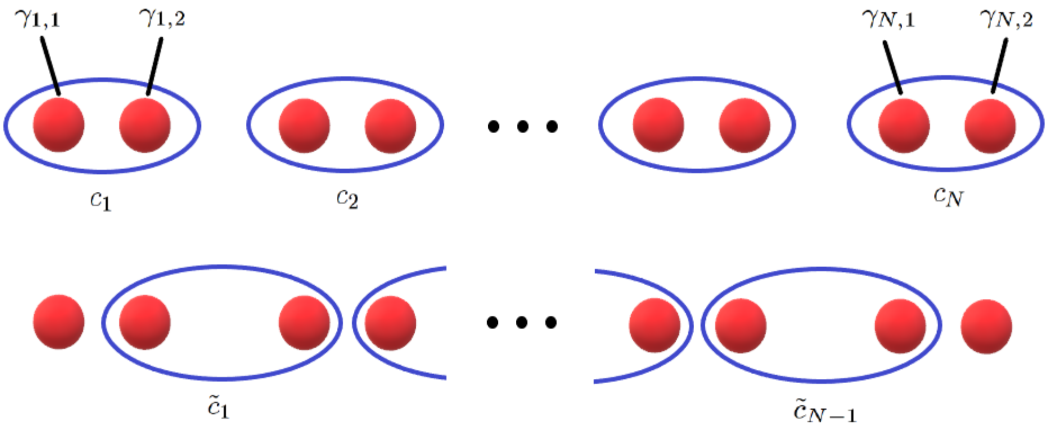

FIGURE 2.4: Sketch of Kitaev's model. The upper panel shows the 1D p-wave superconducting tight binding chain, each fermion at position i in the chain is a combination of two Majorana fermions $\gamma_{i,1}$ and $\gamma_{i,2}$. The lower panel shows the limit $t = \Delta$ and $\mu = 0$, the Majorana fermions of neighboring sites $\gamma_{i+1,1}$ and $\gamma_{i,2}$ combine to new fermions. As a result the two Majorana fermions at the ends are unpaired and can be combined to a non local zero energy mode.

2.3.3 Spinful topological superconductors

The Kitaev model gives us a possibility to realize Majorana fermions assuming we are able to translate this model into actual experiments. The model requires spinless fermions and p-wave superconductivity, which rarely appears in nature, thus we have to manufacture it ourselves. First proposals for possible realizations using proximity effect with topological insulators were made by L. Fu and C. L. Kane [12]. Later easier to realize approaches using semiconductors were proposed by Y. Oreg and R. M. Lutchyn [13], [14]. We use three things to get a topological superconductor, proximity effect, spin-orbit coupling and spin polarization.

The proximity effect or Holm-Meissner effect happens [15], when a superconductor is placed near a non-superconductor. The non-superconducting material will start showing weak superconducting characteristics over mesoscopic distances. The Cooper pairs of the superconductor can move to the non superconducting material, these pairs don't immediately break up instead they break up through scattering events over time.

Using a normal s-wave superconductor and a semiconductor wire, the semiconductor will show superconducting behavior because of the proximity effect. As a result of spin-orbit coupling the energy bands are separated by spin, no spinless regime is possible at this point. For this we apply a magnetic field on the semiconductor, this removes the crossing of the bands and opens up a gap, see Fig. 2.6, if the chemical potential μ is inside this gap, the wire is effectively spinless.

To finally get a spinless superconductor, we applied a magnetic field. If we start without a magnetic field and slowly increase it's strength, the wire will slowly transition from a spinful to a spinless wire. During this transition the wire can show topological behavior, while still not fully spinless.

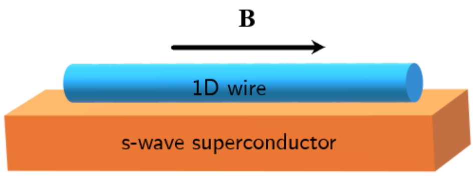

FIGURE 2.5: Simple setup for a topological superconductor. A 1D semiconducting wire is coupled to a conventional s-wave superconductor and a magnetic field along the wire is applied.

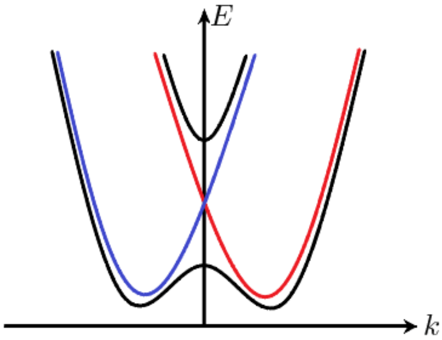

FIGURE 2.6: Band structure of the wire. Blue and red wires are bands with different spin before the magnetic field is applied. Black bands are the result of the applied magnetic field, a gap is opened up and we get a topological superconductor, if the chemical potential is inside this gap.

2.4 Keldysh formalism

The proposed formalism by Leonid Keldysh is useful for the description of the evolution of quantum mechanical systems in non equilibrium [23]. It is a powerful tool and part of it is the determination of Green's functions in non equilibrium. We introduce the Keldysh formalism and the simpler Matsubara formalism for systems in equilibrium. It is easy to switch between both formalisms and they are useful for the examination of tunnel contacts.

2.4.1 Keldysh contour

We consider a system, where the dynamics are described by a time dependent Hamiltonian $H(t) = H_0 + H'(t)$ with H_0 describing the unperturbed system and $H'(t)$ is a time dependent perturbation acting on it. In the past $t < 0$ the system is isolated and described by H_0 with an initial density ρ_0 and disturbed by en external time dependent field at $t > 0$. The Observable O with its corresponding operator $\hat{O}$ is time dependent in the Heisenberg picture [22]:

$$\hat{O}_H(t) = \hat{U}(0,t)\hat{O}\hat{U}(t,0) \tag{2.56}$$

and the expectation value is given by

$$O(t) = \langle \hat{O}_H(t) \rangle \equiv \mathrm{Tr}\{\hat{\rho}_0 \hat{O}_H(t)\} = \mathrm{Tr}\{\hat{\rho}_0 \hat{U}(0,t)\hat{O}\hat{U}(t,0)\}. \tag{2.57}$$

We get the evolution operator solving following equations

$$\begin{aligned} i\frac{d}{dt}\hat{U}(t,t') &= \hat{H}(t)\hat{U}(t,t'), \\ i\frac{d}{dt'}\hat{U}(t,t') &= -\hat{U}(t,t')\hat{H}(t') \end{aligned} \tag{2.58}$$

with $\hat{U}(t,t) = 1$. the evolution operator is given by

$$\hat{U}(t,t') = \begin{cases} \mathcal{T} e^{-i\int_{t'}^{t} d\bar{t}\hat{H}(\bar{t})}, & t > t' \\ \bar{\mathcal{T}} e^{-i\int_{t'}^{t} d\bar{t}\hat{H}(\bar{t})}, & t < t' \end{cases} \tag{2.59}$$

with the time ordering operator $\mathcal{T}$ and anti-chronological time ordering operator $\bar{\mathcal{T}}$.

2.4.2 Keldysh Green's function

The Green's function can be defined as follows [22]

$$G(r,t,r',t') = -i\langle \mathcal{T}\psi_H(r,t)\psi_H^{\dagger}(r',t')\rangle \tag{2.60}$$

with the field operator $\psi_H(r,t)$ of H, time ordering $\mathcal{T}$ and the averaging is done over the ground state. Using the evolution operator, we are able to express the Green's function instead with the field operators ψ_{H_0} of the unperturbed system H_0 and they are connected as follows

$$\psi_H(r,t) = \hat{U}(0,t)\psi_{H_0}\hat{U}(t,0). \tag{2.61}$$

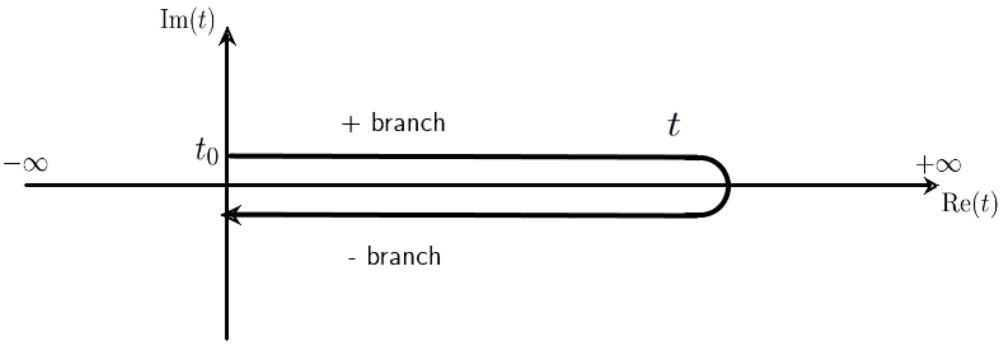

FIGURE 2.7: Keldysh contour example. A closed time path along the contour starting from t_0 along the imaginary and real time axis. The + branch and - branch are shown.

This allows us to describe the Green's function as in Eq. (2.60) and it can be expressed in terms of the non-interacting ground state and we get

$$G(r,t,r',t') = -i\frac{\langle\phi_0|\mathcal{T}\psi_{H_0}(r,t)\psi^\dagger_{H_0}(r',t')U(\infty,-\infty)|\phi_0\rangle}{\langle\phi_0|U(\infty,-\infty)|\phi_0\rangle}. \tag{2.62}$$

The time ordering is done along the Keldysh contour, we differentiate between the $+$ branch, which denotes the time evolution from our initial time t_0 until the time t at which we want to evaluate our system, and the $-$ branch, which denotes the backwards time evolution back to the starting point. The Green's function has four components for the different times t,t', when both are on the forward branch G^{++}, when both are on the backward branch G^{--}, for the case $t' > t$ on different branches it is G^{+-} and for the case $t' < t$ on different branches it is G^{-+}. The four components are related through following equation [16]

$$G^{++} + G^{--} = G^{+-} + G^{-+}, \tag{2.63}$$

therefore only three components are linearly independent and we can rewrite it as follows

$$G = \begin{pmatrix} G^{++} & G^{+-} \\ G^{-+} & G^{--} \end{pmatrix} = L\begin{pmatrix} 0 & G^A \\ G^R & G^K \end{pmatrix} L^{-1} \tag{2.64}$$

with Keldysh Matrix

$$L = \frac{1}{\sqrt{2}}\begin{pmatrix} 1 & 1 \\ -1 & 1 \end{pmatrix} \tag{2.65}$$

and the retarded Green's function G^R, advanced Green's function G^A and Keldysh Green's function G^K.

2.4.3 Matsubara Green's function

The Keldysh formalism is great to study non equilibrium problems, in the case of a system, that is in equilibrium, it is not necessary to utilize the full Keldysh formalism. We can switch to imaginary time formalism, which is also known as the Matsubara formalism [24]. As the name implies, we define a complex time $\tau = it$ and the imaginary Green's function is

$$G(r,\tau,r',\tau') = -\langle \mathcal{T}_\tau \psi(r,\tau)\psi^\dagger(r',\tau')\rangle \tag{2.66}$$

with the complex time ordering operator $\mathcal{T}_\tau$. For a time independent Hamiltonian the Green's function will depend on the time difference $\tau - \tau'$ instead of the individual times and we get

$$G(r,r',\tau) = -\langle \mathcal{T}_\tau \psi(r,\tau)\psi^\dagger(r',0)\rangle. \tag{2.67}$$

The switch between the Matsubara formalism and Keldysh formalism is simple, in imaginary time we only move along the complex time axis and we don't have the branches in real time of the Keldysh formalism. We can do following substitution to get the retarded/advanced Green's function from the Matsubara Green's function

$$i\omega_n \to \omega \pm i0^+, \tag{2.68}$$

where $+/-$ gives us the retarded/advanced Green's function, ω_n are the Matsubara frequencies and 0^+ is a positive infinitesimal. This substitution also works in the other direction, we can get the Matsubara Green's function from the retarded/advanced Green's function. With the retarded and advanced Green's function we can determine the Keldysh Green's function with following relation [9]

$$G^K(\omega) = f(\omega)(G^R(\omega) - G^A(\omega)) \tag{2.69}$$

with distribution function $f(\omega)$ for frequency ω

$$f(\omega) = 1 - 2n_F(\omega) = \tanh(\omega/2T), \tag{2.70}$$

which depends on the Fermi distribution n_F and temperature T.

2.5 Perturbation theory

Perturbation theory is used to study the effects of a small perturbation on an analytically solvable system. This could be an applied field on the system or interaction between different systems. The time dependent Schrödinger equation for an operator $\psi(t)$ is [25]

$$H(t)\psi(t) = i\hbar\frac{\partial\psi(t)}{\partial t} \tag{2.71}$$

and can be solved with the time evolution operator $U(t, t_0)$

$$\psi(t) = U(t, t_0)\psi_0. \tag{2.72}$$

The time evolution operator is given by

$$U(t, t_0) = \mathcal{T}e^{-\frac{i}{\hbar}\int_{t_0}^{t} dt' H(t')} \tag{2.73}$$

with time ordering operator $\mathcal{T}$. This expression can be treated by using a perturbative expansion of the time evolution operator, also called Dyson series

$$\begin{aligned} U(t, t_0) &= 1 - \frac{i}{\hbar}\int_{t_0}^{t_1} dt_1' \mathcal{T}H(t_1') + \frac{1}{2}\left(-\frac{i}{\hbar}\right)^2 \int_{t_0}^{t_1} dt_1' \int_{t_0}^{t_2} dt_2' \mathcal{T}H(t_1')H(dt_2') - \dots \\ &= \sum_{n=0}^{\infty} \frac{(-i)^n}{\hbar^n n!} \int_{t_0}^{t_1} \dots \int_{t_0}^{t_n} dt_1' \dots dt_n' \mathcal{T}(H(t_1') \dots H(t_n')). \end{aligned} \tag{2.74}$$

The leading term of this perturbation series is the first non zero term, depending on the problem this might require to deal with large time ordered products.

2.5.1 Wick's theorem

Wick's theorem, named after Gian-Carlo Wicks, is a method allowing us to reduce a expectation value of a time ordered product to a summation of time ordered products of two operators [26]. This allows us to rewrite expressions in such a way, that we can use the Keldysh Green's function. We consider an expression of the form

$$\langle \mathcal{T}(ABC \dots XYZ) \rangle \tag{2.75}$$

with time ordering operator $\mathcal{T}$ and field operators $A, B, \dots, Z$. Wick's theorem allows us to rewrite it as a sum of all possible products

$$\begin{aligned} \langle \mathcal{T}(ABC \dots XYZ) \rangle = &\langle \mathcal{T}(AB) \rangle \langle \mathcal{T}(CD) \rangle \dots \langle \mathcal{T}(YZ) \rangle \\ &\pm \langle \mathcal{T}(AC) \rangle \langle \mathcal{T}(BD) \rangle \dots \langle \mathcal{T}(YZ) \rangle \pm \dots \end{aligned} \tag{2.76}$$

The sign before the terms is determined by the amount of permutations needed. It is necessary for the average over the ground state to be done with an even number of operators or else the average will be zero. Depending on the operators, lengthy terms can be simplified to a short sum of the products of Green's functions.

2.5.2 Schrieffer-Wolff transformation

The Schrieffer-Wolff transformation is a unitary transformation used to project high energy excitations of a quantum many body system to an effective low energy subspace [27]. Starting with a time independent Hamiltonian

$$H = H_0 + V \tag{2.77}$$

with small perturbation V and unperturbed Hamiltonian H_0, whose eigenstates and eigenvalues are known. The transformation perturbatively diagonalizes the Hamiltonian to first order in perturbation V. This transformation is written as follows

$$H_{eff} = e^S H e^{-S} \tag{2.78}$$

with the generator S, for small V the generator is also small. This expression can be rewritten to

$$H_{eff} = H_0 + \frac{1}{2}[S, V] + \mathcal{O}(V^3) \tag{2.79}$$

with the condition for the generator

$$[H_0, S] = V. \tag{2.80}$$

The difficult part of this transformation is to get started, once S has been determined, the calculation is straight forward.

As a short example how it would look like, we take a look at a simple system with multiple energy levels. We project the system to the lowest energy state j and the transformation looks as follows

$$H_{eff} = H_{jj} + \sum_{n \neq j} H_{jn} \frac{1}{E - H_{nn}} H_{nj}, \tag{2.81}$$

where $H_{nm} = P_n H P_m$ and $H^\dagger_{nm} = H_{mn}$ with the projectors P, ground state energy E. For a system with multiple particles, the projectors would be given by the occupation of the corresponding energy levels.

Chapter 3

Josephson effect in junctions of conventional and topological superconductors

After discussing some fundamentals, we are going to apply them now. The following chapters are going to be dedicated to the publications in the appendix, we start with the first one A.1. We take a look at different setups for topological superconducting hybrid junctions and analyze the equilibrium Josephson current-phase relation.

3.1 S-QD-TS junction

The first junction we investigate is the S-QD-TS junction, with conventional s-wave superconductor (S), topological superconductor (TS) and an interacting spin-degenerate single-level quantum dot (QD). The main charge carrier in conventional s-wave superconductors are singlets, Cooper pairs made out of electrons with opposite spin. The main charge carrier in spinless topological superconductor are triplets, Cooper pairs made out of electrons with same spin. This means that for a Josephson current in a junction of a conventional superconductor and a topological superconductor to exist, the spin of an electron in the Cooper pairs needs to be flipped. To achieve this, a quantum dot and a Zeeman field are added in between the junction, see Fig. 3.1.

The Hamiltonian for the setup is given by

$$H = H_{\mathrm{S}} + H_{\mathrm{TS}} + H_{\mathrm{QD}} + H_{\mathrm{tun}} \tag{3.1}$$

with $H_{\mathrm{S/TS}}$ describing the semi infinite S/TS leads, H_{QD} describing the isolated dot between them and H_{tun} are the tunnel contacts. The quantum dot is an Anderson impurity with a single spin-degenerate energy level ϵ_0 with repulsive on-site interaction energy $U > 0$ [28]

$$H_{\mathrm{QD}} = \sum_{\sigma=\uparrow,\downarrow} \epsilon_0 \left(n_\sigma - \frac{1}{2} \right) + U n_\uparrow n_\downarrow - \mathbf{B} \cdot \mathbf{S}, \tag{3.2}$$

where $n_\sigma = d_\sigma^\dagger d_\sigma = 0, 1$ are the occupation numbers of the quantum dot with fermionic operators d_σ and $d_\sigma^\dagger$ for spin σ. We define

$$\mathbf{S}_{i=x,y,z} = \sum_{\sigma,\sigma'} d_\sigma^\dagger \left(\sigma_i\right)_{\sigma\sigma'} d_{\sigma'}, \tag{3.3}$$

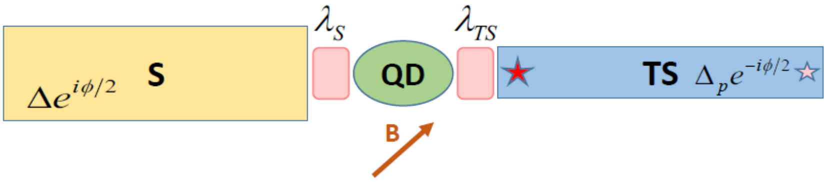

FIGURE 3.1: S-QD-TS geometry: S denotes a conventional s-wave BCS superconductor with order parameter $\Delta e^{i\phi/2}$, and TS represents a topologically nontrivial superconducting wire with Majorana bound states (shown as stars) and proximity-induced order parameter $\Delta_p e^{-i\phi/2}$. The interface contains a quantum dot (QD) corresponding to an Anderson impurity, connected to the S/TS leads by tunnel amplitudes $\lambda_{S/TS}$ (light red). The QD is also exposed to a local Zeeman field $\mathbf{B}$.

with standard Pauli matrices $\sigma_{x,y,z}$, such that $\mathbf{S}/2$ is a spin-1/2 operator. An external Zeeman field $\mathbf{B} = (B_x, B_y, B_z)$ acts on the quantum dot spin, it is independent from the field needed for the spinful nanowire proposal for TS wires [13], [14]. The leads are coupled to the quantum dot through the tunneling Hamiltonian as in Sec. 2.1.5, [29]

$$H_{\text{tun}} = \lambda_S \sum_{\sigma=\uparrow,\downarrow} \psi_\sigma^\dagger d_\sigma + \lambda_{TS} e^{-i\phi/2} \psi^\dagger d_\uparrow + \text{h.c.}, \tag{3.4}$$

where ψ_σ are the boundary fermion fields of the superconducting lead and ψ are fields of the effectively spinless topological superconducting lead. The S lead is described by the BCS model, see Sec. 2.1.2 and the TS lead is described by the Kitaev chain, see Sec. 2.3.2, for now. Without loss of generality, the Majorana bound state spin polarization direction is chosen as $\hat{e}_z$ and the tunnel amplitudes $\lambda_{S/TS}$ are real-valued, the tunnel amplitudes contain density of states factors for the respective leads. We use a gauge, such that the superconducting phase difference ϕ appears in the QD-TS tunneling term. The current flowing through the system is given by

$$\hat{I} = \frac{2e}{\hbar} \partial_\phi H_{\text{tun}}. \tag{3.5}$$

Because we are going to use the Matsubara boundary Green's functions, we do not have to specify $H_{\text{S/TS}}$ explicitly. The superconducting lead with energy gap Δ has following boundary Green's function [9]

$$\begin{aligned} g(\tau) &= -\langle \mathcal{T}_\tau \Psi_{\text{S}}(\tau) \Psi_{\text{S}}^\dagger(0) \rangle_0 = \beta^{-1} \sum_\omega e^{-i\omega\tau} g(\omega), \\ \Psi_{\text{S}} &= \begin{pmatrix} \psi_\uparrow \\ \psi_\downarrow^\dagger \end{pmatrix}, \quad g(\omega) = -\frac{i\omega\tau_0 + \Delta\tau_x}{\sqrt{\omega^2 + \Delta^2}}, \end{aligned} \tag{3.6}$$

where the expectation value $\langle \cdots \rangle_0$ refers to an isolated S lead, $\mathcal{T}_\tau$ denotes time ordering over complex time τ, ω runs over fermionic Matsubara frequencies $\omega = 2\pi(n + 1/2)/\beta$ with integer n, inverse temperature β and we define Pauli (unity) matrices $\tau_{x,y,z}$ (τ_0) in particle-hole space corresponding to the Nambu spinor Ψ_{S}. For the topological superconducting lead with proximity-induced gap Δ_p the boundary

Green's function of the low energy limit Kitaev chain is given by [9]

$$\begin{aligned} G(\tau) &= -\langle \mathcal{T}_\tau \Psi_{\mathrm{TS}}(\tau)\Psi^\dagger_{\mathrm{TS}}(0)\rangle_0, \quad \Psi_{\mathrm{TS}} = \begin{pmatrix} \psi \\ \psi^\dagger \end{pmatrix}, \\ G(\omega) &= \frac{1}{i\omega}\left(\sqrt{\omega^2+\Delta_p^2}\,\tau_0 + \Delta_p \tau_x\right), \end{aligned} \tag{3.7}$$

where the matrices $\tau_{0,x}$ act in the Nambu space defined by the spinor Ψ_{TS}.

We assume that U is the dominant energy scale and the single particle energy level is therefore at $\epsilon_0 \approx -U/2$. As a result low energy states with energy well below U are restricted to single occupation and the quantum dot acts like a magnetic impurity embedded in the TS junction. As the system is restricted to single occupancy for the low energy case, we project the system to the single occupancy case through a Schrieffer-Wolff transformation and the effective low-energy Hamiltonian splits up to

$$H_{\mathrm{eff}} = H_0 + H_{\mathrm{int}}, \quad H_0 = H_{\mathrm{S}} + H_{\mathrm{TS}} - \mathbf{B}\cdot\mathbf{S}. \tag{3.8}$$

The interaction Hamiltonian can be written as

$$\begin{aligned} H_{\mathrm{int}} &= \frac{4}{U}\sum_{\sigma,\sigma'} \mathcal{Q}_{\sigma\sigma'}\eta^\dagger_\sigma \eta_{\sigma'}, \\ \mathcal{Q}_{\sigma\sigma} &= \frac{\sigma}{2}S_z, \quad \mathcal{Q}_{\sigma,-\sigma} = \frac{1}{2}S_{-\sigma}, \end{aligned} \tag{3.9}$$

where $S_\pm = S_x \pm iS_y$ and

$$\eta_\sigma = \lambda_S \psi_\sigma + \delta_{\sigma,\uparrow}\lambda_{TS} e^{i\phi/2}\psi. \tag{3.10}$$

The partition function is then given by

$$Z = \mathrm{Tr}\Big|_{\delta n=0}\left(e^{-\beta H_0}\mathcal{T}_\tau e^{-\int_0^\beta d\tau H_{\mathrm{int}}(\tau)}\right) \tag{3.11}$$

with $\delta n = \sum_\sigma n_\sigma - 1$ and $H_{\mathrm{int}}(\tau) = e^{\tau H_0} H_{\mathrm{int}} e^{-\tau H_0}$ with H_0 from Eq. (3.8) and the trace is over the Hilbert subspace we projected to. The partition function can be rewritten to

$$\begin{aligned} Z &= Z_0 \left\langle \mathcal{T}_\tau e^{-\beta \hat{W}} \right\rangle_0 = e^{-\beta F}, \\ \hat{W} &= \beta^{-1}\int_0^\beta d\tau H_{\mathrm{int}}(\tau), \\ Z_0 &= \mathrm{Tr}\Big|_{\delta n=0} e^{-\beta H_0} = e^{-\beta F_0}, \end{aligned} \tag{3.12}$$

where F is the free energy and the Josephson current is then given by the free energy $I = (2e/\hbar)\partial_\phi F$.

We consider the elastic cotunneling regime $\lambda_S\lambda_{TS} \ll \min\{\Delta, \Delta_p, U\}$, where perturbation theory in H_{int} is justified. To calculate the current we need an expression for the free energy, the cumulant expansion is given by

$$F - F_0 = W_0 - \frac{\beta}{2}\left(\langle \hat{W}^2\rangle_0 - W_0^2\right) + \mathcal{O}(W^3) \tag{3.13}$$

with $W_0 = \langle \hat{W}\rangle_0$. Inserting our interaction Hamiltonian, we can use Wick's theorem from section 2.5.1 to determine the contractions and they are expressed in terms of boundary Green's functions matrix elements

$$\begin{aligned}\langle \mathcal{T}_\tau \eta_\sigma(\tau)\eta^\dagger_{\sigma'}(0)\rangle_0 &= \delta_{\sigma\sigma'}\Big[\lambda_S^2\langle \mathcal{T}_\tau \psi_\sigma(\tau)\psi^\dagger_\sigma(0)\rangle_0 + \\ &+ \delta_{\sigma,\uparrow}\lambda_{TS}^2\langle \mathcal{T}_\tau \psi(\tau)\psi^\dagger(0)\rangle_0\Big]\end{aligned} \tag{3.14}$$

and similarly

$$\begin{aligned}\langle \mathcal{T}_\tau \eta_\sigma(\tau)\eta_{\sigma'}(0)\rangle_0 &= \delta_{\sigma,-\sigma'}\lambda_S^2\langle \mathcal{T}_\tau \psi_\sigma(\tau)\psi_{-\sigma}(0)\rangle_0 \\ &+ e^{i\phi}\delta_{\sigma\sigma'}\delta_{\sigma,\uparrow}\lambda_{TS}^2\langle \mathcal{T}_\tau \psi(\tau)\psi(0)\rangle_0.\end{aligned} \tag{3.15}$$

We can see $\partial_\phi\langle H_{\text{int}}\rangle_0 = 0$ and therefore the ϕ-independent terms W_0 and W_0^2 in Eq. (3.13) do not contribute to the Josephson current and the leading contribution is of second order in H_{int}. The Josephson current is then given by

$$\begin{aligned}I(\phi) &= -\beta^{-1}\partial_\phi\int_0^\beta d\tau_1 d\tau_2\langle \mathcal{T}_\tau H_{\text{int}}(\tau_1)H_{\text{int}}(\tau_2)\rangle_0 \\ &= -\frac{\kappa^2}{\beta}\int_0^\beta d\tau_1 d\tau_2\, g_{12}(\tau_1-\tau_2)G_{12}(\tau_1-\tau_2) \\ &\times\; ie^{i\phi}\sum_\sigma \sigma\langle \mathcal{T}_\tau \mathcal{Q}_{\sigma,\uparrow}(\tau_1)\mathcal{Q}_{-\sigma,\uparrow}(\tau_2)\rangle_0 + \text{h.c.},\end{aligned} \tag{3.16}$$

with the small dimensionless parameter

$$\kappa = \frac{4\lambda_S\lambda_{TS}}{U} \ll 1. \tag{3.17}$$

The boundary Green's function matrix elements are given by

$$\begin{aligned}g_{12}(\tau) &= -\frac{\Delta}{\beta}\sum_\omega \frac{\cos(\omega\tau)}{\sqrt{\omega^2+\Delta^2}}, \\ G_{12}(\tau) &= -\frac{\Delta_p}{\beta}\sum_\omega \frac{\sin(\omega\tau)}{\omega} \simeq -\frac{\Delta_p}{2}\,\text{sgn}(\tau).\end{aligned} \tag{3.18}$$

$|g_{12}(\tau)|$ is exponentially small unless $\Delta|\tau| < 1$. In particular, $g_{12}(\tau) \to -\delta(\tau)$ for $\Delta \to \infty$. Further for $B \ll \Delta$ with $B \equiv |\mathbf{B}|$, the magnetic impurity $(\mathbf{S})$ dynamics will be slow on time scales of order $1/\Delta$. This allows us to approximate the spin-spin correlators by their equal-time expressions

$$\lim_{\tau_1\to\tau_2}\langle \mathcal{T}_\tau \mathcal{Q}_{\sigma,\uparrow}(\tau_1)\mathcal{Q}_{-\sigma,\uparrow}(\tau_2)\rangle_0 = \frac{\sigma}{4}\text{sgn}(\tau_1-\tau_2)\langle S_+(\tau_1)\rangle_0. \tag{3.19}$$

We can now calculate the Josephson current and the current phase relation is given by

$$\begin{aligned}I(\phi) &= I_x\sin\phi + I_y\cos\phi, \\ I_{x,y} &= \frac{e\kappa^2\Delta_p}{2\hbar}\frac{B_{x,y}}{B}\tanh(\beta B).\end{aligned} \tag{3.20}$$

Even though Δ doesn't appear in the current, the calculations require it to be sufficiently large. Our expression for the current predicts anomalous supercurrents for the S-QD-TS setup. A finite Josephson current for vanishing phase difference ($\phi = 0$) can be observed [32], [33], [34]. Another way to view this effect as a φ_0-shift in the current-phase relation, $I(\phi) = I_c \sin(\phi + \varphi_0)$, an observation of this φ_0-junction behavior could then provide additional evidence for Majorana bound states [35]. Our equation shows, that the local magnetic field is required to have a finite B_y-component with $\hat{e}_z$ defining the Majorana bound state spin polarization direction. If $\mathbf{B}$ is aligned with $\hat{e}_z$, the supercurrent in Eq. (3.20) vanishes identically since s-wave Cooper pairs cannot tunnel from the S lead into the TS wire in the absence of spin flips [31]. Otherwise, the current phase relation is 2π-periodic and sensitive to the Majorana bound state through the peculiar dependence on the relative orientation between the Majorana bound state spin polarization ($\hat{e}_z$) and the local Zeeman field $\mathbf{B}$ on the QD. The fact that $B_y \neq 0$ (rather than $B_x \neq 0$) is necessary to have $\varphi_0 \neq 0$ can be traced back to our choice of real-valued tunnel couplings. Experiments for junctions between normal conducting leads and topological superconductors employing quantum dots can probe non local effects due to Majorana bound states [36–42]. For our junction Eq. 3.20 predicts a tunable anomalous supercurrent.

To compare our results, we do a mean-field analysis, which allows to go beyond the perturbative cotunneling regime. For this we need to define the Green's function of the quantum dot

$$G_d(\tau) = -\langle \mathcal{T}_\tau \Psi_d(\tau) \Psi_d^\dagger(0) \rangle, \quad \Psi_d^\dagger = (d_\uparrow^\dagger, d_\downarrow, d_\downarrow^\dagger, -d_\uparrow)^T. \tag{3.21}$$

Note that this notation introduces double counting, which implies that only half of the levels are physically independent. The mean-field Hamiltonian can be written in this Nambu bi-spinor basis

$$\begin{aligned}
\mathcal{H}_{\mathrm{MF}} &= \begin{pmatrix} \epsilon_\uparrow & \Delta_d & \alpha_d & 0 \\ \Delta_d^* & -\epsilon_\downarrow & 0 & \alpha_d \\ \alpha_d^* & 0 & \epsilon_\downarrow & \Delta_d \\ 0 & \alpha_d^* & \Delta_d^* & -\epsilon_\uparrow \end{pmatrix}, \\
\epsilon_\uparrow &= \epsilon_0 - B_z + U\langle n_\downarrow \rangle, \quad \epsilon_\downarrow = \epsilon_0 + B_z + U\langle n_\uparrow \rangle, \\
\alpha_d &= B_x + iB_y - U\langle d_\downarrow^\dagger d_\uparrow \rangle, \quad \Delta_d = U\langle d_\downarrow d_\uparrow \rangle.
\end{aligned} \tag{3.22}$$

The mean-field parameters appearing in Eq. (3.22) follow by solving the self-consistency equations

$$\begin{aligned}
\langle n_\uparrow \rangle &= \frac{1}{\beta} \sum_\omega G_{d,11}(\omega), \quad \langle n_\downarrow \rangle = \frac{1}{\beta} \sum_\omega G_{d,33}(\omega), \\
\langle d_\downarrow^\dagger d_\uparrow \rangle &= \frac{1}{\beta} \sum_\omega G_{d,13}(\omega), \quad \langle d_\downarrow d_\uparrow \rangle = \frac{1}{\beta} \sum_\omega G_{d,21}(\omega),
\end{aligned} \tag{3.23}$$

where the mean-field approximation readily yields

$$G_d(\omega) = \left[i\omega - \mathcal{H}_{\mathrm{MF}} - \Sigma_S(\omega) - \Sigma_{TS}(\omega) \right]^{-1}. \tag{3.24}$$

The self-energies $\Sigma_{S/TS}(\omega)$ have the following matrix representation due to the coupling of the QD to the S/TS leads

$$\Sigma_S = \Gamma_S \begin{pmatrix} g_{11} & -g_{12} & 0 & 0 \\ -g_{21} & g_{22} & 0 & 0 \\ 0 & 0 & g_{11} & -g_{12} \\ 0 & 0 & -g_{21} & g_{22} \end{pmatrix} \tag{3.25}$$

and

$$\Sigma_{\mathrm{TS}} = \Gamma_{TS} \begin{pmatrix} G_{11} & 0 & 0 & -G_{12}e^{-i\phi} \\ 0 & 0 & 0 & 0 \\ 0 & 0 & 0 & 0 \\ -G_{21}e^{i\phi} & 0 & 0 & G_{22} \end{pmatrix} \tag{3.26}$$

with the hybridization parameters $\Gamma_{S/TS} = \lambda^2_{S/TS}$. The Josephson current from Eq. (3.5) is obtained as follows

$$I(\phi) = -\frac{e}{\hbar\beta}\sum_{\omega} \frac{\partial_\phi \det\left[G_d^{-1}(\omega)\right]}{\det\left[G_d^{-1}(\omega)\right]}. \tag{3.27}$$

We now study different cases numerically, we set $\Delta_p = \Delta$ and consider the zero-temperature limit. To compare our results we first check the case $U = 0$. At low energy scales the self-energy $\Sigma = \Sigma_S + \Sigma_{TS}$ simplifies to

$$\Sigma \simeq \begin{pmatrix} \frac{2\Delta}{i\omega}\Gamma_{TS} & -\Gamma_S & 0 & -\frac{2\Delta}{i\omega}\Gamma_{TS}e^{-i\phi} \\ -\Gamma_S & 0 & 0 & 0 \\ 0 & 0 & 0 & -\Gamma_S \\ -\frac{2\Delta}{i\omega}\Gamma_{TS}e^{i\phi} & 0 & -\Gamma_S & \frac{2\Delta}{i\omega}\Gamma_{TS} \end{pmatrix}. \tag{3.28}$$

Andreev bound states with subgap energies are a result of multiple Andreev reflections, they occur between non superconducting and superconducting materials at energies less than the superconducting gap, an electron (hole) forms a Cooper pair in the superconductor with the retroreflection of a hole (electron) of opposite spin and velocity but equal momentum. The Andreev bound states spectrum of the S-QD-TS junction follows by solving a determinantal equation, $\det\left[G_d^{-1}(\omega)\right] = 0$. One finds a zero-energy pole which is related to the Majorana bound state and results from the $1/\omega$ dependence of $\Sigma_{TS}(\omega)$. Additionally we get finite-energy subgap poles for

$$i\omega \equiv E_A^{(\sigma_1=\pm,\sigma_2=\pm)} = \sigma_1\sqrt{\frac{b_0 + \sigma_2\sqrt{b_0^2 + 4c_0}}{2}}, \tag{3.29}$$

with the notation

$$\begin{aligned} b_0 &= \epsilon_\downarrow^2 + \epsilon_\uparrow^2 + 4\Gamma_{TS}\Delta + 2\Gamma_S^2 + 2|\alpha_d|^2, \\ c_0 &= -4\Gamma_{TS}\Delta\left(\epsilon_\downarrow^2 + \Gamma_S^2 + |\alpha_d|^2\right) - \epsilon_\uparrow^2\epsilon_\downarrow^2 \\ &\quad - \left(|\alpha_d|^2 - \Gamma_S^2\right)\left(|\alpha_d|^2 - \Gamma_S^2 - 2\epsilon_\uparrow\epsilon_\downarrow\right) \\ &\quad + 8\Delta\Gamma_S\Gamma_{TS}\mathrm{Re}\left(\alpha_d e^{i\phi}\right). \end{aligned} \tag{3.30}$$

Numerically exact results for $U = 0$ are compared to the analytical prediction (3.29). We first notice that, as expected, Eq. (3.29) accurately fits the numerical results in the atomic limit, see the left panel in Fig. 3.2. Deviations can be observed for larger values of $\Gamma_{S,TS}/\Delta$. However, as shown in the right panel of Fig. 3.2, rather good agreement is again obtained by rescaling Eq. (3.29) with a constant factor of the order of $(1 + \Gamma_{S,TS}/\Delta)$. For finite B_y, we find that the phase-dependent ABS spectrum is shifted with respect to $\phi = 0$. In fact, since the phase dependence of the subgap states comes from the term $\mathrm{Re}(\alpha_d e^{i\phi})$ in the atomic limit, see Eqs. (3.22) and (3.30), B_y can be fully accounted for in this limit by simply shifting $\phi \to \phi + \varphi_0$.

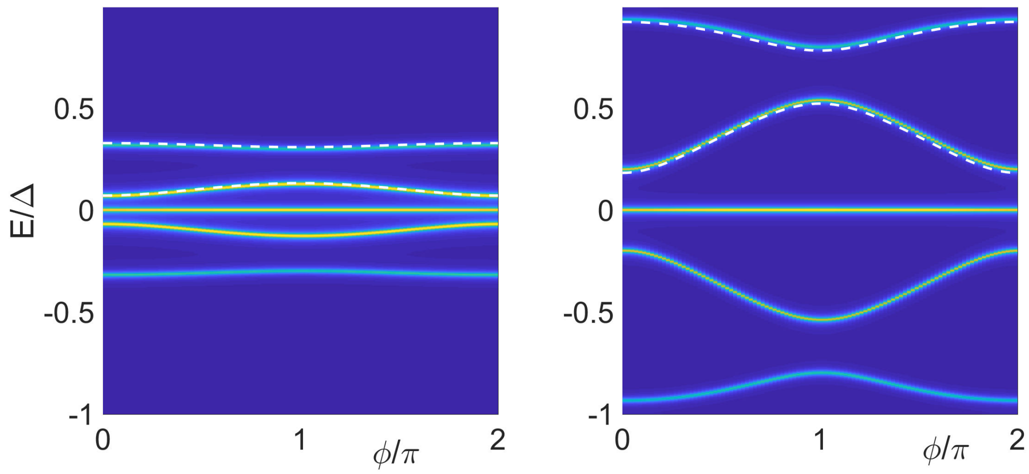

FIGURE 3.2: Phase dependence of the subgap spectrum of an S-QD-TS junction in the noninteracting case, $U = 0$. The TS wire is modeled from the low-energy limit of a Kitaev chain, and we use the parameters $B_y = 0$, $B_x = B_z = B/\sqrt{2}$, $\epsilon_0 = 0$, $\Delta_p = \Delta$, and $\Gamma_S = \Gamma_{TS} = \Gamma$. From blue to yellow, the color code indicates increasing values of the spectral density. The left (right) panel is for $\Gamma = 0.045\Delta$ and $B = 0.1\Delta$ ($\Gamma = B = 0.5\Delta$). Solid curves were obtained by numerical evaluation of Eq. (3.27). Dashed curves give the analytical prediction (3.29). In the right panel, the energies resulting from Eq. (3.29) have been rescaled by the factor $1 + \Gamma/\Delta$.

We thereby recover the φ_0-junction behavior discussed before for the cotunneling regime, see Eq. (3.20). Next we check the behavior for a finite U. For $B_y = 0$ we get zero junction behavior, which is in line with the results of Eq. (3.20) in the cotunneling regime. Further we encounter ϕ_0-junction behavior for $B_y \neq 0$ again, this suggests, that φ_0-junction behavior is very robust and extends also into other parameter regimes as long as the condition $B_y \neq 0$ is met. For a more detailed analysis see A.1.

3.2 Spinful nanowire model for the TS

We now want to know how the results of the S-QD-TS junction change, if we use the spinful nanowire model from Sec. 2.3.3, which allows us to connect closer to experimental parameters compared to the Kitaev chain, instead of the Kitaev chain. First we will observe the elementary case of an S-TS junction using the spinful nanowire model. The spinful nanowire model for TS wires is given by [30]

$$\begin{aligned}
H_{\mathrm{TS}} &= \frac{1}{2}\sum_j \left[\psi_j^\dagger \hat{h}\psi_j + \left(\psi_j^\dagger \hat{t}\psi_{j+1} + \mathrm{h.c.}\right)\right], \qquad (3.31)\\
\hat{h} &= (2t-\mu)\tau_z\sigma_0 + V_x\tau_0\sigma_x + \Delta_p\tau_x\sigma_0,\\
\hat{t} &= -t\tau_z\sigma_0 + i\alpha\tau_z\sigma_z,
\end{aligned}$$

where the lattice fermion operators $c_{j\sigma}$ for given site j with spin polarizations $\sigma =\uparrow,\downarrow$ are combined to the four-spinor operator $\psi_j = \left(c_{j\uparrow}, c_{j\downarrow}, c_{j\downarrow}^\dagger, -c_{j\uparrow}^\dagger\right)^T$. The Pauli matrices $\tau_{x,y,z}$ (and unity τ_0) act in Nambu space, while Pauli matrices $\sigma_{x,y,z}$ and σ_0 refer to spin. The following model parameters are chosen for the calculations, the lattice spacing is set to $a = 10$ nm, which results in a nearest-neighbor hopping $t = \hbar^2/(2m^*a^2) = 20$ meV with effective electron mass $m^* = 0.02m_e$, m_e electron mass and the spin-orbit coupling strength $\alpha = 4$ meV for InAs nanowires [30]. The proximity-induce pairing gap is again denoted by Δ_p, the chemical potential is μ, and the bulk Zeeman energy scale V_x is determined by a magnetic field applied along the wire. The topological nontrivial phase is realized under the following condition [13], [14]

$$V_x > V_x^c = \sqrt{\mu^2 + \Delta_p^2}. \tag{3.32}$$

The current through the junction depends on the local magnetic field $\mathbf{B}$ as before and additionally on the bulk Zeeman field V_x. The boundary Greens function for the spinful model needs to be calculated numerically [30].

Before we discuss the S-QD-TS case, we take a look at the S-TS junction. The transparency $\mathcal{T}$ close to the topological transition can be approximated with

$$\mathcal{T} = \frac{4(\lambda/t)^2}{[1 + (\lambda/t)^2]^2}, \tag{3.33}$$

where $t = 20$ meV is the hopping parameter in Eq. (3.31) and the tunnel coupling λ. We take a look at the current phase relation and study the critical current I_c as a function of $\mathcal{T}$ for the transition between the topologically trivial ($V_x < V_x^c$) and the nontrivial ($V_x > V_x^c$) regime. The critical current is strongly suppressed in the topological phase and slowly decreases moving deeper into the topological phase, see Fig. 3.3. This is in accordance with the results of the Kitaev chain, where the Josephson current is blocked [31], because of the different pairing, s-wave pairing in S and p-wave pairing in TS. There is a remaining finite supercurrent, which can still be observed for large values of V_x. This is a result of remaining s-wave pairing correlations in the spinful nanowire model. The kink like feature can be attributed to the rapid decrease of the Andreev bound states, this also suggests, that the continuum contributions mainly originate from s-wave pairing correlations, that are not particularly sensitive to the topological transition.

We return to the S-QD-TS junction and use the mean-field analysis again, replacing the boundary Green's function for the TS wire with the spinful nanowire model. Proceeding the same way as with the Kitaev chain, we discuss the results for certain parameters. We assume the local magnetic field $\mathbf{B}$ acting on the QD coincides with the bulk Zeeman field V_x in the TS wire, $\mathbf{B} = (V_x, 0, 0)$. For large values of $\Gamma_{S,TS}$, the critical current against V_x again shows a kink like feature at the phase transition, see Fig. 3.4. This kink can be traced back to the sudden drop of Andreev bound state contribution as well. The critical current gets suppressed in the topological phase similar to the S-TS junction, see A.1.

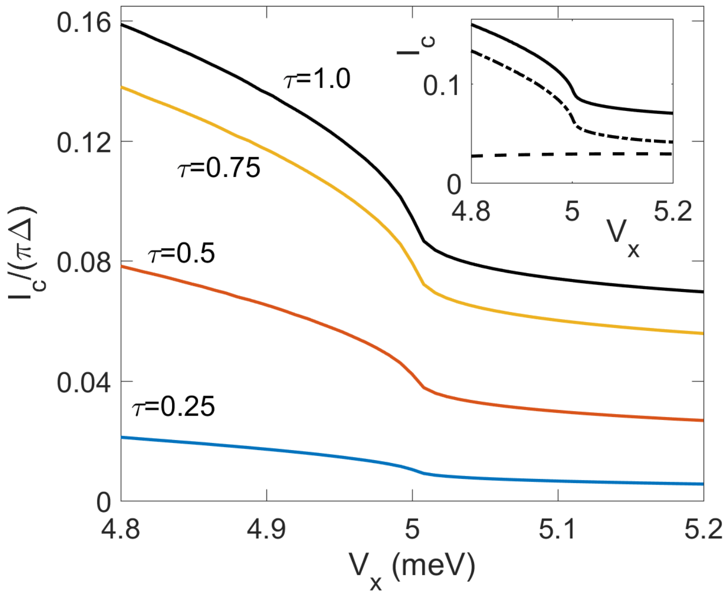

FIGURE 3.3: Main panel: Critical current I_c vs Zeeman energy V_x for an S-TS junction using the spinful TS nanowire model (3.31) for $\Delta_p = \Delta = 0.2$ meV, $\mu = 5$ meV, and different transparencies $\mathcal{T}$ calculated from Eq. (3.33). All other parameters are specified in the main text. Inset: Decomposition of I_c for $\mathcal{T} = 1$ into ABS (dotted-dashed) and continuum (dashed) contributions.

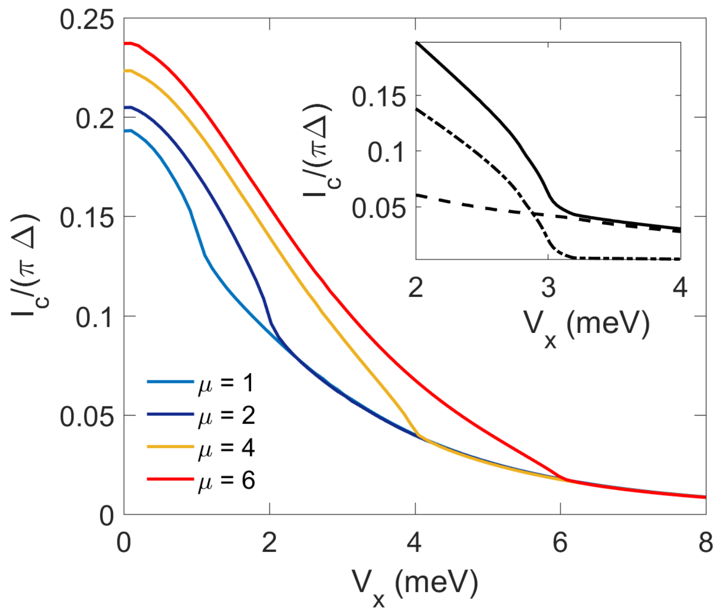

FIGURE 3.4: Main panel: Critical current I_c vs Zeeman energy V_x for S-QD-TS junctions from mean-field theory using the spinful TS nanowire model (3.31). Results are shown for several values of the chemical potential μ (in meV), where we assume $U = 10\Delta$, $\epsilon_0 = -U/2$, $\Delta_p = \Delta = 0.2$ meV, $\Gamma_S = 2\Gamma_{TS} = 9\Delta$, and $\mathbf{B} = (V_x, 0, 0)$. Inset: Detailed view of the transition region $V_x \approx V_x^c$ for $\mu = 3$ meV, including a decomposition of I_c into the ABS (dotted-dashed) and the continuum (dashed) contribution.

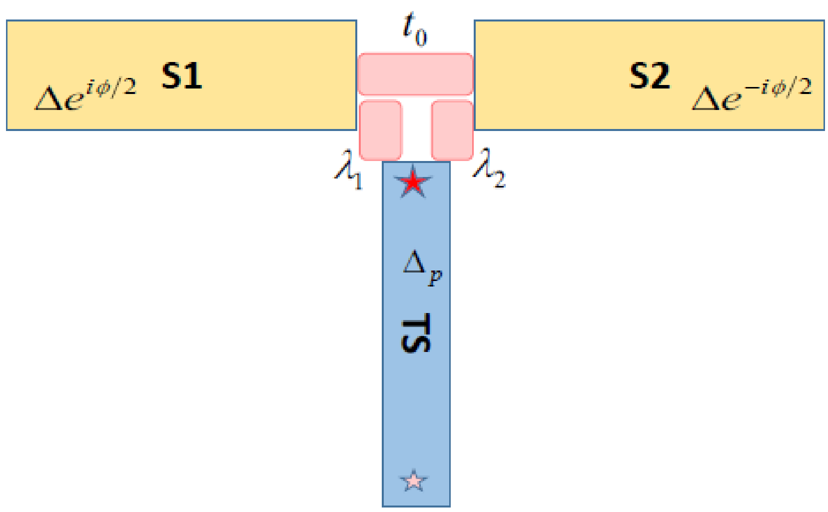

FIGURE 3.5: S-TS-S geometry: Two conventional superconductors (S1 and S2) with the same gap Δ and a TS wire with proximity gap Δ_p form a trijunction. The order parameter phase of S1 (S2), $\phi_1 = \phi/2$ ($\phi_2 = -\phi/2$), is taken relative to the phase of the TS wire, and tunnel couplings $\lambda_{1/2}$ connect S1/S2 to the TS wire. When the TS wire is decoupled ($\lambda_{1,2} = 0$), the S-S junction becomes a standard SAC with transparency $\mathcal{T}$ determined by the tunnel amplitude t_0, see Eq. (3.39).

3.3 S-TS-S junctions: Switching the parity of a superconducting atomic contact

The next junction we discuss is the three-terminal S-TS-S setup, where the TS wire is modeled after a Kitaev chain. A possible way to look at the junction is as a conventional superconducting atomic contact, the TS wire is tunnel-coupled to the S-S junction, see Fig. 3.5. As in the previous parts discussed, the current between a superconducting lead and a spinless topological superconducting lead is going to be suppressed, but because of the different parities of topological trivial and non trivial leads, interesting and useful things might be observed in this setup, specifically the reflections at the surfaces, which can resonate and form a standing wave, the so called Andreev bound states. As the Josephson current is not of much interest in this case, we take a look at different properties, for this purpose we calculate the Euclidean action, Euclidean denotes, that the path integral is done over the imaginary time instead of real time.

For the two S leads, boundary fermion fields are contained in Nambu spinors as in Eq. (3.6),

$$\Psi_{S,j=1,2} = \begin{pmatrix} \psi_{j,\uparrow} \\ \psi^\dagger_{j,\downarrow} \end{pmatrix}, \tag{3.34}$$

where their boundary Green's function follows with the Nambu matrix $g(\omega)$ in Eq. (3.6) as

$$g_j^{-1}(\omega) = g^{-1}(\omega) + b_j \tau_0. \tag{3.35}$$

We again use Pauli matrices $\tau_{x,y,z}$ and unity τ_0 in Nambu space. The dimensionless parameters $b_{1,2}$ describe the Zeeman field component along the Majorana bound state spin polarization axis. The TS wire is represented by the Majorana operator $\gamma = \gamma^\dagger$, with $\gamma^2 = 1/2$, which anticommutes with all other fermions. We represent

γ by an auxiliary fermion $f_\uparrow$, where the index reminds us that the Majorana bound state spin polarization points along $\hat{e}_z$,

$$\gamma = (f_\uparrow + f_\uparrow^\dagger)/\sqrt{2}. \tag{3.36}$$

The Majorana mode $\gamma' = -i(f_\uparrow - f_\uparrow^\dagger)/\sqrt{2}$ at the opposite end of the wire, is assumed to have negligible hybridization with the $\Psi_{S,j}$ spinors and with γ. We introduce the Euclidean action as $S = S_0 + S_{\text{tun}}$, the uncoupled action contribution is given by

$$\begin{aligned} S_0 &= \sum_{j=1,2} \int_0^\beta d\tau d\tau' \bar{\Psi}_{S,j}(\tau) g_j^{-1}(\tau-\tau') \Psi_{S,j}(\tau') + \\ &+ \frac{1}{2} \int_0^\beta d\tau \, \gamma(\tau) \partial_\tau \gamma(\tau). \end{aligned} \tag{3.37}$$

The leads are connected by a time-local tunnel action corresponding to the tunnel Hamiltonian

$$\begin{aligned} H_{\text{tun}} &= t_0 \left(\Psi_{S,1}^\dagger \tau_z e^{i\tau_z \phi/2} \Psi_{S,2} + \text{h.c.} \right) + \\ &+ \sum_{j=1,2} \frac{\lambda_j}{\sqrt{2}} \left(\psi_{j,\uparrow}^\dagger e^{i\phi_j/2} - \text{h.c.} \right) \gamma. \end{aligned} \tag{3.38}$$

We assume the tunnel amplitudes t_0 and $\lambda_{1,2}$ are real-valued without loss of generality and that they include density-of-state factors again. The transparency of the contact is determined by the parameter t_0 (with $0 \leq t_0 \leq 1$) and is given by [28]

$$\mathcal{T} = \frac{4t_0^2}{(1+t_0^2)^2}. \tag{3.39}$$

We trace out the $\Psi_{S,2}$ spinor field, so it is described in terms of one spinor field $\Psi \equiv \Psi_{S,1}$, which is coupled to the Majorana field γ. The effective action is then given by

$$\begin{aligned} S_{\text{eff}} &= \int_0^\beta d\tau d\tau' \Big\{ \bar{\Psi}(\tau) K^{-1}(\tau-\tau') \Psi(\tau') \\ &+ \Phi^T(\tau) \left[\frac{1}{2} \delta(\tau-\tau') \partial_{\tau'} - \lambda_2^2 P_\uparrow g_2(\tau-\tau') P_\uparrow \right] \Phi(\tau') \\ &+ \Big[\bar{\Psi}(\tau) \Big(\lambda_1 e^{i\phi_1/2} \delta(\tau-\tau') \\ &- \lambda_2 e^{i\phi_2/2} t_0 \tau_z e^{i\tau_z \phi/2} g_2(\tau-\tau') \Big) P_\uparrow \Phi(\tau') + \text{h.c.} \Big] \Big\}, \end{aligned} \tag{3.40}$$

where the operator $P_\uparrow = (\tau_0 + \tau_z)/2$ projects a Nambu spinor to its spin-$\uparrow$ component. The partition function follows with S_{eff} in Eq. (3.40) in the functional integral representation

$$Z = \int \mathcal{D}[\bar{\Psi}, \Psi, \gamma] e^{-S_{\text{eff}}} \equiv e^{-\beta F(\phi_1,\phi_2)}. \tag{3.41}$$

The Josephson current through S lead no. j then follows from the free energy via $I_j = (2e/\hbar)\partial_{\phi_j} F$. The supercurrent flowing through the TS wire is then given by

$$I_{\rm TS} = -(I_1 + I_2), \tag{3.42}$$

as dictated by current conservation.

We perform an atomic approximation to analyze the dynamics in the system. Δ represents the largest energy scale of interest and we can approximate $\sqrt{\Delta^2+\omega^2} \approx \Delta$. We rescale the equation with $\Psi \to \sqrt{\Delta/(1+t_0^2)}\Psi$ and get for the effective action in the atomic limit

$$\begin{aligned} S_{\rm at} &= \int_0^\beta d\tau \Big\{ \frac{1}{2}\gamma\partial_\tau\gamma + \bar{\Psi}\Big[\partial_\tau + \Delta\cos(\phi/2)\tau_x + \\ &\quad + r\Delta\sin(\phi/2)\tau_y + B_z\tau_0\Big]\Psi + \\ &\quad + \frac{1}{\sqrt{2}}\sum_{\sigma=\uparrow,\downarrow}\left(\lambda_\sigma\psi_\sigma^\dagger - \text{h.c.}\right)\gamma\Big\}, \end{aligned} \tag{3.43}$$

where $r = \sqrt{1-\mathcal{T}}$ is the reflection amplitude of the contact, see Eq. (3.39). We define additional parameters

$$\begin{aligned} \lambda_\uparrow &= \lambda_1\sqrt{(1+r)\Delta/2}\, e^{i\phi_1/2}, \\ \lambda_\downarrow &= -\lambda_2\sqrt{(1-r)\Delta/2}\, e^{-i\phi_2/2}, \\ B_z &= \left(\frac{1+r}{2}b_1 + \frac{1-r}{2}b_2\right)\Delta. \end{aligned} \tag{3.44}$$

Therefore the parameters $b_{1,2}$ in Eq. (3.35) effectively generate the Zeeman scale B_z in Eq. (3.44). The action can be written in terms of the effective Hamiltonian

$$\begin{aligned} H_{\rm at} &= \sum_{\sigma=\uparrow,\downarrow=\pm} \sigma B_z\psi_\sigma^\dagger\psi_\sigma + \left(\delta_A\psi_\uparrow^\dagger\psi_\downarrow^\dagger + \text{h.c.}\right) \\ &+ \frac{1}{\sqrt{2}}\sum_\sigma\left(\lambda_\sigma\psi_\sigma^\dagger - \text{h.c.}\right)\gamma, \end{aligned} \tag{3.45}$$

with

$$\delta_A(\phi) = \Delta\left[\cos(\phi/2) - ir\sin(\phi/2)\right]. \tag{3.46}$$

For a contact decoupled from the TS wire and taken at zero field ($B_z = 0$), the Andreev bound state energy follows from Eq. (3.45) in the standard form [43]

$$E_A(\phi) = |\delta_A| = \Delta\sqrt{1-\mathcal{T}\sin^2(\phi/2)}. \tag{3.47}$$

We can make a few observations at this point. The Majorana field $\gamma = (f_\uparrow + f_\uparrow^\dagger)/\sqrt{2}$, couples to both spin modes ψ_σ in Eq. (3.45). The coupling $\lambda_\downarrow$ between γ and the spin-$\downarrow$ field in the contact, $\psi_\downarrow$, is generated by crossed Andreev reflection processes, where a Cooper pair in lead S2 splits according to $\psi_{2,\uparrow}^\dagger\psi_{2,\downarrow}^\dagger \to f_\uparrow^\dagger\psi_{1,\downarrow}^\dagger$, plus the conjugate process. Next we observe that $H_{\rm at}$ is invariant under a particle-hole transformation, resulting in the replacements $\psi_\sigma \to \psi_\sigma^\dagger$ and $f_\uparrow \to f_\uparrow^\dagger$, along with $B_z \to -B_z$ and $\phi_j \to 2\pi - \phi_j$. Further $n_\sigma = \psi_\sigma^\dagger\psi_\sigma = 0,1$ and $n_f = f_\uparrow^\dagger f_\uparrow = 0,1$, the total fermion parity of the junction,

$$\mathcal{P}_{\text{tot}} = (-1)^{n_f+n_\uparrow+n_\downarrow} = \pm 1, \tag{3.48}$$

is a conserved quantity, $[\mathcal{P}_{\text{tot}}, H_{\text{at}}]_- = 0$. For the analysis we restrict our observations to the even-parity sector $\mathcal{P}_{\text{tot}} = +1$, the results for the odd-parity case are analogous. The Hilbert subspace is spanned by the following four states

$$|n_\uparrow, n_\downarrow, n_f\rangle = \left(\psi_\uparrow^\dagger\right)^{n_\uparrow} \left(\psi_\downarrow^\dagger\right)^{n_\downarrow} \left(f_\uparrow^\dagger\right)^{n_f} |0\rangle, \tag{3.49}$$

where $(n_\uparrow, n_\downarrow, n_f) \in \{(0,0,0),(1,1,0),(1,0,1),(0,1,1)\}$ and $|0\rangle$ is the vacuum state. In this basis, the Hamiltonian (3.45) has the matrix representation

$$\mathcal{H}_{\text{at}}(\phi_1,\phi_2) = \begin{pmatrix} 0 & \delta_A^* & \lambda_\uparrow^*/2 & \lambda_\downarrow^*/2 \\ \delta_A & 0 & \lambda_\downarrow/2 & -\lambda_\uparrow/2 \\ \lambda_\uparrow/2 & \lambda_\downarrow^*/2 & B_z & 0 \\ \lambda_\downarrow/2 & -\lambda_\uparrow^*/2 & 0 & -B_z \end{pmatrix}. \tag{3.50}$$

The ground state energy $E_G^{(\text{e})} = \min(\varepsilon)$ follows from

$$\det\left(\mathcal{H}_{\text{at}} - \varepsilon\right) = 0. \tag{3.51}$$

We now consider some different cases for our analysis. The first case we consider is that the TS wire is only coupled to the first S wire, $\lambda_2 = 0$ and therefore $\lambda_\downarrow = 0$, as a result we get the four eigenenergies

$$\begin{aligned} \varepsilon_\pm \;&=\; \frac{1}{\sqrt{2}}\Bigg(E_A^2 + B_z^2 + \frac{1}{2}|\lambda_\uparrow|^2 \\ &\pm\; \sqrt{\left(E_A^2 - B_z^2\right)^2 + |\lambda_\uparrow|^2\left(E_A^2 + B_z^2\right)}\Bigg)^{1/2}. \end{aligned} \tag{3.52}$$

The groundstate energy is therefore given by $E_G^{(\text{e})} = -\varepsilon_+$ and the only terms depending on the phases $\phi_{1,2}$ are given by the Andreev level energy $E_A(\phi)$. The Josephson current is given by

$$I_1 = -I_2 = \frac{2e}{\hbar}\partial_\phi E_G^{(\text{e})} = -\frac{2e}{\hbar}\partial_\phi \varepsilon_+. \tag{3.53}$$

Therefore no supercurrent flows through the TS wire.

Next we consider the case, when the TS wire is absent, ($\lambda_1 = 0$). As a result the even and odd parity sectors are decoupled, $\mathcal{P}_{\text{SAC}} = (-1)^{n_\uparrow+n_\downarrow} = \pm 1$. If the ground state is in the odd parity sector for $|B_z| > E_A(\phi)$, the Josephson current is fully blocked, but if the TS wire is no longer decoupled ($\lambda_1 \neq 0$), the parity of the contact is no longer conserved. Meaning the Majorana bound state acts as a parity switch between the two sectors and lifts the supercurrent blockade. For more details see A.1.

Chapter 4

Boundary Green's function approach for spinful single-channel and multichannel Majorana nanowires

The second publication A.2, focuses on spinful nanowire models and their application. As in the previously mentioned, the calculations for the spinful model are done numerically, we will try to get an analytical understanding of the model. For this purpose we are going to summarize interesting and useful properties from the boundary Green's function method. Afterwards we are going to expand the model from a single channel to a multi channel model and introduce a model for different topological superconductors than the proximity induced ones. Finally we examine junctions including these models.

4.1 Boundary Green's function

Starting with the boundary Green's function method, the infinitely long nanowire is described by following Hamiltonian

$$H_{\text{bulk}} = \frac{1}{2}\sum_k \hat{\Psi}_k^\dagger \hat{\mathcal{H}}(k)\hat{\Psi}_k, \tag{4.1}$$

which is an infinitely long chain with lattice spacing a, $\hat{\mathcal{H}}(k)$ is a $N \times N$ Bogoliubov-de Gennes Hamiltonian and $\hat{\Psi}_k$ are fermionic Nambu spinor fields. The retarded Green's function of the infinite chain is defined as

$$\hat{G}^R(k,\omega) = \left[\omega + i0^+ - \hat{\mathcal{H}}(k)\right]^{-1}. \tag{4.2}$$

Switching to real space, we get

$$\hat{G}^R_{jj'}(\omega) = \frac{a}{2\pi}\int_{-\pi/a}^{\pi/a} dk\, e^{i(j-j')ka}\,\hat{G}^R(k,\omega) \tag{4.3}$$

with lattice site indices j, j' and we substitute $z = e^{ika}$ to turn it into a complex contour integral

$$\hat{G}^R_{jj'}(\omega) = \frac{1}{2\pi i}\oint_{|z|=1} \frac{dz}{z} z^{j-j'}\hat{G}^R(z,\omega). \tag{4.4}$$

For the calculation we need to determine the roots $z_n(\omega)$ of the characteristic polynomial in the complex-z plane

$$P(z,\omega) = \det\left[\omega - \hat{\mathcal{H}}(z)\right] = \frac{1}{z^N}\prod_{n=1}^{2N}\left[z - z_n(\omega)\right]. \tag{4.5}$$

We rewrite the integral as a sum over the residues of all roots inside the unit circle

$$\hat{G}^R_{jj'}(\omega) = \sum_{|z_n|<1} \frac{z_n^{j-j'}\hat{A}(z_n,\omega)}{\prod_{m\neq n}(z_n - z_m)}, \tag{4.6}$$

where $\hat{A}(z,\omega)$ is the cofactor matrix of $[\omega - \mathcal{H}(z)]\,z$. For notational simplicity, we omit the superscript 'R' in retarded GFs from now on. As we analyze junctions, we need to derive the boundary Green's function of a semi-infinite nanowire from the infinite wire [9], [45]. Therefore an impurity with potential ϵ is placed in the middle of the wire at lattice site $j = 0$ and take the limit $\epsilon \to \infty$, effectively cutting the chain in half. With the Dyson equation we get for the local Green's function components of the cut nanowire

$$\hat{\mathcal{G}}_{jj}(\omega) = \hat{G}_{jj}(\omega) - \hat{G}_{j0}(\omega)\left[\hat{G}_{00}(\omega)\right]^{-1}\hat{G}_{0j}(\omega). \tag{4.7}$$

The left and right parts are given by

$$\hat{\mathcal{G}}_L(\omega) = \hat{\mathcal{G}}_{-1,-1}(\omega), \quad \hat{\mathcal{G}}_R(\omega) = \hat{\mathcal{G}}_{11}(\omega). \tag{4.8}$$

We seen from the calculation of the boundary Green's function, that the roots $z_n(\omega)$ play an important role in the calculation and we can derive information about the physics in the system from them and are going to use them to analyze different models for nanowires. At this point we can summarize some general properties of the roots:

(i) Hermiticity of the BdG Hamiltonian implies that every root $z_n(\omega)$ is accompanied by a root $1/z_n^*(\omega)$, where '$*$' denotes complex conjugation.

(ii) Electron-hole symmetry of the BdG Hamiltonian implies that $z_n(\omega) = z_n^*(-\omega)$. In the presence of an additional symmetry $\hat{\mathcal{H}}(k) = \hat{U}\hat{\mathcal{H}}(-k)\hat{U}^\dagger$ with a unitary matrix $\hat{U}$, for every root $z_n(\omega)$, also $z_n^*(\omega)$ must be a root.

(iii) As a consequence of (i) and (ii), $\prod_{n=1}^{2N} z_n(\omega) = 1$.

(iv) Topological phase transitions can occur once a pair of zero-energy roots hits the unit circle, $|z_n(0)| = 1$, which corresponds to the closing and reopening of a gap in the bulk spectrum.

(v) Equations (4.6) and (4.7) imply that subgap bound states (with energy E) localized near the boundary of a semi-infinite wire decay into the bulk in a manner controlled by $\max(|z_n(E)| < 1)$.

4.2 Spinful single-channel hybrid nanowires

Defining the roots for the calculation of the boundary Green's function, has given us an analytical approach to analyze the spinful nanowire model from Sec. 2.3.3. The first model we analyze is the spinful single-channel model we used in the previous chapter for spinful topological junctions. Using the Nambu bispinor $\hat{\Psi}_k^T = \left(c_{k\uparrow}, c_{k\downarrow}, c^\dagger_{-k\downarrow}, -c^\dagger_{-k\uparrow}\right)$ with fermionic annihilation operator $c_{k\sigma}$ for momentum k and spin $\sigma = \uparrow, \downarrow$, we get for the Hamiltonian in Eq. (4.1)

$$\mathcal{H}(k) = \epsilon_k \sigma_0 \tau_z + V_x \sigma_x \tau_0 + \alpha_k \sigma_z \tau_z + \Delta \sigma_0 \tau_x, \tag{4.9}$$

where $\tau_{x,y,z}$, τ_0 are Pauli matrices in spin and Nambu space and $\sigma_{x,y,z}$, σ_0 are usual Pauli matrices. The kinetic energy is given by $\epsilon_k = 2t[1 - \cos(ka)] - \mu$ with lattice spacing a, chemical potential μ and the nearest-neighbor hopping amplitude t. V_x is the magnetic Zeeman field along the wire axis, $\alpha_k = \alpha \sin(ka)$ describes the spin-orbit interaction and Δ is the proximity-induced on-site pairing amplitude. The bulk dispersion relation, $E = E_{k,\pm} \geq 0$, is given by [13], [14]

$$E^2_{k,\pm} = \Delta^2 + \alpha_k^2 + V_x^2 + \epsilon_k^2 \pm 2\sqrt{\Delta^2 V_x^2 + (\alpha_k^2 + V_x^2)\epsilon_k^2}. \tag{4.10}$$

The model enters the topological phase for $V_x > V_c = \sqrt{\Delta^2 + \mu^2}$ and we use values for the parameters appropriate for InAs wires as in Sec. 3.2.

To gain further insight into the model, we look at the roots $z_n(\omega)$. The roots need to satisfy Eq. (4.5) and using $z = e^{ika}$ we get following condition for the model

$$\begin{aligned} &2\Delta^2 \left[\tilde{\alpha}^2(z) + \epsilon^2(z) - V_x^2 - \omega^2\right] + \\ &+2\tilde{\alpha}^2(z)\left[V_x^2 - \omega^2 - \epsilon^2(z)\right] + \tilde{\alpha}^4(z) + V_x^4 + \Delta^4 + \\ &+\left[\omega^2 - \epsilon^2(z)\right]^2 - 2V_x^2\left[\omega^2 + \epsilon^2(z)\right] = 0, \end{aligned} \tag{4.11}$$

with the functions

$$\tilde{\alpha}(z) = -i\alpha(z - z^{-1})/2, \quad \epsilon(z) = -t(z + z^{-1} - 2) - \mu. \tag{4.12}$$

This condition can be expressed as an eighth-order polynomial equation

$$\sum_{m=0}^{8} a_m(\omega) z^m = 0, \tag{4.13}$$

with the normalization conditions $a_0 = a_8 = 1$. These roots can be grouped up into two different classes related to the pairing gaps Δ_1 and Δ_2, which vanish for $\Delta \to 0$ and the points at which the dispersion relation becomes gapless for $\Delta = 0$ are given by

$$\begin{aligned} k_{1,2} \simeq \cos^{-1}\Bigg(&\frac{2t(2t-\mu)}{\alpha^2 + 4t^2} \\ &\pm \frac{\sqrt{V_x^2(\alpha^2 + 4t^2) + \alpha^4 + 4t\mu\alpha^2 - \alpha^2\mu^2}}{\alpha^2 + 4t^2}\Bigg). \end{aligned} \tag{4.14}$$

We first take a look at the topological trivial regime $V_x < V_c$. We can see in Fig. 4.1, that the low-energy physics will be dominated by the regions $|k| \approx k_1$ and

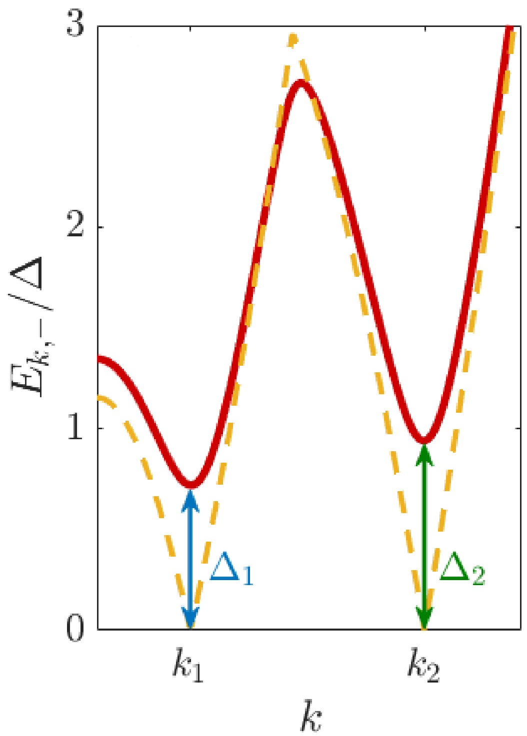

FIGURE 4.1: Bulk dispersion relation of the spinful single-channel Majorana wire model [13,14] . $E_{k,-}$ vs k, see Eq. (4.10), for the topologically trivial regime $V_x < V_c$ (solid red curve), indicating the two pairing gaps Δ_1 and Δ_2 at $k = k_1$ and $k = k_2$, respectively, cf. Eq. (4.14). We use $\mu = 5$ meV, $\Delta = 2$ meV, and $V_x = 0.5V_c$. All other parameters are specified in the main text. The dashed yellow curve is for $\Delta = 0$.

$|k| \approx k_2$ and we get the corresponding pairing gaps $\Delta_{1,2} = |E_{k_{1,2},-}|$ by substituting $k_{1,2}$ into the bulk dispersion relation (4.10). The pairing gap Δ_1 closes and reopens during the topological transition of V_x. Seeing the dispersion relation in Fig. 4.1, the dispersion relation becomes gapless for $\Delta = 0$ and we can linearize and approximate Eq. (4.10) for electrons and holes near $k = k_1$ and $k = k_2$. We define the velocities $v_{\nu=1,2} = |\partial_k E_{k=k_\nu,-}|_{\Delta=0}$ and the effective Hamiltonian near k_1, k_2 is given by

$$\mathcal{H}_{\text{eff},\nu=1,2}(k) \simeq \begin{pmatrix} v_\nu(k-k_\nu) & \Delta_\nu \\ \Delta_\nu & -v_\nu(k-k_\nu) \end{pmatrix}, \tag{4.15}$$

The condition $\det[\omega - \mathcal{H}_{\text{eff},\nu}(z)] = 0$ can be solved with $ika = \ln z$ and the effective roots are given by

$$z_\nu(\omega) \simeq \left(1 \pm \frac{a}{v_\nu}\sqrt{\Delta_\nu^2 - \omega^2}\right) e^{ik_\nu a}, \tag{4.16}$$

plus the complex conjugate values. Seeing this result, we propose an ansatz for the roots inside the unit circle for the topological trivial regime

$$z_\nu(\omega) = \left(1 - \tau_\nu\sqrt{\Delta_\nu^2 - \omega^2}\right) e^{i\delta_\nu}, \tag{4.17}$$

where $\tau_{1,2}$ and $\delta_{1,2}$ are phenomenological coefficients and the complex conjugate roots is also a solution. Because we assumed Δ and $|\omega|$ are small, the parameters are limited $\tau_\nu = a/v_\nu$ and $\delta_\nu = k_\nu a$. In addition, we also impose the condition

$$\tau_1\Delta_1 = \tau_2\Delta_2 = \eta \ll 1, \tag{4.18}$$

where η is a small parameter.

Next we take a look at the topologically nontrivial regime $V_x > V_c$. In the topological phase the momentum k_1 in Eq. (4.14) becomes purely imaginary and the previous ansatz needs to be adjusted with $\delta_1 \to i\delta_1$. The resulting roots are then real valued and given by

$$\begin{aligned} z_{1,\pm}(\omega) &= \left(1 \pm \tau_1\sqrt{\Delta_1^2 - \omega^2}\right) e^{-\delta_1}, \\ z_{2,\pm}(\omega) &= \left(1 - \tau_2\sqrt{\Delta_2^2 - \omega^2}\right) e^{\pm i\delta_2}, \end{aligned} \tag{4.19}$$

where both δ_1 and δ_2 are real positive.

The topological invariant is given by [44]

$$Q = \frac{\operatorname{sgn} \operatorname{Pf} \hat{\mathcal{H}}(k=0)}{\operatorname{sgn} \operatorname{Pf} \hat{\mathcal{H}}(k=\pi/a)} = \pm 1 \tag{4.20}$$

and the amount of complex conjugate root pairs N_p near, but inside, the unit circle corresponds to the topological invariant $Q = (-1)^{N_p}$. For an odd number of pairs the phase is topologically nontrivial and for an even number it is trivial. Transitioning from the topological trivial to nontrivial phase, the complex conjugate z_1 roots gather to form an almost degenerate root pair located on the real axis inside the unit circle. This switch between the topological invariants happens, when the determinant of the Hamiltonian at $k = 0$ vanishes. For a more detailed analysis see A.2.

4.3 Two-channel class-D nanowire

Now we want to expand the model for the spinful nanowire model to the multichannel case. Specifying that we are discussing a class-D nanowire, is because of the model introduced in the next part. The model is for spinful topological superconductors for nanowires created through the proximity effect as described in Sec. 2.3.3, during their creation time symmetry is broken, which class-D denotes. The boundary Green's function method could be applied for an arbitrary number of channels, but the polynomials would become rather large, therefore we restrict it to the dual channel case, which still shows features of multichannel nanowires [46], [47]. The two-channel wire is described by two single-channel wires coupled to each other, the Hamiltonian for the two-channel case is given by

$$\hat{\mathcal{H}}_{\text{2ch}}(k) = \begin{pmatrix} \hat{\mathcal{H}}(k) & \hat{T} \\ \hat{T}^{\dagger} & \hat{\mathcal{H}}(k) \end{pmatrix} \tag{4.21}$$

and the tunnel couplings are given by

$$\hat{T} = -t_y\sigma_0\tau_z + i\alpha_y\sigma_x\tau_z + \Delta_y\sigma_0\tau_x, \tag{4.22}$$

where t_y and α_y are spin-conserving and spin-flipping hopping amplitudes. For our current class D model, we find that allowing for a small $\Delta_y \neq 0$ does not lead to significant changes in the phase diagram, therefore we set $\Delta_y = 0$ for this part. The topological invariant can be calculated the same way as for the single channel model, we just have to replace the Hamiltonian and the Pfaffian at $k = 0$ is given by

$$\begin{aligned} \operatorname{Pf}\hat{\mathcal{H}}_{\text{2ch}}(0) &= \alpha_y^4 + \left[(\mu - 3t_y)^2 - V_x^2 + \Delta^2\right] \times \\ &\times \left[(\mu - t_y)^2 - V_x^2 + \Delta^2\right] + \\ &+ 2\alpha_y^2\left[-(\mu - 3t_y)(\mu - t_y) - V_x^2 + \Delta^2\right]. \end{aligned} \tag{4.23}$$

The boundaries of the topological phases are given by the two critical Zeeman fields

$$\begin{aligned} V_{c,\pm} &= \Big(\alpha_y^2 + \mu^2 - 4\mu t_y + 5t_y^2 + \Delta^2 + \\ &\qquad \pm 2|\mu - 2t_y|\sqrt{t_y^2 + \alpha_y^2}\Big)^{1/2} \end{aligned} \tag{4.24}$$

and the resulting phase diagram is depicted in Fig. **??**.

We can analyze the behavior of the roots, the same way as for the single-channel model. The result is similar to the single-channel model, when an odd number of root pairs is on the unit circle, the system is in the topological phase. Also for increasing V_x a root pair gathers on the real axis again and forms an almost degenerate root pair. The similarities in behavior are easy to explain, as the model for the two-channel nanowire is effectively a pair of single-channel wires. For more details regarding the model see A.2.

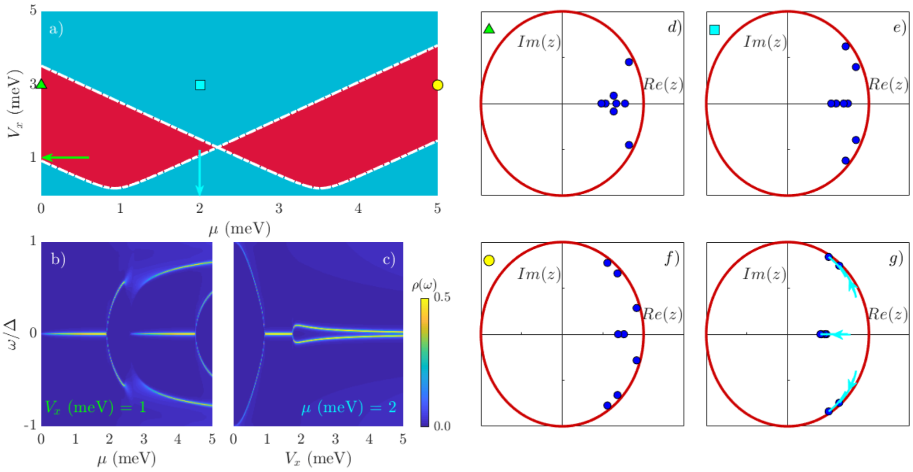

FIGURE 4.2: Two-channel spinful Majorana wire model of class D, see Eq. (4.21), with parameters as explained in the main text. Panel a) shows the bulk phase diagram in the μ-V_x plane. Topological non-trivial (trivial) phases are shown in red (blue). Panels b) and c) show the energy dependence of the local DoS, $\rho_{j=1}(\omega)$ [in meV^{-1}], at the boundary of a semi-infinite two-channel wire along the trajectories marked by arrows in panel a). Panels d)–f) illustrate the roots $z_n(0)$ inside the unit circle at the three points indicated in panel a) by a triangle [d)], a square [e)], and a circle [f)], respectively. Panel g) shows the evolution of the roots within the topologically trivial regime as V_x increases from 3 to 8 meV at constant chemical potential $\mu = 2$ meV. In panels d)–g), we use $\Delta = 1$ meV.

4.4 TRITOPS nanowires

Previously we were looking at models for proximity induced nanowires, where time reversal symmetry was broken in their creation, now we are going to look at TRITOPS wires, meaning time reversal symmetry is not broken in their creation. Different proposals for their physical realization have been put forward in recent years [53–70]. We are going to look at both the single-channel case and the two-channel case.

The Hamiltonian for the single-channel case is given by [56]

$$\hat{\mathcal{H}}_{\mathrm{DIII}}(k) = \epsilon_k \sigma_0 \tau_z + \alpha_k \sigma_z \tau_z + \Delta_k \sigma_0 \tau_x, \tag{4.25}$$

where DIII is the symmetry class, the Nambu spinors are the same as before and

$$\begin{aligned} \epsilon_k &= -2t\cos(ka) - \mu, \quad \alpha_k = 2\alpha\sin(ka), \\ &\Delta_k = 2\Delta\cos(ka). \end{aligned} \tag{4.26}$$

In this model t still corresponds to a nearest-neighbor hopping amplitude, μ is the chemical potential, a the lattice spacing and α the spin-orbit coupling strength. The parameter Δ corresponds to a nearest-neighbor pairing interaction. It is possible to block-diagonalize the Hamiltonian, $\hat{\mathcal{H}}_{\mathrm{DIII}} = \mathrm{diag}(\hat{\mathcal{H}}_-, \hat{\mathcal{H}}_+)$, by replacing $\hat{\Psi}_k^T \to \left(c_{k\uparrow}, c^\dagger_{-k\downarrow}, c_{k\downarrow}, -c^\dagger_{-k\uparrow}\right)$ and we get

$$\hat{\mathcal{H}}_\pm(k) = (\epsilon_k \mp \alpha_k)\tilde{\sigma}_z + \Delta_k \tilde{\sigma}_x = \boldsymbol{\beta}_\pm(k) \cdot \tilde{\boldsymbol{\sigma}}, \tag{4.27}$$

where $\tilde{\boldsymbol{\sigma}}$ is the vector of $\tilde{\sigma}_{x,y,z}$ Pauli matrices in the respective 2×2 space obtained after block diagonalization. Each Hamiltonian $\hat{\mathcal{H}}_{\pm}(k)$ corresponds to a Dirac-type model where

$$\boldsymbol{\beta}_{\pm}(k) = \begin{pmatrix} 2\Delta\cos(ka) \\ 0 \\ -\mu - 2t\cos(ka) \pm 2\alpha\sin(ka) \end{pmatrix} \tag{4.28}$$

is a vector field mapping the first Brillouin zone onto a closed curve.

Projecting $\hat{\mathcal{H}}_{\pm}$ to the $\tilde{\sigma}_x$-$\tilde{\sigma}_z$ plane, we obtain an elliptic curve. If the ellipse encloses the origin of the $\tilde{\sigma}_x$-$\tilde{\sigma}_z$ plane, we know that for a semi-infinite wire, $\hat{\mathcal{H}}_{\pm}(k)$ will generate an edge state with energy equal to the modulus of the component of $\boldsymbol{\beta}_{\pm}(k)$ perpendicular to this plane [48]. This means for us $[\boldsymbol{\beta}_{\pm}(k)]_y = 0$, that we have a pair of zero-energy boundary states in the topological phase. We get from Eq. (4.28), that the topological transition occurs at $ka = \pm\pi/2$ and $|\mu| = 2\alpha$. This conclusion is consistent with the fact that at the topological transition, one finds roots at $z = e^{ika} = \pm i$, see also Ref. [45], in agreement with property (v) in Sec. 4.1. Using the boundary Green's function method we can determine the roots $z_n(\omega)$ of a semi-infinite wire again. An analytical expression for the largest-modulus zero-frequency root, z_{max}, inside the unit circle can be computed from purely geometrical considerations for the ellipse using the results from [48], [49]. The calculation can be seen in the appendix of A.2. The length scale governing the spatial decay profile of the pair of Majorana states localized near the boundary of a semi-infinite TRITOPS wire then follows as $\lambda_e = -\frac{a}{2}\ln|z_{\text{max}}|$.

For the two-channel case we proceed as before, it is constructed by coupling two single-channel wires together and the Hamiltonian is given by

$$\hat{\mathcal{H}}_{\text{DIII,2ch}}(k) = \begin{pmatrix} \hat{\mathcal{H}}_{\text{DIII}}(k) & \hat{T}_{\text{DIII}} \\ \hat{T}^{\dagger}_{\text{DIII}} & \hat{\mathcal{H}}_{\text{DIII}}(k) \end{pmatrix} \tag{4.29}$$

with the interwire tunneling coupling

$$\hat{T}_{\text{DIII}} = -t_y\sigma_0\tau_z + i\alpha_y\sigma_y\tau_z + \Delta_y\sigma_0\tau_z. \tag{4.30}$$

Spin-conserving (t_y) and spin-flipping (α_y) hopping processes are allowed, as well as for non-local pairing terms (Δ_y). t_y and α_y are parametrized as specified in Sec. 4.3. The phase diagram of the model is displayed in Fig. 4.3. To make some analytical progress, we consider the case $\Delta_y = 0$ and determine the conditions for gap closings. The gap closes again for $ka = \pm\pi/2$ as for the single-channel TRITOPS wire, but now for the chemical potential set to one of the critical values

$$|\mu_{\pm}| = \sqrt{\alpha_y^2 + (t_y \pm 2\alpha)^2}. \tag{4.31}$$

where the topological invariant is related to the product of the signs of the effective pairing amplitude at different Fermi points [50]. For further explanations see A.2.

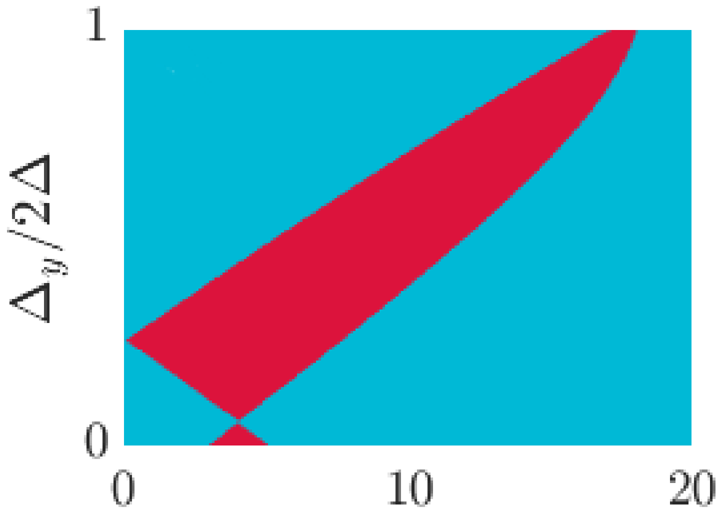

FIGURE 4.3: Two-channel TRITOPS nanowire, see Eq. (4.29), with parameters as explained in the main text. Shows the phase diagram in the μ-Δ_y plane, with the topologically nontrivial (trivial) phase in red (blue).

4.5 Phase-biased topological Josephson junctions

After introducing different models for spinful topological nanowires, we want to take a look at different Josephson junctions. The first junction we consider is a three-terminal junction made out of three spinful single-channel nanowires in the topological phase. All three of them are in plane with two of them aligned and the third at an arbitrary angle θ to the other two. We assume no direct tunneling between the two aligned wires, left and right, exists and a Zeeman field V_z perpendicular to the junction is applied. As the angle between the wires is important, we need to introduce a reference frame for the system and define rotations to achieve our setup.

The boundary Green's functions for the left and right wires are given by

$$\hat{\mathcal{G}}'_{L/R} = R_y \hat{\mathcal{G}}_{L,R} R_y^{-1} \tag{4.32}$$

with $\hat{\mathcal{G}}_{L,R}$ as described in Sec. 4.2 and the rotation matrix $R_y = R(\vartheta = \pi/2)$, which transforms a Zeeman field along the x-direction into a Zeeman field along the negative z-direction, with

$$R(\vartheta) = \left[\sigma_0 \cos(\vartheta/2) - i\sigma_y \sin(\vartheta/2)\right] \tau_0. \tag{4.33}$$

The position of the third wire is given by

$$\hat{\mathcal{G}}_C = R_z(\theta) R_y \hat{\mathcal{G}}_L R_y^{-1} R_z^{-1}(\theta), \tag{4.34}$$

where we get the rotation matrix $R_z(\theta)$ by replacing $\sigma_y \to \sigma_z$ and $\vartheta \to \theta$. The tunnel Hamiltonian for the coupling between the three wires, which conserves spin, is given by

$$H_T = \frac{1}{2} \sum_{\nu=L,R} \hat{\Psi}_\nu^\dagger \hat{\lambda}_\nu \hat{\Psi}_C + \text{h.c.}, \quad \hat{\lambda}_\nu = \lambda_\nu \sigma_0 \tau_z e^{i\tau_z \phi_\nu/2} \tag{4.35}$$

with the boundary spinor fields $\hat{\Psi}_{L,R,C}$, the superconducting phase ϕ_ν of the corresponding wire and real valued tunnel couplings $\lambda_n u$. We set the gauge with $\phi_C = 0$ and the full boundary Green's function is

$$\hat{G}_{3\text{TS}} = \begin{pmatrix} \hat{\mathcal{G}}_L^{-1} & \hat{\lambda}_L & 0 \\ \hat{\lambda}_L^\dagger & \hat{\mathcal{G}}_C^{-1} & \hat{\lambda}_R \\ 0 & \hat{\lambda}_R^\dagger & \hat{\mathcal{G}}_R^{-1} \end{pmatrix}^{-1} \tag{4.36}$$

and the local density of states at the junction follows as

$$\rho_{3\text{TS}}(\omega) = -\frac{1}{\pi}\text{Im}\,\text{Tr}\left[\hat{G}_{3\text{TS}}(\omega)\right]. \tag{4.37}$$

As the wires are in the topological phase, the low-energy properties of the trijunction are going to be dominated by the Majorana bound states. Therefore we derive a minimal model, keeping only Majorana bound states at the junction. The effective Hamiltonian for each wire is then given by

$$H_{\text{eff},\nu} = \lim_{\omega\to 0} \hat{\mathcal{G}}_\nu^{-1}(\omega). \tag{4.38}$$

From our analysis of the model for the spinful single-channel nanowire we know, that the z_2 roots dominate in the topological phase and the spinors are therefore given by [30]

$$\begin{aligned} \hat{\Psi}_L &\simeq \sqrt{\frac{\Delta_2}{t}}\begin{pmatrix} 0 \\ 1 \\ -i \\ 0 \end{pmatrix}\gamma_L, \quad \hat{\Psi}_R \simeq \sqrt{\frac{\Delta_2}{t}}\begin{pmatrix} 0 \\ -i \\ 1 \\ 0 \end{pmatrix}\gamma_R, \\ \hat{\Psi}_C &\simeq \sqrt{\frac{\Delta_2}{t}}R_z(\theta)\begin{pmatrix} 0 \\ 1 \\ -i \\ 0 \end{pmatrix}\gamma_C, \end{aligned} \tag{4.39}$$

where the Majorana operators γ_ν satisfy the anticommutation relations $\{\gamma_\nu, \gamma_{\nu'}\} = \delta_{\nu\nu'}$ and the pairing gap is as defined in section 4.2. With the boundary spinors we can project the tunneling Hamiltonian to the minimal model and get

$$H_{\text{mm}} = -i\Omega_L(\phi)\gamma_L\gamma_C - i\Omega_R(\phi)\gamma_R\gamma_C, \tag{4.40}$$

with the energies

$$\begin{aligned} \Omega_L(\phi) &= \frac{2\Delta_2\lambda_L}{t}\sin\left(\frac{\phi+\theta}{2}\right), \\ \Omega_R(\phi) &= -\frac{2\Delta_2\lambda_R}{t}\cos\left(\frac{\phi-\theta}{2}\right). \end{aligned} \tag{4.41}$$

We can diagonalize the Hamiltonian for the minimal model by rotating the $\gamma_{L,R}$ operators to new Majorana operators $\tilde{\gamma}_{L,R}$,

$$\begin{pmatrix} \gamma_L \\ \gamma_R \end{pmatrix} = \begin{pmatrix} \sin\kappa & -\cos\kappa \\ \cos\kappa & \sin\kappa \end{pmatrix}\begin{pmatrix} \tilde{\gamma}_L \\ \tilde{\gamma}_R \end{pmatrix}, \tag{4.42}$$

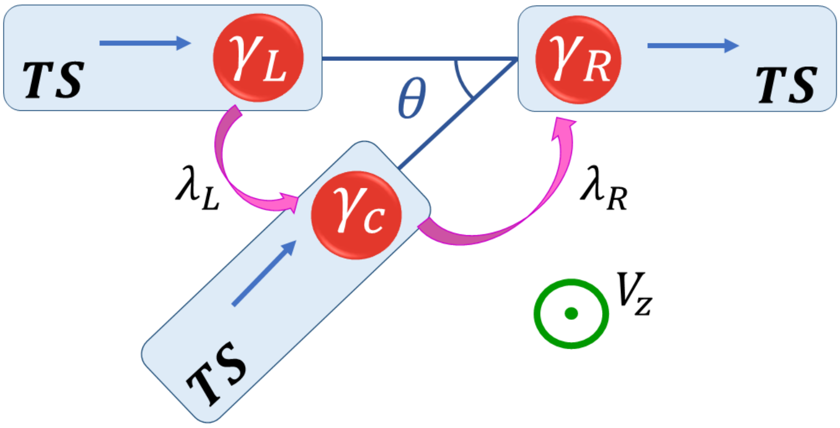

FIGURE 4.4: Three-terminal junction of spinful TS nanowires (cf. Sec. 4.2), with two parallel wires (L, R) and a central (C) wire at angle θ. The red dots indicate Majorana bound states with Majorana operators $\gamma_{L,R,C}$ near the junction, with tunnel couplings $\lambda_{L,R}$ connecting the L, R wires to the C wire. We assume that no direct tunnel coupling between the L and R wires is present. A Zeeman field V_z is applied perpendicular to the plane containing the three wires. Blue arrows show the positive momentum direction in each wire.

with $\sin\kappa = \Omega_L/\Omega$ and

$$\Omega(\phi) = \sqrt{\Omega_L^2(\phi) + \Omega_R^2(\phi)}. \tag{4.43}$$

We get for the diagonalized Hamiltonian

$$H_{\text{mm}} = -i\Omega(\phi)\tilde{\gamma}_L\gamma_C, \tag{4.44}$$

where the decoupled Majorana operator $\tilde{\gamma}_R$ describes the remaining zero-energy state [51]. The eigenstates of the minimal model are

$$E_\pm(\phi) = \pm\frac{1}{2}\sqrt{\Omega_L^2(\phi) + \Omega_R^2(\phi)} \tag{4.45}$$

and correspond to Andreev bound states with phase dependent subgap energy. We get the Josephson current-phase relation from $\partial_\phi E_-(\phi)$.

The next junction we observe is a two-terminal Josephson junction between a TRITOPS and a TS spinful nanowire. Both wires are coupled to each other with the tunneling Hamiltonian

$$H_T = \frac{1}{2}\lambda_L\hat{\Psi}_L^\dagger\,\sigma_0 e^{i\tau_z\phi/2}\tau_z\hat{\Psi}_R + \text{h.c.}, \tag{4.46}$$

where ϕ is the superconducting phase difference across the junction and real-valued tunnel coupling λ_L. As previously done, we assume the pairing gap Δ is identical for both wires. The relative angle θ between the directions of the spin-orbit fields is variable. The TS wire needs a Zeeman field to induce the topological phase, while in the TRITOPS wire no Zeeman field should be present. To achieve this mesoscopic ferromagnets can be used to induce a Zeeman field locally [52]. As we are going to observe the system relative to an angle again, we proceed similar to the previous junction and rotate the boundary Green's function for the TS wire with $R_y(\theta)$. As we assume that both wires are in the topological phase, we again derive a minimal model for the Majorana bound states and the spinors with Majorana operators $\gamma_{L1,L2,R}$ are

$$\begin{aligned} \hat{\Psi}_L &\simeq \sqrt{\frac{\Delta}{t}} \begin{pmatrix} 1 \\ 0 \\ i \\ 0 \end{pmatrix} \gamma_{L1} + \sqrt{\frac{\Delta}{t}} \begin{pmatrix} 0 \\ i \\ 0 \\ 1 \end{pmatrix} \gamma_{L2}, \\ \hat{\Psi}_R &\simeq \sqrt{\frac{\Delta_2}{t}} R_y(\theta) \begin{pmatrix} i \\ -i \\ 1 \\ 1 \end{pmatrix} \gamma_R. \end{aligned} \tag{4.47}$$

The resulting minimal model Hamiltonian is

$$H_{\min} = -i \left[w_1(\phi)\gamma_{L1} + w_2(\phi)\gamma_{L2} \right] \gamma_R \tag{4.48}$$

with the energies

$$\begin{aligned} w_1(\phi) &= \frac{2\lambda_L \sqrt{\Delta\Delta_2}}{t} \cos\frac{\phi}{2} \cos\frac{\theta}{2}, \\ w_2(\phi) &= -\frac{2\lambda_L \sqrt{\Delta\Delta_2}}{t} \sin\frac{\phi}{2} \sin\frac{\theta}{2}. \end{aligned} \tag{4.49}$$

The structure of this minimal model is similar to the minimal model of the previous junction and we get for the eigenstates

$$E_\pm(\phi) = \pm\frac{1}{2}\sqrt{w_1^2(\phi) + w_2^2(\phi)}. \tag{4.50}$$

The subgap spectrum is characterized by a decoupled zero-energy Majorana state and the hybridization of the two other Majorana operators yields the Andreev bound state dispersion. For more details see A.2.

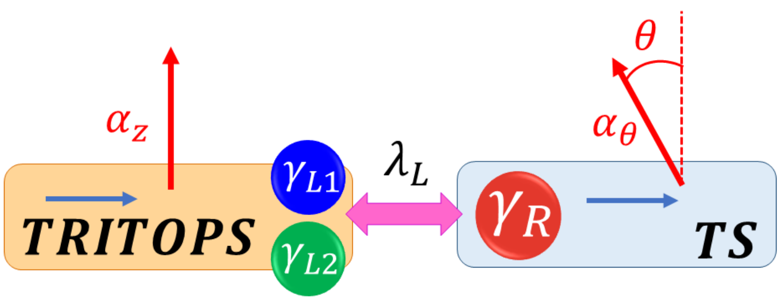

FIGURE 4.5: Sketch of a TRITOPS-TS Josephson junction. Colored dots indicate Majorana bound states corresponding to the Majorana operators $\gamma_{L1,L2,R}$. The tunnel coupling λ_L connects both wires, where blue arrows shows the positive momentum direction in each wire. The spin-orbit axes on both sides are tilted by the relative angle θ.

Chapter 5

Conclusion and Outlook

We close our discussions by summarizing our main findings. We studied the Josephson effect in different setups, conventional s-wave BCS superconductors and topologically nontrivial p-wave superconductors with Majorana end states were used. For the TS wires different models were used. The Kitaev chain describing a spinless topological superconductor in the deep topological regime, which allows analytical progress but makes it difficult to establish contact to experimental control parameters. We also used a spinful nanowire model for proximitized semiconductor nanowires and TRITOPS for differently realized topological superconductors. We generalized the boundary Green's function approach and obtained an analytical understanding of the roots of the corresponding secular polynomial in complex momentum space.

We found for the S-TS tunnel junction, that in the topological phase supercurrent is mainly carried by above-gap continuum contributions. The supercurrent blockade prevents a Josephson current in the deep topological regime, where the spinless theory is fully valid and no residual s-wave pairing exists. For realistic parameters a small but finite current is found. The Josephson current shows the usual 2π-periodic sinusoidal current-phase relation. The critical current depending on the bulk Zeeman field shows a kink-like feature at the critical value, caused by the sudden drop of Andreev state contribution.

The supercurrent blockade can be lifted by adding a magnetic impurity to the junction. We described the magnetic impurity as a spin-degenerate quantum dot with local magnetic field $\mathbf{B}$ and studied the corresponding S-QD-TS junction for spinless and spinful TS wires. From analytical results in the cotunneling regime and numerical results within the mean field approximation, we predict an anomalous Josephson effect with φ_0-junction behavior for the current-phase relation, when the TS wire is in the topological phase.

Another junction we studied is the S-TS-S junction, which allows for a Majorana-induced parity switch between Andreev state sectors with different parity. This observation could be useful for future microwave spectroscopy experiments of Andreev qubits in such contacts.

We used our gained understanding of the roots from the boundary Green's function method to study more junctions. The two examples we used were the trijunction of three spinful TS wires and a TRITOPS-TS junction. For both cases we analyzed the subgap Andreev state dispersion at zero temperature.

The introduced approaches are useful for further research. One could study the nonequilibrium transport properties or include electron-phonon effects. The results can be helpful for the interpretation of transport experiments carried out on hybrid devices containing nanowires with topologically nontrivial superconducting phases.

Chapter 6

Bibliography

[1] M. Tinkham, *Introduction to Superconductivity* , Dover Publications (1996).

[2] H. Bruus and K. Flensberg, *Many-body quantum theory in condensed matter physics*, Oxford University Press (2004).

[3] V. L. Ginzburg and L. D. Landau, *On the theory of superconductivity*, Zh. Eksp. Theor. Fiz. 20, 1064-1082 (1950).

[4] R. Egger, lecture notes *Theoretische Festkörperphysik*, Heinrich-Heine-Universität Düsseldorf, summer term 2013.

[5] H. K. Onnes, *The Superconductivity of Mercury*, Comm. Phys. Lab. Univ. Leiden, 122-124 (1911).

[6] W. Meissner, R. Ochsenfeld, *Ein neuer Effekt bei Eintritt der Supraleitfähigkeit*, Die Naturwissenschaften 21, 44, 787 (1933).

[7] J. Bardeen, L. N. Cooper and J. R. Schrieffer, *Theory of Superconductivity*, Phys. Rev. 108, 1175 (1957).

[8] B. D. Josephson, *Possible new effects in superconducting tunneling*, Physics Letters Vol. 1, Issue 7, 251 (1962).

[9] A. Zazunov, R. Egger, and A. Levy Yeyati, *Low-energy theory of transport in Majorana wire junctions*, Phys. Rev. B 94, 014502 (2016).

[10] M. Leijnse and K. Flensberg, *Introduction to topological superconductivity and Majorana fermions*, Semicond. Sci. Technol. 27, 124003 (2012).

[11] A. Kitaev, *Unpaired Majorana fermions in quantum wires*, Physics-Uspekhi, 44:131 (2001).

[12] L. Fu and C. L. Kane, *Superconducting proximity effect and Majorana fermions at the surface of a topological insulator*, Phys. Rev. Lett. 100, 096407 (2008).

[13] R. M. Lutchyn, J. D. Sau, and S. Das Sarma, *Majorana Fermions and a Topological Phase Transition in Semiconductor-Superconductor Heterostructures*, Phys. Rev. Lett. 105, 077001 (2010).

[14] Y. Oreg, G. Refael, and F. von Oppen, *Helical Liquids and Majorana Bound States in Quantum Wires*, Phys. Rev. Lett. 105, 177002 (2010).

[15] R. Holm and W. Meissner, *Messungen mit Hilfe von flüssigem Helium. XIII*, Z. Physik 74, 715–735 (1932).

[16] A. Altland and B. Simons, *Condensed Matter Field Theory*, Cambridge University Press, 2. Edition (2010).

[17] V. Fock and M. Born, *Beweis des adiabatensatzes*, Zeitschrift für Physik Volume 51, Issue 3-4, 165 (1928).

[18] D. J. Griffiths, *Introduction to quantum mechanics*, Prentice Hall International (1995).

[19] M. V. Berry, *Quantal phase factors accompanying adiabatic changes*, Proc. R. Soc. Lond. A 1984 392, 45 (1984).

[20] E. Majorana, *Teoria simmetrica dell'elettrone e del positrone*, Nuovo Cim 14, 171 (1937).

[21] C. L. Kane and M. Z. Hasan, *Topological insulators*, Rev. Mod. Phys. 82, 3045 (2010).

[22] J. Rammer, *Quantum Field Theory of Non-equilibrium States*, Cambridge University Press (2011).

[23] L. Keldysh, *Diagram technique for nonequilibrium processes*, Sov. Phys. JETP 20: 1018 (1965).

[24] T. Matsubara, *A New Approach to Quantum-Statistical Mechanics*, Prog. Theor. Phys. 14, 351 (1955).

[25] A. A. Abrikosov, *Methods of Quantum Field Theory in Statistical Physics*, Dover Publications (1975).

[26] G. C. Wick, *The Evaluation of the Collision Matrix*, Phys. Rev. 80, 268 (1950).

[27] J. R. Schrieffer and P. A. Wolff, *Relation between the Anderson and Kondo Hamiltonians*, Phys. Rev. 149, 491 (1966).

[28] Yu. V. Nazarov and Ya. M. Blanter, *Quantum Transport: Introduction to Nanoscience*, Cambridge University Press (2010).

[29] A. Zazunov, R. Egger, and A. Levy Yeyati, *Coulomb blockade of Majorana-fermion-induced transport*, Phys. Rev. B 84, 165440 (2011).

[30] A. Zazunov, R. Egger, M. Alvarado, and A. Levy Yeyati, *Josephson effect in multiterminal topological junctions*, Phys. Rev. B 96, 024516 (2017).

[31] A. Zazunov and R. Egger, *Supercurrent blockade in Josephson junctions with a Majorana wire*, Phys. Rev. B 85, 104514 (2012).

[32] A. Zazunov, R. Egger, T. Jonckheere, and T. Martin, *Anomalous Josephson Current through a Spin-Orbit Coupled Quantum Dot*, Phys. Rev. Lett. 103, 147003 (2009).

[33] A. Buzdin, *Direct Coupling Between Magnetism and Superconducting Current in the Josephson ϕ_0 Junction*, Phys. Rev. Lett. 101, 107005 (2008).

[34] A. Brunetti, A. Zazunov, A. Kundu, and R. Egger, *Anomalous Josephson current, incipient time-reversal symmetry breaking, and Majorana bound states in interacting multilevel dots*, Phys. Rev. B 88, 144515 (2013).

[35] C. Schrade, S. Hoffman, and D. Loss, *Detecting topological superconductivity with ϕ_0 Josephson junctions* Phys. Rev. B 95, 195421 (2017).

[36] R. Aguado, *Majorana quasiparticles in condensed matter*, Rivista Nuovo Cimento 11, 523 (2017).

[37] M.T. Deng, S. Vaitiekenas, E.B. Hansen, J. Danon, M. Leijnse, K. Flensberg, J. Nygård, P. Krogstrup, and C.M. Marcus, *Majorana bound states in a coupled quantum-dot hybrid-nanowire system*, Science 354, 1557 (2016).

[38] M. Leijnse and K. Flensberg, *Quantum Information Transfer between Topological and Spin Qubit Systems*, Phys. Rev. Lett. 107, 210502 (2011).

[39] D. Sticlet, C. Bena, and P. Simon, *Spin and Majorana Polarization in Topological Superconducting Wires*, Phys. Rev. Lett. 108, 096802 (2012).

[40] E. Prada, P. San-Jose, and R. Aguado, *Transport spectroscopy of NS nanowire junctions with Majorana fermions* Phys. Rev. B 86, 180503(R) (2012).

[41] E. Prada, R. Aguado, and P. San-Jose, *Measuring Majorana nonlocality and spin structure with a quantum dot*, Phys. Rev. B 96, 085418 (2017).

[42] S. Hoffman, D. Chevallier, D. Loss, and J. Klinovaja, *Spin-dependent coupling between quantum dots and topological quantum wires*, Phys. Rev. B 96, 045440 (2017).

[43] A. Martín-Rodero and A. L. Yeyati, *Josephson and Andreev transport through quantum dots*, Adv. Phys. 60, 899 (2011).

[44] J. Alicea, *New directions in the pursuit of Majorana fermions in solid state systems*, Rep. Prog. Phys. 75, 076501 (2012).

[45] L. Arrachea, G. S. Lozano, and A. A. Aligia, *Thermal transport in one-dimensional spin heterostructures*, Phys. Rev. B 80, 014425 (2009).

[46] R. M. Lutchyn, T. D. Stanescu, and S. Das Sarma, *Search for Majorana Fermions in Multiband Semiconducting Nanowires*, Phys. Rev. Lett. 106, 127001 (2011).

[47] B. D. Woods, J. Chen, S. M. Frolov, and T. D. Stanescu, *Zero-energy pinning of topologically trivial bound states in multiband semiconductor-superconductor nanowires*, Phys. Rev. B 100, 125407 (2019).

[48] R. S. K. Mong and V. Shivamoggi, *Edge states and the bulk-boundary correspondence in Dirac Hamiltonians*, Phys. Rev. B 83, 125109 (2011).

[49] A. A. Aligia and L. Arrachea, *Entangled end states with fractionalized spin projection in a time-reversal-invariant topological superconducting wire*, Phys. Rev. B 98, 174507 (2018).

[50] X.-L. Qi, T. L. Hughes, and S.-C. Zhang, *Topological invariants for the Fermi surface of a time-reversal-invariant superconductor*, Phys. Rev. B 1, 134508 (2010).

[51] T. Jonckheere, J. Rech, A. Zazunov, R. Egger, A. L. Yeyati, and T. Martin, *Giant shot noise from Majorana zero modes in topological trijunctions*, Phys. Rev. Lett. 122, 097003 (2019).

[52] P. Wei, S. Manna, M. Eich, P. Lee, and J. Moodera, *Superconductivity in the Surface State of Noble Metal Gold and its Fermi Level Tuning by EuS Dielectric*, Phys. Rev. Lett. 122, 247002 (2019).

[53] C. L. M. Wong and K. T. Law, *Majorana Kramers doublets in $d_{x^2y^2}$-wave superconductors with Rashba spin-orbit coupling*, Phys. Rev. B 86, 184516 (2012).

[54] S. Nakosai, Y. Tanaka, and N. Nagaosa, *Topological Superconductivity in Bilayer Rashba System*, Phys. Rev. Lett. 108, 147003 (2012).

[55] S. Deng, L. Viola, and G. Ortiz, *Majorana Modes in Time-Reversal Invariant s-Wave Topological Superconductors*, Phys. Rev. Lett. 108, 036803 (2012).

[56] F. Zhang, C. L. Kane, and E. J. Mele, *Time-Reversal-Invariant Topological Superconductivity and Majorana Kramers Pairs*, Phys. Rev. Lett. 111, 056402 (2013).

[57] A. Keselman, L. Fu, A. Stern, and E. Berg, *Inducing Time-Reversal-Invariant Topological Superconductivity and Fermion Parity Pumping in Quantum Wires*, Phys. Rev. Lett. 111, 116402 (2013).

[58] E. Dumitrescu and S. Tewari, *Topological properties of the time-reversal-symmetric Kitaev chain and applications to organic superconductors*, Phys. Rev. B 88, 220505(R) (2013).

[59] S. B. Chung, J. Horowitz, and X.-L. Qi, *Time-reversal anomaly and Josephson effect in time-reversal-invariant topological superconductors*, Phys. Rev. B 88, 214514 (2013).

[60] S. Nakosai, J. C. Budich, Y. Tanaka, B. Trauzettel, and N. Nagaosa, *Majorana Bound States and Nonlocal Spin Correlations in a Quantum Wire on an Unconventional Superconductor*, Phys. Rev. Lett. 110, 117002 (2013).

[61] A. Haim, A. Keselman, E. Berg, and Y. Oreg, *Time-reversal-invariant topological superconductivity induced by repulsive interactions in quantum wires*, Phys. Rev. B 89, 220504(R) (2014).

[62] E. Gaidamauskas, J. Paaske, and K. Flensberg, *Majorana Bound States in Two-Channel Time-Reversal-Symmetric Nanowire Systems*, Phys. Rev. Lett. 112, 126402 (2014).

[63] J. Klinovaja, A. Yacoby, and D. Loss, *Kramers pairs of Majorana fermions and parafermions in fractional topological insulators*, Phys. Rev. B 90, 155447 (2014).

[64] C. Schrade, A. A. Zyuzin, J. Klinovaja, and D. Loss, *Proximity-Induced π Josephson Junctions in Topological Insulators and Kramers Pairs of Majorana Fermions*, Phys. Rev. Lett. 115, 237001 (2015).

[65] A. Haim, E. Berg, K. Flensberg, and Y. Oreg, *No-go theorem for a time-reversal invariant topological phase in noninteracting systems coupled to conventional superconductors*, Phys. Rev. B 94, 161110(R) (2016).

[66] Y. Kim, D. E. Liu, E. Gaidamauskas, J. Paaske, K. Flensberg, and R. M. Lutchyn, *Signatures of Majorana Kramers pairs in superconductor-Luttinger liquid and superconductor-quantum dot-normal lead junctions*, Phys. Rev. B 94, 075439 (2016).

[67] E. Mellars and B. Béri, *Signatures of time-reversal-invariant topological superconductivity in the Josephson effect*, Phys. Rev. B 94, 174508 (2016).

[68] A. Camjayi, L. Arrachea, A. Aligia, and F. von Oppen, *Fractional Spin and Josephson Effect in Time-Reversal-Invariant Topological Superconductors*, Phys. Rev. Lett. 119, 046801 (2017).

[69] C. Schrade and L. Fu, *Parity-Controlled* 2π *Josephson Effect Mediated by Majorana Kramers Pairs*, Phys. Rev. Lett. 120, 267002 (2018).

[70] A. Haim and Y. Oreg, *Time-reversal-invariant topological superconductivity in one and two dimensions*, Phys. Rep. 825, 1 (2019).

Appendix A

Publications

A.1 Josephson effect in junctions of conventional and topological superconductors

A. Zazunov, A. Iks, M. Alvarado, A. Levy Yeyati, and R. Egger, Josephson effect in junctions of conventional and topological superconductors, Beilstein J. Nanotechnol. 9, 1659 (2018)

My contribution in this paper was in scientific discussions, work and preparation of the manuscript. I did analytical calculations for the S-QD-TS model and did numerical analysis for the spinful models S-TS and S-QD-TS.

BEILSTEIN JOURNAL OF NANOTECHNOLOGY

Josephson effect in junctions of conventional and topological superconductors

Alex Zazunov[1], Albert Iks[1], Miguel Alvarado[2], Alfredo Levy Yeyati[2] and Reinhold Egger[*1]

Full Research Paper

Open Access

Address:
[1]Institut für Theoretische Physik, Heinrich-Heine-Universität, D-40225 Düsseldorf, Germany and [2]Departamento de Física Teórica de la Materia Condensada C-V, Condensed Matter Physics Center (IFIMAC) and Instituto Nicolás Cabrera, Universidad Autónoma de Madrid, E-28049 Madrid, Spain

Email:
Reinhold Egger[*] - egger@hhu.de

* Corresponding author

Keywords:
Andreev bound states; Josephson current–phase relation; Majorana zero modes; topological superconductivity

Beilstein J. Nanotechnol. **2018,** *9,* 1659–1676.
doi:10.3762/bjnano.9.158

Received: 30 January 2018
Accepted: 27 April 2018
Published: 06 June 2018

This article is part of the Thematic Series "Topological materials".

Associate Editor: J. M. van Ruitenbeek

Abstract

We present a theoretical analysis of the equilibrium Josephson current-phase relation in hybrid devices made of conventional *s*-wave spin-singlet superconductors (S) and topological superconductor (TS) wires featuring Majorana end states. Using Green's function techniques, the topological superconductor is alternatively described by the low-energy continuum limit of a Kitaev chain or by a more microscopic spinful nanowire model. We show that for the simplest S–TS tunnel junction, only the *s*-wave pairing correlations in a spinful TS nanowire model can generate a Josephson effect. The critical current is much smaller in the topological regime and exhibits a kink-like dependence on the Zeeman field along the wire. When a correlated quantum dot (QD) in the magnetic regime is present in the junction region, however, the Josephson current becomes finite also in the deep topological phase as shown for the cotunneling regime and by a mean-field analysis. Remarkably, we find that the S–QD–TS setup can support φ_0-junction behavior, where a finite supercurrent flows at vanishing phase difference. Finally, we also address a multi-terminal S–TS–S geometry, where the TS wire acts as tunable parity switch on the Andreev bound states in a superconducting atomic contact.

Introduction

The physics of topological superconductors (TSs) is being vigorously explored at present. After Kitaev [1] showed that a one-dimensional (1D) spinless fermionic lattice model with nearest-neighbor *p*-wave pairing ('Kitaev chain') features a topologically nontrivial phase with Majorana bound states (MBSs) at open boundaries, references [2,3] have pointed out that the physics of the Kitaev chain could be realized in spin–orbit coupled nanowires with a magnetic Zeeman field and in the proximity to a nearby *s*-wave superconductor. The spinful nanowire model of references [2,3] indeed features *p*-wave pairing correlations for appropriately chosen model parameters. In addition, it also contains *s*-wave pairing correlations which become gradually smaller as one moves into the deep topological regime. Topologically nontrivial hybrid semiconductor nanowire devices are of considerable interest in the context of quantum information processing [4-12], and they may also be designed in two-dimensional layouts by means of gate lithography techniques. Over the last few years, several experiments employing such platforms have provided mounting evidence for MBSs, e.g., from zero-bias conductance peaks in N–TS junctions (where N stands for a normal-conducting lead) and via signatures of the 4π-periodic Josephson effect in TS–TS junctions [13-25]. Related MBS phenomena have been reported for other material platforms as well [26-30], and most of the results reported below also apply to those settings. Available materials are often of sufficiently high quality to meet the conditions for ballistic transport, and we will therefore neglect disorder effects.

In view of the large amount of published theoretical works on the Josephson effect in such systems, let us first motivate the present study. (For a more detailed discussion and references, see below.) Our manuscript addresses the supercurrent flowing in Josephson junctions with a magnetic impurity. By considering Josephson junctions between a topological superconductor and a non-topological superconductor, we naturally extend previous works on Josephson junctions with a magnetic impurity between two conventional superconductors, as well as other works on Josephson junctions between topological and non-topological superconductors but without a magnetic impurity. In the simplest description, Josephson junctions between topological and non-topological supeconductors carry no supercurrent. Instead, a supercurrent can flow only with certain deviations from the idealized model description. The presence of a magnetic impurity in the junction is one of these deviations, and this effect allows for novel signatures for the topological transition via the so-called φ_0-behavior and/or through the kink-like dependence of the critical current on a Zeeman field driving the transition. We consider two different geometries in various regimes, e.g., the cotunneling regime where a controlled perturbation theory is possible, and a mean-field description of the stronger-coupling regime. We study both idealized Hamiltonians (allowing for analytical progress) as well as more realistic models for the superconductors.

To be more specific, we address the equilibrium current–phase relation (CPR) in different setups involving both conventional s-wave BCS superconductors ('S' leads) and TS wires, see Figure 1 for a schematic illustration. In general, the CPR is closely related to the Andreev bound state (ABS) spectrum of the system. For S–TS junctions with the TS wire deep in the topological phase such that it can be modeled by a Kitaev chain, the supercurrent vanishes identically [31]. This supercurrent blockade can be traced back to the different (s/p-wave) pairing symmetries for the S/TS leads, together with the fact that MBSs have a definite spin polarization. For an early study of Josephson currents between superconductors with different (p/d) pairing symmetries, see also [32]. A related phenomenon concerns Multiple Andreev Reflection (MAR) features in nonequilibrium superconducting quantum transport at subgap voltages [33-36]. Indeed, it has been established that MAR processes are absent in S–TS junctions (with the TS wire in the deep topological regime) such that only quasiparticle transport above the gap is possible [37-44].

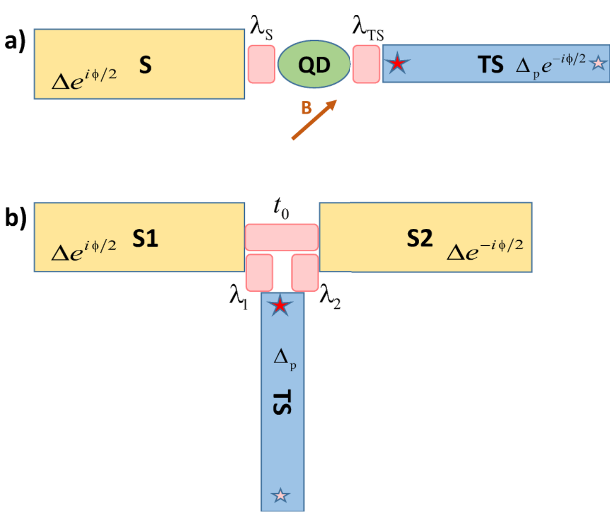

Figure 1: Schematic setups studied in this paper. a) S–QD–TS geometry: S denotes a conventional s-wave BCS superconductor with order parameter $\Delta e^{i\phi/2}$, and TS represents a topologically nontrivial superconducting wire with MBSs (shown as stars) and proximity-induced order parameter $\Delta_p e^{-i\phi/2}$. The interface contains a quantum dot (QD) corresponding to an Anderson impurity, connected to the S/TS leads by tunnel amplitudes $\lambda_{S/TS}$ (light red). The QD is also exposed to a local Zeeman field **B**. b) S–TS–S geometry: Two conventional superconductors (S1 and S2) with the same gap Δ and a TS wire with proximity gap Δ_p form a trijunction. The order parameter phase of S1 (S2), $\phi_1 = \phi/2$ ($\phi_2 = -\phi/2$), is taken relative to the phase of the TS wire, and tunnel couplings $\lambda_{1/2}$ connect S1/S2 to the TS wire. When the TS wire is decoupled ($\lambda_{1,2} = 0$), the S–S junction becomes a standard SAC with transparency $\mathcal{T}$ determined by the tunnel amplitude t_0, see Equation 42.

There are several ways to circumvent this supercurrent blockade in S–TS junctions. (i) One possibility has been described in [43]. For a trijunction formed by two TS wires and one S lead, crossed Andreev reflections allow for the nonlocal splitting of Cooper pairs in the S electrode involving both TS wires (or the reverse process). In this way, an equilibrium supercurrent will be generated unless the MBS spin polarization axes of both TS wires are precisely aligned. (ii) Even for a simple S–TS junction, a finite Josephson current is expected when the TS wire is modeled as spinful nanowire. This effect is due to the residual s-wave pairing character of the spinful TS model [2,3]. Interestingly, upon changing a control parameter, e.g., the bulk Zeeman field, which drives the TS wire across the topological phase transition, we find that the critical current exhibits a kink-like feature that is mainly caused by a suppression of the Andreev state contribution in the topological phase. (iii) Yet another possibility is offered by junctions containing a magnetic impurity in a local magnetic field. We here analyze the S–QD–TS setup in Figure 1a in some detail, where a quantum dot (QD) is present within the S–TS junction region. The QD is modeled as an Anderson impurity [36], which is equivalent to a spin-1/2 quantum impurity over a wide parameter regime. Once spin mixing is induced by the magnetic impurity and the local magnetic field, we predict that a finite Josephson current flows even in the deep topological limit. In particular, in the cotunneling regime, we find an anomalous Josephson effect with finite supercurrent at vanishing phase difference (φ_0-junction behavior) [45-47], see also [48-51]. The 2π-periodic CPR found in S–QD–TS junctions could thereby provide independent evidence for MBSs via the anomalous Josephson effect. In addition, we compute the CPR within the mean-field approximation in order to go beyond perturbation theory in the tunnel couplings connecting the QD to the superconducting leads. Our mean-field analysis shows that the φ_0-junction behavior is a generic feature for S–QD–TS devices in the topological regime which is not limited to the cotunneling regime.

In the final part of the paper, we turn to the three-terminal S–TS–S setup shown in Figure 1b, where the S–S junction by itself (with the TS wire decoupled) represents a standard superconducting atomic contact (SAC) with variable transparency of the weak link. Recent experiments have demonstrated that the many-body ABS configurations of a SAC can be probed and manipulated to high accuracy by microwave spectroscopy [52-54]. When the TS wire is coupled to the S–S junction, see Figure 1b, the Majorana end state acts as a parity switch on the ABS system of the SAC. This effect allows for additional functionalities in Andreev spectroscopy. We note that similar ideas have also been explored for TS–N–TS systems [55].

Results and Discussion

S–QD–TS junction

Model

Let us start with the case of an S–QD–TS junction, where an interacting spin-degenerate single-level quantum dot (QD) is sandwiched between a conventional *s*-wave superconductor (S) and a topological superconductor (TS). This geometry is shown in Figure 1a. The corresponding topologically trivial S–QD–S problem has been studied in great detail over the past decades both theoretically [56-63] and experimentally [64-69]. A main motivation for those studies came from the fact that the QD can be driven into the magnetic regime where it represents a spin-1/2 impurity subject to Kondo screening by the leads. The Kondo effect then competes against the superconducting bulk gap and one encounters local quantum phase transitions. By now, good agreement between experiment and theory has been established. Rather than studying the fate of the Kondo effect in the S–QD–TS setting of Figure 1a, we here pursue two more modest goals. First, we shall discuss the cotunneling regime in detail, where one can employ perturbation theory in the dot–lead couplings. This regime exhibits π-junction behavior in the S–QD–S case [56]. Second, in order to go beyond the cotunneling regime, we have performed a mean-field analysis similar in spirit to earlier work for S–QD–S devices [57,58].

The Hamiltonian for the setup in Figure 1a is given by

$$H = H_{\mathrm{S}} + H_{\mathrm{TS}} + H_{\mathrm{QD}} + H_{\mathrm{tun}}\,, \tag{1}$$

where $H_{\mathrm{S/TS}}$ and H_{QD} describe the semi-infinite S/TS leads and the isolated dot in between, respectively, and H_{tun} refers to the tunnel contacts. We often use units with $e = \hbar = k_{\mathrm{B}} = 1$, and $\beta = 1/T$ denotes inverse temperature. The QD is modeled as an Anderson impurity [36], i.e., a single spin-degenerate level of energy ε_0 with repulsive on-site interaction energy $U > 0$,

$$H_{\mathrm{QD}} = \sum_{\sigma=\uparrow,\downarrow} \varepsilon_0 \left(n_\sigma - \frac{1}{2} \right) + U n_\uparrow n_\downarrow - \mathbf{B}\cdot\mathbf{S}\,, \tag{2}$$

where the QD occupation numbers are $n_\sigma = d_\sigma^\dagger d_\sigma = 0,1$, with dot fermion operators d_σ and $d_\sigma^\dagger$ for spin σ. Using standard Pauli matrices $\sigma_{x,y,z}$, we define

$$\mathbf{S}_{i=x,y,z} = \sum_{\sigma,\sigma'} d_\sigma^\dagger \left(\sigma_i\right)_{\sigma\sigma'} d_{\sigma'}\,, \tag{3}$$

such that $\mathbf{S}/2$ is a spin-1/2 operator. In the setup of Figure 1a, we also take into account an external Zeeman field $\mathbf{B} = (B_x, B_y, B_z)$ acting on the QD spin, where the units in Equation 2 include gyromagnetic and Bohr magneton factors. The spinful nanowire proposal for TS wires [2,3] also requires a sufficiently strong bulk Zeeman field oriented along the wire in order to realize the topologically nontrivial phase, but for concreteness, we here imagine the field $\mathbf{B}$ as independent local field coupled only to the QD spin. One could use, e.g., a ferromagnetic grain near the QD to generate it. This field here plays a crucial role because for $\mathbf{B} = 0$, the S+QD part is spin rotation [SU(2)] invariant and the arguments of [31] then rule out a supercurrent for TS wires in the deep topological regime. We show below that unless $\mathbf{B}$ is inadvertently aligned with the MBS spin polarization axis, spin mixing will indeed generate a supercurrent.

The S/TS leads are coupled to the QD via a tunneling Hamiltonian [70],

$$H_{\text{tun}} = \lambda_S \sum_{\sigma=\uparrow,\downarrow} \Psi_\sigma^\dagger d_\sigma + \lambda_{TS} e^{-i\phi/2} \Psi^\dagger d_\uparrow + \text{h.c.}, \tag{4}$$

where ψ_σ and ψ are boundary fermion fields representing the S lead and the effectively spinless TS lead, respectively. For the S lead, we assume the usual BCS model [62], where the operator ψ_σ annihilates an electron with spin σ at the junction. The TS wire will, for the moment, be described by the low-energy Hamiltonian of a Kitaev chain in the deep topological phase with chemical potential $\mu = 0$ [1,5]. The corresponding fermion operator ψ at the junction includes both the MBS contribution and above-gap quasiparticles [40]. Without loss of generality, we choose the unit vector $\hat{e}_z$ as the MBS spin polarization direction and take real-valued tunnel amplitudes $\lambda_{S/TS}$, see Figure 1a, using a gauge where the superconducting phase difference ϕ appears via the QD–TS tunneling term. These tunnel amplitudes contain density-of-states factors for the respective leads. The operator expression for the current flowing through the system is then given by

$$\hat{I} = \frac{2e}{\hbar} \partial_\phi H_{\text{tun}}. \tag{5}$$

We do not specify $H_{S/TS}$ in Equation 1 explicitly since within the imaginary-time (τ) boundary Green's function (bGF) formalism [40] employed here, we only need to know the bGFs. For the S lead with gap value Δ, the bGF has the Nambu matrix form [40]

$$\begin{aligned} g(\tau) &= -\left\langle \mathcal{T}_\tau \Psi_S(\tau) \Psi_S^\dagger(0) \right\rangle_0 = \beta^{-1} \sum_\omega e^{-i\omega\tau} g(\omega), \\ \Psi_S &= \begin{pmatrix} \Psi_\uparrow \\ \Psi_\downarrow^\dagger \end{pmatrix}, \qquad g(\omega) = -\frac{i\omega\tau_0 + \Delta\tau_x}{\sqrt{\omega^2 + \Delta^2}}, \end{aligned} \tag{6}$$

where the expectation value $\langle \ldots \rangle_0$ refers to an isolated S lead, $\mathcal{T}$ denotes time ordering, ω runs over fermionic Matsubara frequencies, i.e., $\omega = 2\pi(n + 1/2)/\beta$ with integer n, and we define Pauli (unity) matrices $\tau_{x,y,z}$ (τ_0) in particle–hole space corresponding to the Nambu spinor Ψ_S. Similarly, for a TS lead with proximity-induced gap Δ_p, the low-energy limit of a Kitaev chain yields the bGF [40]

$$\begin{aligned} G(\tau) &= -\left\langle \mathcal{T}_\tau \Psi_{TS}(\tau) \Psi_{TS}^\dagger(0) \right\rangle_0, \quad \Psi_{TS} = \begin{pmatrix} \Psi \\ \Psi^\dagger \end{pmatrix}, \\ G(\omega) &= \frac{1}{i\omega} \left(\sqrt{\omega^2 + \Delta_p^2}\, \tau_0 + \Delta_p \tau_x \right). \end{aligned} \tag{7}$$

The matrices $\tau_{0,x}$ here act in the Nambu space defined by the spinor Ψ_{TS}. Later on we will address how our results change when the TS wire is modeled as spinful nanowire [2,3], where the corresponding bGF has been specified in [43]. We emphasize that the bGF (Equation 7) captures the effects of both the MBS (via the $1/\omega$ term) and of the above-gap continuum quasiparticles (via the square root) [40,71].

In most of the following discussion, we will assume that U is the dominant energy scale, with the single-particle level located at $\varepsilon_0 \approx -U/2$. In that case, low-energy states with energy well below U are restricted to the single occupancy sector,

$$n_\uparrow + n_\downarrow = 1, \tag{8}$$

and the QD degrees of freedom become equivalent to the spin-1/2 operator $\mathbf{S}/2$ in Equation 3. In this regime, the QD acts like a magnetic impurity embedded in the S–TS junction. Using a Schrieffer–Wolff transformation to project the full Hamiltonian to the Hilbert subspace satisfying Equation 8, $H \to H_{\text{eff}}$, one arrives at the effective low-energy Hamiltonian

$$H_{\text{eff}} = H_0 + H_{\text{int}}, \quad H_0 = H_S + H_{TS} - \mathbf{B}\cdot\mathbf{S}, \tag{9}$$

with the interaction term

$$\begin{aligned} H_{\text{int}} = & -\frac{2}{U} \sum_{\sigma,\sigma'} \left(\eta_\sigma^\dagger d_\sigma d_{\sigma'}^\dagger \eta_{\sigma'} + \text{h.c.} \right) \\ &= \frac{2}{U} \sum_{\sigma=\uparrow/\downarrow=\pm} \left(\sigma S_z \eta_\sigma^\dagger \eta_\sigma + S_\sigma \eta_{-\sigma}^\dagger \eta_\sigma \right) \\ &+ \frac{2}{U} \delta n \sum_\sigma \eta_\sigma^\dagger \eta_\sigma - \frac{2\Lambda}{U} (\delta n + 1), \end{aligned} \tag{10}$$

where $S_\pm = S_x \pm iS_y$ and $\delta n = \sum_\sigma n_\sigma - 1$. Moreover, $\Lambda = \left[\eta_\sigma, \eta_\sigma^\dagger\right]_+$ is the anticommutator of the composite boundary fields

$$\eta_\sigma = \lambda_S \Psi_\sigma + \delta_{\sigma,\uparrow} \lambda_{TS} e^{i\phi/2} \Psi. \tag{11}$$

We note that Λ is real-valued and does not depend on ϕ. Due to the constraint (Equation 8) on the dot occupation, the last two terms in Equation 10 do not contribute to the system dynamics and we obtain

$$\begin{aligned} H_{\text{int}} &= \frac{4}{U} \sum_{\sigma,\sigma'} \mathcal{Q}_{\sigma\sigma'} \eta_\sigma^\dagger \eta_{\sigma'}, \\ \mathcal{Q}_{\sigma\sigma} &= \frac{\sigma}{2} S_z, \quad \mathcal{Q}_{\sigma,-\sigma} = \frac{1}{2} S_{-\sigma}. \end{aligned} \tag{12}$$

A formally exact expression for the partition function is then given by

$$Z = \mathrm{Tr}\big|_{\delta n=0}\left(e^{-\beta H_0}\mathcal{T}_\tau e^{-\int_0^\beta d\tau H_{\mathrm{int}}(\tau)}\right), \tag{13}$$

where $H_{\mathrm{int}}(\tau) = e^{\tau H_0} H_{\mathrm{int}} e^{-\tau H_0}$ with H_0 in Equation 9 and the trace extends only over the Hilbert subspace corresponding to Equation 8. We can equivalently write Equation 13 in the form

$$\begin{aligned} Z &= Z_0 \left\langle \mathcal{T}_\tau e^{-\beta \hat{W}} \right\rangle_0 = e^{-\beta F}, \\ \hat{W} &= \beta^{-1}\int_0^\beta d\tau H_{\mathrm{int}}(\tau), \\ Z_0 &= \mathrm{Tr}\big|_{\delta n=0}\, e^{-\beta H_0} = e^{-\beta F_0}, \end{aligned} \tag{14}$$

where F is the free energy. The Josephson current then follows as $I = (2e/\hbar)\,\partial_\phi F$, see Equation 5.

Cotunneling regime

We now address the CPR in the elastic cotunneling regime,

$$\lambda_{\mathrm{S}}\lambda_{\mathrm{TS}} \ll \min\left\{\Delta, \Delta_{\mathrm{p}}, U\right\}, \tag{15}$$

where perturbation theory in H_{int} is justified. We thus wish to compute the free energy $F(\phi)$ from Equation 14 to lowest nontrivial order. With $W_0 = \langle \hat{W} \rangle_0$, the standard cumulant expansion gives

$$F - F_0 = W_0 - \frac{\beta}{2}\left(\left\langle \hat{W}^2 \right\rangle_0 - W_0^2\right) + \mathcal{O}(W)^2. \tag{16}$$

By virtue of Wick's theorem, time-ordered correlation functions of the boundary operators (Equation 11) are now expressed in terms of S/TS bGF matrix elements, see Equation 6 and Equation 7,

$$\left\langle \mathcal{T}_\tau \eta_\sigma(\tau)\eta^\dagger_{\sigma'}(0)\right\rangle_0 = \delta_{\sigma\sigma'}\begin{bmatrix} \lambda_{\mathrm{S}}^2 \left\langle \mathcal{T}_\tau \Psi_\sigma(\tau)\Psi^\dagger_\sigma(0)\right\rangle_0 \\ +\delta_{\sigma,\uparrow}\lambda_{\mathrm{TS}}^2 \left\langle \mathcal{T}_\tau \Psi(\tau)\Psi^\dagger(0)\right\rangle_0 \end{bmatrix} \tag{17}$$

and similarly

$$\begin{aligned}\left\langle \mathcal{T}_\tau \eta_\sigma(\tau)\eta_{\sigma'}(0)\right\rangle_0 = \;& \delta_{\sigma,-\sigma'}\lambda_{\mathrm{S}}^2 \left\langle \mathcal{T}_\tau \Psi_\sigma(\tau)\Psi_{-\sigma}(0)\right\rangle_0 \\ &+ e^{i\phi}\delta_{\sigma\sigma'}\delta_{\sigma,\uparrow}\lambda_{\mathrm{TS}}^2 \left\langle \mathcal{T}_\tau \Psi(\tau)\Psi(0)\right\rangle_0 . \end{aligned} \tag{18}$$

Next we observe that $\partial_\phi \langle H_{\mathrm{int}}\rangle_0 = 0$. As a consequence, the ϕ-independent terms W_0 and W_0^2 in Equation 16 do not contribute to the Josephson current. The leading contribution is then of second order in H_{int},

$$\begin{aligned} I(\phi) &= -\beta^{-1}\partial_\phi \int_0^\beta d\tau_1 d\tau_2 \left\langle \mathcal{T}_\tau H_{\mathrm{int}}(\tau_1) H_{\mathrm{int}}(\tau_2)\right\rangle_0 \\ &= -\frac{\kappa^2}{\beta}\int_0^\beta d\tau_1 d\tau_2\, g_{12}(\tau_1-\tau_2) G_{12}(\tau_1-\tau_2) \\ &\quad \times i e^{i\phi}\sum_\sigma \sigma \left\langle \mathcal{T}_\tau \mathcal{Q}_{\sigma,\uparrow}(\tau_1)\mathcal{Q}_{-\sigma,\uparrow}(\tau_2)\right\rangle_0 + \mathrm{h.c.}, \end{aligned} \tag{19}$$

with $\mathcal{Q}_{\sigma,\sigma'}$ in Equation 12 and the small dimensionless parameter

$$\kappa = \frac{4\lambda_{\mathrm{S}}\lambda_{\mathrm{TS}}}{U} \ll 1. \tag{20}$$

From Equation 6 and Equation 7, the bGF matrix elements needed in Equation 19 follow as

$$\begin{aligned} g_{12}(\tau) &= -\frac{\Delta}{\beta}\sum_\omega \frac{\cos(\omega\tau)}{\sqrt{\omega^2+\Delta^2}}, \\ G_{12}(\tau) &= -\frac{\Delta_{\mathrm{p}}}{\beta}\sum_\omega \frac{\sin(\omega\tau)}{\omega} \simeq -\frac{\Delta_{\mathrm{p}}}{2}\mathrm{sgn}(\tau). \end{aligned} \tag{21}$$

Now $|g_{12}(\tau)|$ is exponentially small unless $\Delta|\tau| < 1$. In particular, $g_{12}(\tau) \to -\delta(\tau)$ for $\Delta \to \infty$. Moreover, for $B \ll \Delta$ with $B \equiv |\mathbf{B}|$, the magnetic impurity (**S**) dynamics will be slow on time scales of the order of $1/\Delta$. We may therefore approximate the spin–spin correlators in Equation 19 by their respective equal-time expressions,

$$\lim_{\tau_1\to\tau_2}\left\langle \mathcal{T}_\tau \mathcal{Q}_{\sigma,\uparrow}(\tau_1)\mathcal{Q}_{-\sigma,\uparrow}(\tau_2)\right\rangle_0 = \frac{\sigma}{4}\mathrm{sgn}(\tau_1-\tau_2)\langle S_{+\tau_1}\rangle_0 . \tag{22}$$

Inserting Equation 21 and Equation 22 into the expression for the supercurrent in Equation 19, the time integrations can be carried out analytically.

We obtain the CPR in the cotunneling regime as

$$\begin{aligned} I(\phi) &= I_x \sin\phi + I_y \cos\phi, \\ I_{x,y} &= \frac{e\kappa^2\Delta_{\mathrm{p}}}{2\hbar}\frac{B_{x,y}}{B}\tanh(\beta B), \end{aligned} \tag{23}$$

with κ in Equation 20. We note that while $I(\phi)$ is formally independent of Δ, the value of Δ must be sufficiently large to justify the steps leading to Equation 23. Remarkably, Equation 23 predicts anomalous supercurrents for the S–QD–TS setup, i.e., a finite Josephson current for vanishing phase difference ($\phi = 0$) [45,46,72]. One can equivalently view this effect as a φ_0-shift in the CPR, $I(\phi) = I_c \sin(\phi + \varphi_0)$. An observation of this φ_0-junction behavior could then provide additional evidence for MBSs (see also [47]), where Equation 23 shows that the local magnetic field is required to have a finite B_y-component with $\hat{e}_z$ defining the MBS spin polarization direction. In particular, if $\mathbf{B}$ is aligned with $\hat{e}_z$, the supercurrent in Equation 23 vanishes identically since *s*-wave Cooper pairs cannot tunnel from the S lead into the TS wire in the absence of spin flips [31]. Otherwise, the CPR is 2π-periodic and sensitive to the MBS through the peculiar dependence on the relative orientation between the MBS spin polarization ($\hat{e}_z$) and the local Zeeman field $\mathbf{B}$ on the QD. The fact that $B_y \neq 0$ (rather than $B_x \neq 0$) is necessary to have $\varphi_0 \neq 0$ can be traced back to our choice of real-valued tunnel couplings. For tunable tunnel phases, also the field direction where one has $\varphi_0 = 0$ will vary accordingly.

Noting that the anomalous Josephson effect has recently been observed in S–QD–S devices [73], we expect that similar experimental techniques will allow to access the CPR (Equation 23). We mention in passing that previous work has also pointed out that experiments employing QDs between N (instead of S) leads and TS wires can probe nonlocal effects due to MBSs [12,16,74-78]. In our case, e.g., by variation of the field direction in the *xy*-plane, Equation 23 predicts a tunable anomalous supercurrent. We conclude that in the cotunneling regime, the π-junction behavior of S–QD–S devices is replaced by the more exotic physics of φ_0-junctions in the S–QD–TS setting.

Mean-field approximation

Next we present a mean-field analysis of the Hamiltonian (Equation 1) which allows us to go beyond the perturbative cotunneling regime. For the corresponding S–QD–S case, see [58,79]. We note that a full solution of this interacting many-body problem requires a detailed numerical analysis using, e.g., the numerical renormalization group [60,61] or quantum Monte Carlo simulations [59,63], which is beyond the scope of the present work. We start by defining the GF of the QD,

$$G_d(\tau) = -\left\langle \mathcal{T}_\tau \Psi_d(\tau) \Psi_d^\dagger(0) \right\rangle, \quad \Psi_d^\dagger = \left(d_\uparrow^\dagger, d_\downarrow, d_\downarrow^\dagger, -d_\uparrow \right)^T. \quad (24)$$

Note that this notation introduces double counting, which implies that only half of the levels are physically independent. Of course, the results below take this issue into account.

With the above Nambu bi-spinor basis, the mean-field Hamiltonian has the 4 × 4 matrix representation

$$\mathcal{H}_{\mathrm{MF}} = \begin{pmatrix} \varepsilon_\uparrow & \Delta_d & \alpha_d & 0 \\ \Delta_d^* & -\varepsilon_\downarrow & 0 & \alpha_d \\ \alpha_d^* & 0 & \varepsilon_\downarrow & \Delta_d \\ 0 & \alpha_d^* & \Delta_d^* & -\varepsilon_\uparrow \end{pmatrix},$$
$$\varepsilon_\uparrow = \varepsilon_0 - B_z + U\langle n_\downarrow \rangle, \ \varepsilon_\downarrow = \varepsilon_0 + B_z + U\langle n_\uparrow \rangle,$$
$$\alpha_d = B_x + iB_y - U\left\langle d_\downarrow^\dagger d_\uparrow \right\rangle, \quad \Delta_d = U\langle d_\downarrow d_\uparrow \rangle. \quad (25)$$

The mean-field parameters appearing in Equation 25 follow by solving the self-consistency equations

$$\langle n_\uparrow \rangle = \frac{1}{\beta}\sum_\omega G_{d,11}(\omega), \quad \langle n_\downarrow \rangle = \frac{1}{\beta}\sum_\omega G_{d,33}(\omega),$$
$$\left\langle d_\downarrow^\dagger d_\uparrow \right\rangle = \frac{1}{\beta}\sum_\omega G_{d,13}(\omega), \ \langle d_\downarrow d_\uparrow \rangle = \frac{1}{\beta}\sum_\omega G_{d,21}(\omega), \quad (26)$$

where the mean-field approximation readily yields

$$G_d(\omega) = \left[i\omega - \mathcal{H}_{\mathrm{MF}} - \Sigma_{\mathrm{S}}(\omega) - \Sigma_{\mathrm{TS}}(\omega) \right]^{-1}. \quad (27)$$

The self-energies $\Sigma_{\mathrm{S/TS}}(\omega)$ due to the coupling of the QD to the S/TS leads have the matrix representation

$$\Sigma_{\mathrm{S}} = \Gamma_{\mathrm{S}} \begin{pmatrix} g_{11} & -g_{12} & 0 & 0 \\ -g_{21} & g_{22} & 0 & 0 \\ 0 & 0 & g_{11} & -g_{12} \\ 0 & 0 & -g_{21} & g_{22} \end{pmatrix} \quad (28)$$

and

$$\Sigma_{\mathrm{TS}} = \Gamma_{\mathrm{TS}} \begin{pmatrix} G_{11} & 0 & 0 & -G_{12}e^{i\phi} \\ 0 & 0 & 0 & 0 \\ 0 & 0 & 0 & 0 \\ -G_{21}e^{i\phi} & 0 & 0 & G_{22} \end{pmatrix} \quad (29)$$

with the hybridization parameters $\Gamma_{\mathrm{S/TS}} = \lambda_{\mathrm{S/TS}}^2$. The bGFs $g(\omega)$ and $G(\omega)$ have been defined in Equation 6 and Equation 7, respectively. Once a self-consistent solution to Equation 26 has been determined, which in general requires numerics, the Josephson current is obtained from Equation 5 as

$$I(\phi) = -\frac{e}{\hbar\beta}\sum_{\omega}\frac{\partial_\phi \det\left[G_d^{-1}(\omega)\right]}{\det\left[G_d^{-1}(\omega)\right]}. \tag{30}$$

In what follows, we study a setup with $\Delta_p = \Delta$ and consider the zero-temperature limit.

In order to compare our self-consistent mean-field results to the noninteracting case, let us briefly summarize analytical expressions for the $U = 0$ ABS spectrum in the atomic limit defined by $\Gamma_{S,TS} \ll \Delta$. First we notice that at low energy scales, the self-energy $\Sigma = \Sigma_S + \Sigma_{TS}$, see Equation 28 and Equation 29, simplifies to

$$\Sigma \simeq \begin{pmatrix} \frac{2\Delta}{i\omega}\Gamma_{TS} & -\Gamma_S & 0 & -\frac{2\Delta}{i\omega}\Gamma_{TS}e^{i\phi} \\ -\Gamma_S & 0 & 0 & 0 \\ 0 & 0 & 0 & -\Gamma_S \\ -\frac{2\Delta}{i\omega}\Gamma_{TS}e^{i\phi} & 0 & -\Gamma_S & \frac{2\Delta}{i\omega}\Gamma_{TS} \end{pmatrix} \tag{31}$$

The ABS spectrum of the S–QD–TS junction then follows by solving a determinantal equation, $\det\left[G_d^{-1}(\omega)\right] = 0$. One finds a zero-energy pole which is related to the MBS and results from the $1/\omega$ dependence of $\Sigma_{TS}(\omega)$. In addition, we get finite-energy subgap poles for

$$i\omega \equiv E_A^{(\sigma_1=\pm,\sigma_2=\pm)} = \sigma_1\sqrt{\frac{b_0 + \sigma_2\sqrt{b_0^2 + 4c_0}}{2}}, \tag{32}$$

with the notation

$$\begin{aligned} b_0 &= \varepsilon_\downarrow^2 + \varepsilon_\uparrow^2 + 4\Gamma_{TS}\Delta + 2\Gamma_S^2 + 2\left|\alpha_d\right|^2, \\ c_0 &= -4\Gamma_{TS}\Delta\left(\varepsilon_\downarrow^2 + \Gamma_S^2 + \left|\alpha_d\right|^2\right) - \varepsilon_\uparrow^2\varepsilon_\downarrow^2 \\ &\quad -\left(\left|\alpha_d\right|^2 - \Gamma_S^2\right)\left(\left|\alpha_d\right|^2 - \Gamma_S^2 - \varepsilon_\uparrow\omega_\downarrow\right) \\ &\quad +8\Delta\Gamma_S\Gamma_{TS}\,\mathrm{Re}\left(\alpha_d e^{i\phi}\right). \end{aligned} \tag{33}$$

In Figure 2, numerically exact results for the $U = 0$ ABS spectrum are compared to the analytical prediction (Equation 32). We first notice that, as expected, Equation 32 accurately fits the numerical results in the atomic limit, see the left panel in Figure 2. Deviations can be observed for larger values of $\Gamma_{S,TS}/\Delta$. However, as shown in the right panel of Figure 2, rather good agreement is again obtained by rescaling Equation 32 with a constant factor of the order of $(1 + \Gamma_{S,TS}/\Delta)$. For finite B_y, we find (data not shown) that the phase-dependent ABS spectrum is shifted with respect to $\phi = 0$. In fact, since the phase dependence of the subgap states comes from the term $\mathrm{Re}\left(\alpha_d e^{i\phi}\right)$ in the atomic limit, see Equation 25 and Equation 33, B_y can be fully accounted for in this limit by simply shifting $\phi \to \phi + \varphi_0$. We thereby recover the φ_0-junction behavior discussed before for the cotunneling regime, see Equation 23.

We next turn to self-consistent mean-field results for the phase-dependent ABS spectrum at finite U. Figure 3 shows the spectrum for the electron–hole symmetric case $\varepsilon_0 = -U/2$, with other parameters as in the right panel of Figure 2. For moderate interaction strength, e.g., taking $U = \Delta$ (left panel), we find that com-

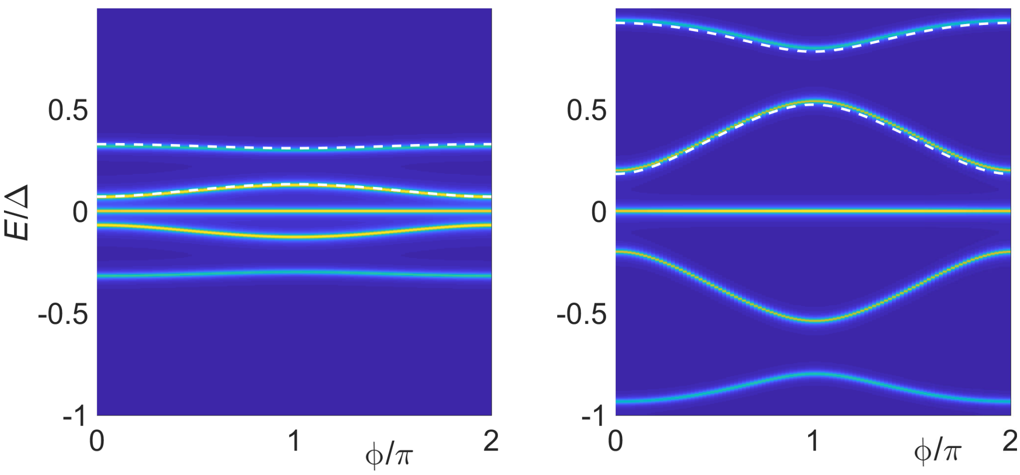

Figure 2: Phase dependence of the subgap spectrum of an S–QD–TS junction in the noninteracting case, $U = 0$. The TS wire is modeled from the low-energy limit of a Kitaev chain, and we use the parameters $B_y = 0$, $B_x = B_z = B/\sqrt{2}$, $\varepsilon_0 = 0$, $\Delta_p = \Delta$, and $\Gamma_S = \Gamma_{TS} = \Gamma$. From blue to yellow, the color code indicates increasing values of the spectral density. The left (right) panel is for $\Gamma = 0.045\Delta$ and $B = 0.1\Delta$ ($\Gamma = B = 0.5\Delta$). Solid curves were obtained by numerical evaluation of Equation 30. Dashed curves give the analytical prediction (Equation 32). In the right panel, the energies resulting from Equation 32 have been rescaled by the factor $1 + \Gamma/\Delta$.

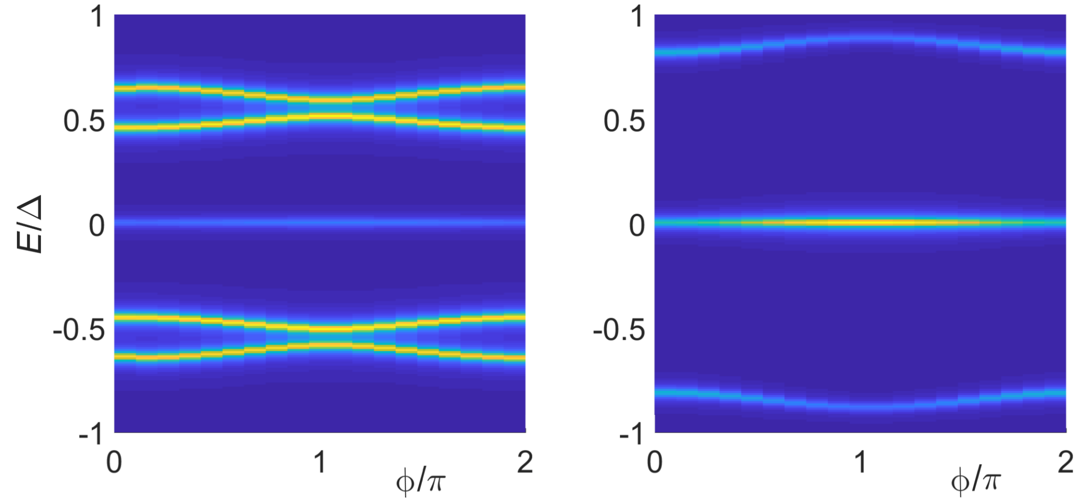

Figure 3: Phase-dependent ABS spectrum from mean-field theory for S–QD–TS junctions as in Figure 2 but with $U > 0$ and $\varepsilon_0 = -U/2$. We put $\Delta_p = \Delta$, $B_y = 0$, and $\Gamma_S = \Gamma_{TS} = \Gamma$. The color code is as in Figure 2. The left panel is for $U = \Delta$, $\Gamma = 0.5\Delta$, and $B_x = B_z = B/\sqrt{2}$ with $B = 0.5\Delta$ [cf. the right panel of Figure 2]. The right panel is for $U = 10\Delta$, $\Gamma = 4.5\Delta$, $B_x = 15\Delta$, and $B_z = 0$.

pared to the $U = 0$ case in Figure 2, interactions push together pairs of Andreev bands, e.g., the pair corresponding to $E_A^{(+,\pm)}$ in Equation 30. On the other hand, for stronger interactions, e.g., $U = 10\Delta$ (right panel), the outer ABSs leak into the continuum spectrum and only the inner Andreev states remain inside the superconducting gap. The ABS spectrum shown in Figure 3 is similar to what is observed in mean-field calculations for S–QD–S systems with broken spin symmetry and in the magnetic regime of the QD, where one finds up to four ABSs for $U < \Delta$ while the outer ABSs merge with the continuum for $U > \Delta$ [79]. Interestingly, the inner ABS contribution to the free energy for $U = 10\Delta$ is minimal for $\phi = \pi$, see right panel of Figure 3, and we therefore expect π-junction behavior for $B_y = 0$ also in the regime with $U \gg \Delta$ and $B \gg \Delta$. We notice, however, that changing the sign of B_x would result in zero junction behavior. We interpret the inner ABSs for $U \gg \Delta$ as Shiba states with the phase dependence generated by the coupling to the MBS. Without the latter coupling, the Shiba state has ϕ-independent energy slightly below Δ determined by the scattering phase shift difference between both spin polarizations [80].

As illustrated in Figure 4, the CPR computed numerically from Equation 30 for different values of $\Gamma_{S,TS}/\Delta$, where B_x has been inverted with respect to its value in Figure 3, results in zero junction behavior. This behavior is expected from Equation 23 in the cotunneling regime, and Figure 4 shows that it also persists for $\Gamma_{S,TS} \gg \Delta$. In contrast to Equation 23, however, the CPR for $\Gamma_{S,TS} \gg \Delta$ differs from a purely sinusoidal behavior, see Figure 4. Moreover, for $B_y \neq 0$, we again encounter φ_0-junction behavior, cf. the inset of Figure 4, in accordance with the perturbative result in Equation 23. Our mean-field results suggest that φ_0-junction behavior is very robust and extends also into other parameter regimes as long as the condition $B_y \neq 0$ is met.

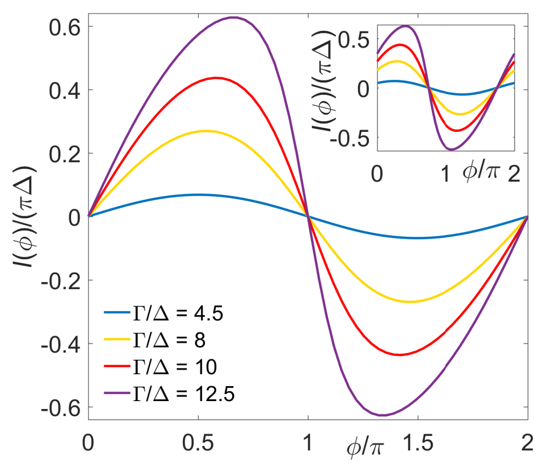

Figure 4: Main panel: Mean-field results for the CPR of S–QD–TS junctions with different Γ/Δ values, where we assume $\Delta_p = \Delta$, $U = 10\Delta$, $\varepsilon_0 = -U/2$, $\Gamma_S = \Gamma_{TS} = \Gamma$, $B = 15\Delta$, and $B_z = 0$. Main panel: For $B_x = -B$ and $B_y = 0$. Inset: Same but for $B_y = -B_x = B/\sqrt{2}$, where φ_0-junction behavior occurs.

Next, Figure 5 shows mean-field results for the critical current, $I_c = \max_\phi |I(\phi)|$, as function of the local magnetic field B_x and otherwise the same parameters as in Figure 4. The main panel in Figure 5 shows that I_c increases linearly with B_x for small $B_x < \Delta$, then exhibits a maximum around $B_x \approx \Gamma$, and subsequently decreases again to small values for $B_x \gg \max\{\Gamma_{S,TS},\Delta\}$. On the other hand, for a fixed absolute value B of the magnetic field and $B_y = 0$, the critical current also exhibits a maximum as a function of the angle θ_B between **B** and the MBS spin polarization axis ($\hat{e}_z$). This effect is illustrated in the inset of Figure 5. As expected, the Josephson current vanishes for $\theta_B \to 0$, where the supercurrent blockade argument of [31] implies $I_c = 0$, and reaches its maximal value for $\theta_B = \pi/2$.

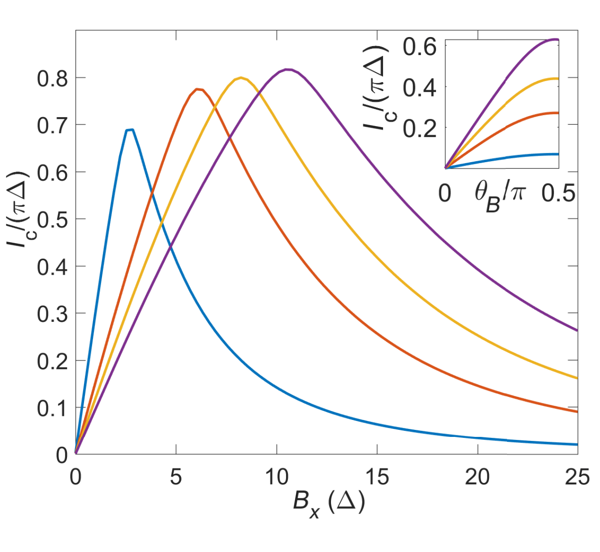

Figure 5: Main panel: Mean-field results for the critical current I_c vs local magnetic field scale B_x in S–QD–TS junctions. Parameters are as in the main panel of Figure 4, i.e., $U = 10\Delta$, $\epsilon_0 = -U/2$, and $B_{y,z} = 0$. From left to right, different curves are for $\Gamma/\Delta = 4.5$, 8, 10 and 12.5. Inset: I_c vs angle θ_B, where $\mathbf{B} = B\,(\sin\theta_B, 0, \cos\theta_B)$ with $B = 15\Delta$.

Spinful nanowire model for the TS

Model

Before turning to the S–TS–S setup in Figure 1b, we address the question of how the above results for S–QD–TS junctions change when using the spinful nanowire model of [2,3] instead of the low-energy limit of a Kitaev chain, see Equation 7. In fact, we will first describe the Josephson current for the elementary case of an S–TS junction using the spinful nanowire model. Surprisingly, to the best of our knowledge, this case has not yet been addressed in the literature.

In spatially discretized form, the spinful nanowire model for TS wires reads [2,3,43]

$$
\begin{aligned}
H_{\mathrm{TS}} &= \frac{1}{2}\sum_j \left[\Psi_j^\dagger \hat{h} \Psi_j + \left(\Psi_j^\dagger \hat{t} \Psi_{j+1} + \mathrm{h.c.} \right) \right], \\
\hat{h} &= (2t-\mu)\tau_z\sigma_0 + V_x \tau_0\sigma_x + \Delta_p \tau_x \sigma_0 , \\
\hat{t} &= -t\tau_z\sigma_0 + i\alpha\tau_z\sigma_z ,
\end{aligned}
\qquad (34)
$$

where the lattice fermion operators $c_{j\sigma}$ for given site j with spin polarizations $\sigma = \uparrow,\downarrow$ are combined to the four-spinor operator

$$\Psi_j = \left(c_{j\uparrow}, c_{j\downarrow}, c_{j\downarrow}^\dagger, -c_{j\uparrow}^\dagger \right)^T .$$

The Pauli matrices $\tau_{x,y,z}$ (and unity τ_0) again act in Nambu space, while Pauli matrices $\sigma_{x,y,z}$ and σ_0 refer to spin. In the figures shown below, we choose the model parameters in Equation 34 as discussed in [43]. The lattice spacing is set to $a = 10$ nm, which results in a nearest-neighbor hopping $t = \hbar^2/(2m^*a^2) = 20$ meV and the spin–orbit coupling strength $\alpha = 4$ meV for InAs nanowires. The proximity-induced pairing gap is again denoted by Δ_p, the chemical potential is μ, and the bulk Zeeman energy scale V_x is determined by a magnetic field applied along the wire. Under the condition

$$V_x > V_x^c = \sqrt{\mu^2 + \Delta_p^2}, \qquad (35)$$

the topologically nontrivial phase is realized [2,3]. As we discuss below, the physics of the S–QD–TS junction sensitively depends on both the bulk Zeeman field V_x and on the local magnetic field **B** acting on the QD, where one can either identify both magnetic fields or treat **B** as independent field. In any case, the bGF $\tilde{G}(\omega)$ for the model in Equation 34, which now replaces the Kitaev chain result $G(\omega)$ in Equation 7, needs to be computed numerically. The bGF $\tilde{G}$ has been described in detail in [43], where also a straightforward numerical scheme for calculating $\tilde{G}(\omega)$ has been devised. With the replacement $G \to \tilde{G}$, we can then take over the expressions for the Josephson current discussed before. Below we study these expressions in the zero-temperature limit.

S–TS junction

Let us first address the CPR for the S–TS junction case. The Josephson current can be computed using the bGF expression for tunnel junctions in [40], which is a simplified version of the above expressions for the S–QD–TS case. The spin-conserving tunnel coupling λ defines a transmission probability (transparency) $\mathcal{T}$ of the normal junction [40,43]. Close to the topological transition, the transparency is well approximated by

$$\mathcal{T} = \frac{4(\lambda/t)^2}{\left[1+(\lambda/t)^2\right]^2}, \qquad (36)$$

where t = 20 meV is the hopping parameter in Equation 34. We then study the CPR and the resulting critical current I_c as a function of $\mathcal{T}$ for both the topologically trivial ($V_x < V_x^c$) and the nontrivial ($V_x > V_x^c$) regime, see Equation 35.

In Figure 6, we show the V_x dependence of the critical current I_c for the symmetric case $\Delta = \Delta_p$. In particular, it is of interest to determine how I_c changes as one moves through the phase transition in Equation 35. First, we observe that I_c is strongly suppressed in the topological phase in comparison to the topologically trivial phase. In fact, I_c slowly decreases as one moves into the deep topological phase by increasing V_x. This observation is in accordance with the expected supercurrent blockade in the deep topological limit [31]: $I_c = 0$ for the corresponding Kitaev chain case since p-wave pairing correlations on the TS side are incompatible with s-wave correlations on the S side. However, a residual finite supercurrent can be observed even for rather large values of V_x. We attribute this effect to the remaining s-wave pairing correlations contained in the spinful nanowire model (Equation 34). Second, Figure 6 shows kink-like features in the $I_c(V_x)$ curve near the topological transition, $V_x \approx V_x^c$. The inset of Figure 6 demonstrates that this feature comes from a rapid decrease of the ABS contribution while the continuum contribution remains smooth. This observation suggests that continuum contributions in this setup mainly originate from s-wave pairing correlations which are not particularly sensitive to the topological transition.

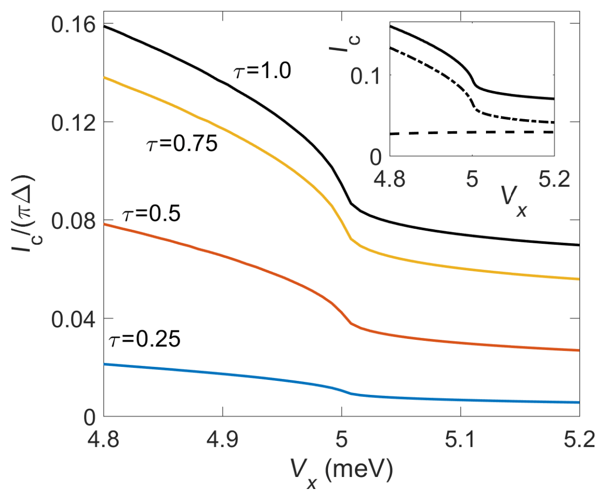

Figure 6: Main panel: Critical current I_c vs Zeeman energy V_x for an S–TS junction using the spinful TS nanowire model (Equation 34) for $\Delta_p = \Delta$ = 0.2 meV, μ = 5 meV, and different transparencies $\mathcal{T}$ calculated from Equation 36. All other parameters are specified in the main text. Inset: Decomposition of I_c for $\mathcal{T}$ = 1 into ABS (dotted-dashed) and continuum (dashed) contributions.

In Figure 7, we show the CPR for the S–TS junction with $\mathcal{T}$ = 1 in Figure 6, where different curves correspond to different Zeeman couplings V_x near the critical value. We find that in many parameter regions, in particular for $\mathcal{T} < 1$, the CPR is to high accuracy given by a conventional 2π-periodic Josephson relation, $I(\phi) = I_c \sin\phi$. In the topologically trivial phase, small deviations from the sinusoidal law can be detected, but once one enters the topological phase, these deviations become extremely small.

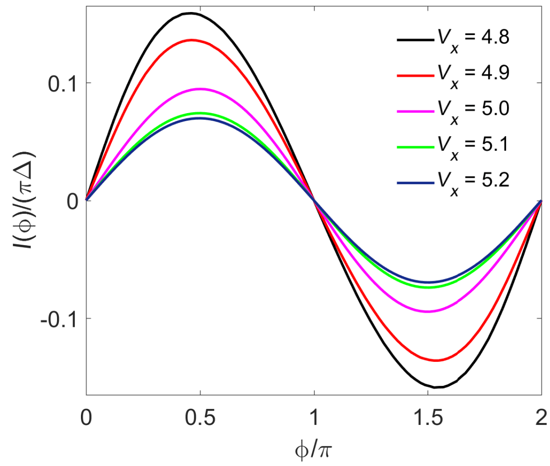

Figure 7: CPR for the S–TS junction with $\mathcal{T}$ = 1 in Figure 6, for different bulk Zeeman fields V_x (in meV) near the critical value V_x^c = 5.004 meV.

S–QD–TS junction with spinful TS wire: Mean-field theory

Apart from providing a direct link to experimental control parameters, another advantage of using the spinful nanowire model of [2,3] for modeling the TS wire is that the angle between the local Zeeman field **B** and the MBS spin polarization does not have to be introduced as phenomenological parameter but instead results from the calculation [43]. It is thus interesting to study the Josephson current in S–QD–TS junctions where the TS wire is described by the spinful nanowire model. For this purpose, we now revisit the mean-field scheme for S–QD–TS junctions using the bGF $\tilde{G}(\omega)$ for the spinful nanowire model (Equation 34). In particular, with the replacement $G \to \tilde{G}$, we solve the self-consistency equations (Equation 26) and thereby obtain the mean-field parameters in Equation 25. The resulting QD GF, $G_d(\omega)$ in Equation 27, then determines the Josephson current in Equation 30. Below we present self-consistent mean-field results obtained from this scheme. In view of the huge parameter space of this problem, we here only discuss a few key observations. A full discussion of the phase diagram and the corresponding physics will be given elsewhere.

The main panel of Figure 8 shows the critical current I_c vs the bulk Zeeman energy V_x for several values of the chemical potential μ, where the respective critical value V_x^c in

Equation 35 for the topological phase transition also changes with μ. The results in Figure 8 assume that the local magnetic field **B** acting on the QD coincides with the bulk Zeeman field V_x in the TS wire, i.e., $\mathbf{B} = (V_x,0,0)$. For the rather large values of $\Gamma_{S,TS}$ taken in Figure 8, the I_c vs V_x curves again exhibit a kink-like feature near the topological transition, $V_x \approx V_x^c$. This behavior is very similar to what happens in S–TS junctions with large transparency $\mathcal{T}$, cf. Figure 6. As demonstrated in the inset of Figure 8, the physical reason for the kink feature can be traced back to a sudden drop of the ABS contribution to I_c when entering the topological phase $V_x > V_x^c$. In the latter phase, I_c becomes strongly suppressed in close analogy to the S–TS junction case shown in Figure 6.

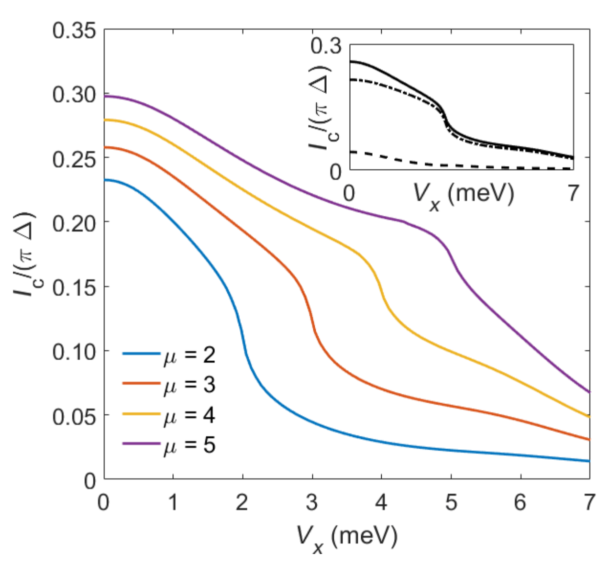

Figure 8: Main panel: Critical current I_c vs Zeeman energy V_x for S–QD–TS junctions from mean-field theory using the spinful TS nanowire model (Equation 34). Results are shown for several values of the chemical potential μ (in meV), where we assume $U = 10\Delta$, $\varepsilon_0 = -U/2$, $\Delta_p = \Delta = 0.2$ meV, $\Gamma_S = 2\Gamma_{TS} = 9\Delta$, and $\mathbf{B} = (V_x,0,0)$. Inset: Detailed view of the transition region $V_x \approx V_x^c$ for μ = 4 meV, including a decomposition of I_c into the ABS (dotted-dashed) and the continuum (dashed) contribution.

In Figure 8, both the QD and the TS wire were subject to the same magnetic Zeeman field. If the direction and/or the size of the local magnetic field **B** applied to the QD can be varied independently from the bulk magnetic field $V_x\hat{e}_x$ applied to the TS wire, one can arrive at rather different conclusions. To illustrate this statement, Figure 9 shows the I_c vs B_z dependence for $\mathbf{B} = (0,0,B_z)$ perpendicular to the bulk field, with $V_x > V_x^c$ such that the TS wire is in the topological phase. In this case, Figure 9 shows that I_c exhibits a maximum close to $B_z \sim \Gamma$. This behavior is reminiscent of what we observed above in Figure 5, using the low-energy limit of a Kitaev chain for the bGF of the TS wire. Remarkably, the critical current can here reach values close to the unitary limit, $I_c \sim e\Delta/\hbar$. We note that since B_z does not drive a phase transition, no kink-like features appear for the $I_c(B_z)$ curves shown in Figure 9. Finally, the inset of Figure 9 shows that for **B** perpendicular to $V_x\hat{e}_x$, where $V_x > V_x^c$ for the parameters chosen in Figure 9, the ABSs provide the dominant contribution to the current in this regime.

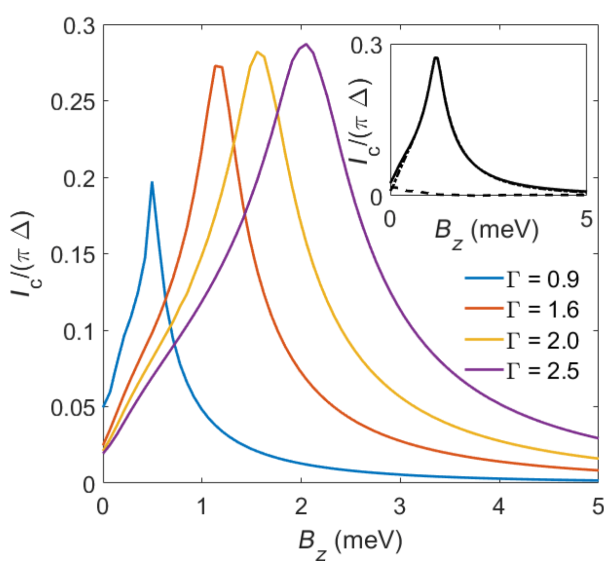

Figure 9: Main panel: Mean-field results for I_c vs B_z in S–QD–TS junctions for several values of $\Gamma_S = \Gamma_{TS} = \Gamma$ (in meV) and μ = 4 meV. The bulk Zeeman field $V_x = 5$ meV along $\hat{e}_x$ (where $V_x > V_x^c$ for our parameters) is applied to the spinful TS wire, while the QD is subject to the local magnetic field $\mathbf{B} = B_z\hat{e}_z$. All other parameters are as in Figure 8. Inset: Decomposition of I_c into ABS (dotted-dashed) and continuum (dashed) contributions for Γ = 1.6 meV.

S–TS–S junctions: Switching the parity of a superconducting atomic contact

Model

We now proceed to the three-terminal S–TS–S setup shown in Figure 1b. The CPR found in the related TS–S–TS trijunction case has been discussed in detail in [43], see also [44]. Among other findings, a main conclusion of [43] for the TS–S–TS geometry was that the CPR can reveal information about the spin canting angle between the MBS spin polarization axes in both TS wires. In what follows, we study the superficially similar yet rather different case of an S–TS–S junction. Throughout this section, we model the TS wire via the low-energy theory of a spinless Kitaev chain, where the bGF $G(\omega)$ in Equation 7 applies.

One can view the setup in Figure 1b as a conventional superconducting atomic contact (SAC) with a TS wire tunnel-coupled to the S–S junction. Over the past few years, impressive experimental progress [52-54] has demonstrated that the ABS level system in a SAC [81] can be accurately probed and manipulated by coherent or incoherent microwave spectroscopy techniques. We show below that an additional TS wire, cf. Figure 1b, acts as tunable parity switch on the many-body ABS levels of the SAC. As we have discussed above, the supercurrent flowing directly between a given S lead and the TS wire is expected to be strongly suppressed. However, through the hybridization with the MBS, Andreev level configurations with even and odd fermion parity are connected. This effect has profound and potentially useful consequences for Andreev spectroscopy.

An alternative view of the setup in Figure 1b is to imagine an S–TS junction, where S1 plays the role of the S lead and the spinful TS wire is effectively composed from a spinless (Kitaev) TS wire and the S2 superconductor. The *p*- and *s*-wave pairing correlations in the spinful TS wire are thereby spatially separated. Since the *s*- and *p*-wave bands represent normal modes, they are not directly coupled to each other in this scenario, i.e., we have to put $\lambda_2 = 0$. We discuss this analogy in more detail later on.

We consider a conventional single-channel SAC (gap Δ) coupled via a point contact to a TS wire (gap Δ_p), cf. Figure 1b. The superconducting phase difference across the SAC is denoted by $\phi = \phi_1 - \phi_2$, where ϕ_j is the phase difference between the respective S arm (j = 1,2) and the TS wire. In practice, the SAC can be embedded into a superconducting ring for magnetic flux tuning of ϕ. To allow for analytical progress, we here assume that Δ_p is so large that continuum quasiparticle excitations in the TS wire can be neglected. In that case, only the MBS at the junction has to be kept when modeling the TS wire. However, we will also hint at how one can treat the general case.

For the two S leads, boundary fermion fields are contained in Nambu spinors as in Equation 6,

$$\Psi_{\mathrm{S},j=1,2} = \begin{pmatrix} \Psi_{j,\uparrow} \\ \Psi^{\dagger}_{j,\downarrow} \end{pmatrix}, \tag{37}$$

where their bGF follows with the Nambu matrix $g(\omega)$ in Equation 6 as

$$g_j^{-1}(\omega) = g^{-1}(\omega) + b_j \tau_0 \,. \tag{38}$$

We again use Pauli matrices $\tau_{x,y,z}$ and unity τ_0 in Nambu space. The dimensionless parameters $b_{1,2}$ describe the Zeeman field component along the MBS spin polarization axis, see below. Since above-gap quasiparticles in the TS wire are neglected here, the TS wire is represented by the Majorana operator $\gamma = \gamma^{\dagger}$, with $\gamma^2 = 1/2$, which anticommutes with all other fermions. We may represent γ by an auxiliary fermion $f_{\uparrow}$, where the index reminds us that the MBS spin polarization points along $\hat{e}_z$,

$$\gamma = \left(f_{\uparrow} + f_{\uparrow}^{\dagger}\right)\big/\sqrt{2}\,. \tag{39}$$

The other Majorana mode $\gamma' = -i\left(f_{\uparrow} - f_{\uparrow}^{\dagger}\right)\big/\sqrt{2}$, which is localized at the opposite end of the TS wire, is assumed to have negligible hybridization with the $\Psi_{\mathrm{S},j}$ spinors and with γ. Writing the Euclidean action as $S = S_0 + S_{\mathrm{tun}}$, we have an uncoupled action contribution,

$$\begin{aligned} S_0 = {} & \sum_{j=1,2} \int_0^{\beta} \mathrm{d}\tau \mathrm{d}\tau' \bar{\Psi}_{\mathrm{S},j}(\tau) g_j^{-1}(\tau-\tau') \Psi_{\mathrm{S},j}(\tau') \\ & + \frac{1}{2}\int_0^{\beta} \mathrm{d}\tau\, \gamma(\tau) \partial_{\tau} \gamma(\tau)\,. \end{aligned} \tag{40}$$

The leads are connected by a time-local tunnel action corresponding to the tunnel Hamiltonian

$$\begin{aligned} H_{\mathrm{tun}} = {} & t_0 \left(\Psi^{\dagger}_{\mathrm{S},1} \tau_z e^{i\tau_z \phi/2} \Psi_{\mathrm{S},2} + \mathrm{h.c.}\right) \\ & + \sum_{j=1,2} \frac{\lambda_j}{\sqrt{2}} \left(\Psi^{\dagger}_{j,\uparrow} e^{i\phi_j/2} - \mathrm{h.c.}\right)\gamma. \end{aligned} \tag{41}$$

Without loss of generality, we assume that the tunnel amplitudes t_0 and $\lambda_{1,2}$, see Figure 1b, are real-valued and that they include density-of-state factors again. The parameter t_0 (with $0 \le t_0 \le 1$) determines the transparency $\mathcal{T}$ of the SAC in the normal-conducting state [36], cf. Equation 36,

$$\mathcal{T} = \frac{4t_0^2}{\left(1+t_0^2\right)^2}. \tag{42}$$

Note that in Equation 41 we have again assumed spin-conserving tunneling, where only spin-↑ fermions in the SAC are tunnel-coupled to the Majorana fermion γ, cf. Equation 4.

At this stage, it is convenient to trace out the $\Psi_{\mathrm{S},2}$ spinor field. As a result, the SAC is described in terms of only one spinor field, $\Psi \equiv \Psi_{\mathrm{S},1}$, which however is still coupled to the Majorana field γ. After some algebra, we obtain the effective action

$$S_{\text{eff}}=\int_0^\beta d\tau d\tau'\left\{\begin{array}{l}\bar{\Psi}(\tau)K^{-1}(\tau-\tau')\Psi(\tau')\\ +\Phi^T(\tau)\begin{bmatrix}\frac{1}{2}\delta(\tau-\tau')\partial_{\tau'}\\ -\lambda_2^2P_{\downarrow}g_2(\tau-\tau')P_{\uparrow}\end{bmatrix}\Phi(\tau')\\ +\left[\begin{array}{l}\bar{\Psi}(\tau)\begin{pmatrix}\lambda_1e^{i\phi_1/2}\delta(\tau-\tau')\\ -\lambda_2e^{i\phi_2/2}t_0\tau_ze^{i\tau_z\phi/2}g_2(\tau-\tau')\end{pmatrix}\\ P_{\uparrow}\Phi(\tau')+\text{h.c.}\end{array}\right]\end{array}\right\}, \quad (43)$$

where the operator $P_\uparrow = (\tau_0 + \tau_z)/2$ projects a Nambu spinor to its spin-↑ component. Moreover, we have defined an effective GF in Nambu space with frequency components

$$K^{-1}(\omega)=g_1^{-1}(\omega)-t_0^2\tau_ze^{i\tau_z\phi/2}g_2(\omega)e^{-i\tau_z\phi/2}\tau_z\,, \quad (44)$$

and the TS lead has been represented by the Majorana–Nambu spinor

$$\Phi(\tau)=\frac{1}{\sqrt{2}}\begin{pmatrix}1\\1\end{pmatrix}\gamma(\tau)=\tau_x\Phi^*(\tau). \quad (45)$$

We note in passing that Equation 43 could at this point be generalized to include continuum states in the TS wire. To that end, one has to (i) replace $\Phi \to (\psi, \psi^\dagger)^T$, where ψ is the boundary fermion of the effectively spinless TS wire, and (ii) replace $\delta(\tau-\tau')\partial_{\tau'} \to G^{-1}(\tau-\tau')$ with G in Equation 7. Including bulk TS quasiparticles becomes necessary for small values of the proximity gap, $\Delta_p \ll \Delta$, and/or when studying nonequilibrium applications within a Keldysh version of our formalism.

In any case, after neglecting the above-gap TS continuum quasiparticles, the partition function follows with S_{eff} in Equation 43 in the functional integral representation

$$Z=\int\mathcal{D}\left[\bar{\Psi},\Psi,\gamma\right]e^{-S_{\text{eff}}}\equiv e^{-\beta F(\phi_1,\phi_2)}. \quad (46)$$

As before, the Josephson current through S lead no. j then follows from the free energy via

$$I_j=(2e/\hbar)\partial_{\phi_j}F.$$

The supercurrent flowing through the TS wire is then given by

$$I_{\text{TS}}=-(I_1+I_2), \quad (47)$$

as dictated by current conservation.

Atomic limit

In order to get insight into the basic physics, we now analyze in detail the atomic limit, where Δ represents the largest energy scale of interest and hence the dynamics is confined to the subgap region. In this case, we can approximate $\sqrt{\Delta^2+\omega^2}\approx\Delta$. After the rescaling

$$\Psi\to\sqrt{\Delta/(1+t_0^2)}\Psi$$

in Equation 43, we arrive at an effective action, $S_{\text{eff}} \to S_{\text{at}}$, valid in the atomic limit,

$$S_{\text{at}}=\int_0^\beta d\tau\left\{\begin{array}{l}\frac{1}{2}\gamma\partial_\tau\gamma+\bar{\Psi}\begin{bmatrix}\partial_\tau+\Delta\cos(\phi/2)\tau_x\\ +r\Delta\sin(\phi/2)\tau_y+B_z\tau_0\end{bmatrix}\Psi\\ +\frac{1}{\sqrt{2}}\sum_{\sigma=\uparrow,\downarrow}\left(\lambda_\sigma\Psi_\sigma^\dagger-\text{h.c.}\right)\gamma\end{array}\right\}, \quad (48)$$

where $r=\sqrt{1-T}$ is the reflection amplitude of the SAC, see Equation 42. We recall that $\Psi=\left(\psi_\uparrow,\psi_\downarrow^\dagger\right)^T$, see Equation 37. Moreover, we define the auxiliary parameters

$$\begin{aligned}\lambda_\uparrow&=\lambda_1\sqrt{(1+r)\Delta/2}e^{i\phi_1/2},\\ \lambda_\downarrow&=-\lambda_2\sqrt{(1-r)\Delta/2}e^{-i\phi_2/2},\\ B_z&=\left(\frac{1+r}{2}b_1+\frac{1-r}{2}b_2\right)\Delta.\end{aligned} \quad (49)$$

The parameters $b_{1,2}$ in Equation 38 thus effectively generate the Zeeman scale B_z in Equation 49.

As a consequence of the atomic limit approximation, the action S_{at} in Equation 48 is equivalently expressed in terms of the effective Hamiltonian

$$\begin{aligned}H_{\text{at}}=&\sum_{\sigma=\uparrow,\downarrow=\pm}\sigma B_z\Psi_\sigma^\dagger\Psi_\sigma+\left(\delta_A\Psi_\uparrow^\dagger\Psi_\downarrow^\dagger+\text{h.c.}\right)\\ &+\frac{1}{\sqrt{2}}\sum_\sigma\left(\lambda_\sigma\Psi_\sigma^\dagger-\text{h.c.}\right)\gamma\,,\end{aligned} \quad (50)$$

where we define

$$\delta_A(\phi)=\Delta\left[\cos(\phi/2)-ir\sin(\phi/2)\right]. \quad (51)$$

For a SAC decoupled from the TS wire and taken at zero field ($B_z = 0$), the ABS energy follows from Equation 50 in the standard form [62]

$$E_A(\phi) = |\delta_A| = \Delta\sqrt{1-\mathcal{T}\sin^2(\phi/2)}. \qquad (52)$$

We emphasize that H_{at} neglects TS continuum quasiparticles as well as all types of quasiparticle poisoning processes. Let us briefly pause in order to make two remarks. First, we note that the Majorana field

$$\gamma = \left(f_\uparrow + f_\uparrow^\dagger\right)/\sqrt{2},$$

see Equation 39, couples to both spin modes ψ_σ in Equation 50. The coupling $\lambda_\downarrow$ between γ and the spin-$\downarrow$ field in the SAC, $\psi_\downarrow$, is generated by crossed Andreev reflection processes, where a Cooper pair in lead S2 splits according to $\psi_{2,\uparrow}^\dagger\psi_{2,\downarrow}^\dagger \to f_\uparrow^\dagger\psi_{1,\downarrow}^\dagger$, plus the conjugate process. Second, we observe that H_{at} is invariant under a particle–hole transformation, amounting to the replacements $\psi_\sigma \to \psi_\sigma^\dagger$ and $f_\uparrow \to f_\uparrow^\dagger$, along with $B_z \to -B_z$ and $\phi_j \to 2\pi - \phi_j$.

We next notice that with $n_\sigma = \psi_\sigma^\dagger\psi_\sigma = 0,1$ and $n_f = f_\uparrow^\dagger f_\uparrow = 0,1$, the total fermion parity of the junction,

$$\mathcal{P}_{\text{tot}} = (-1)^{n_f+n_\uparrow+n_\downarrow} = \pm 1, \qquad (53)$$

is a conserved quantity, $[\mathcal{P}_{\text{tot}}, H_{\text{at}}]_- = 0$. Below we restrict our analysis to the even-parity sector $\mathcal{P}_{\text{tot}} = +1$, but analogous results hold for the odd-parity case. The corresponding Hilbert subspace is spanned by four states,

$$|n_\uparrow, n_\downarrow, n_f\rangle = \left(\Psi_\uparrow^\dagger\right)^{n_\uparrow}\left(\Psi_\downarrow^\dagger\right)^{n_\downarrow}\left(f_\uparrow^\dagger\right)^{n_f}|0\rangle, \qquad (54)$$

where $(n_\uparrow, n_\downarrow, n_f) \in \{(0,0,0), (1,1,0), (1,0,1), (0,1,1)\}$ and $|0\rangle$ is the vacuum state. In this basis, the Hamiltonian (Equation 50) has the matrix representation

$$\mathcal{H}_{\text{at}}(\phi_1,\phi_2) = \begin{pmatrix} 0 & \delta_A^* & \lambda_\uparrow^*/2 & \lambda_\downarrow^*/2 \\ \delta_A & 0 & \lambda_\downarrow/2 & -\lambda_\uparrow/2 \\ \lambda_\uparrow/2 & \lambda_\downarrow^*/2 & B_z & 0 \\ \lambda_\downarrow/2 & -\lambda_\uparrow^*/2 & 0 & -B_z \end{pmatrix}. \qquad (55)$$

The even-parity ground state energy, $E_G^{(e)} = \min(\varepsilon)$, follows as the smallest root of the quartic equation

$$\det\left(\mathcal{H}_{\text{at}} - \varepsilon\right) = 0. \qquad (56)$$

In order to obtain simple results, let us now consider the special case $\lambda_2 = 0$, where the TS wire is directly coupled to lead S1 only, see Figure 1b. In that case, we also have $\lambda_\downarrow = 0$, see Equation 49, and Equation 56 implies the four eigenenergies $\pm\varepsilon_\pm$ with

$$\varepsilon_\pm = \frac{1}{\sqrt{2}}\left(\begin{array}{c} E_A^2 + B_z^2 + \frac{1}{2}|\lambda_\uparrow|^2 \\ \pm\sqrt{\left(E_A^2 - B_z^2\right) + |\lambda_\uparrow|^2\left(E_A^2 + B_z^2\right)} \end{array}\right)^{1/2}, \qquad (57)$$

with $|\lambda_\uparrow|^2 = \lambda_1^2(1+r)\Delta/2$, see Equation 49. The ground-state energy is thus given by $E_G^{(e)} = -\varepsilon_+$. Since E_G depends on the phases $\phi_{1,2}$ only via the Andreev level energy $E_A(\phi)$ in Equation 52, the Josephson current through the SAC is given by

$$I_1 = -I_2 = \frac{2e}{\hbar}\partial_\phi E_G^{(e)} = -\frac{2e}{\hbar}\partial_\phi\varepsilon_+. \qquad (58)$$

Note that Equation 47 then implies that no supercurrent flows into the TS wire.

Next we observe that in the absence of the TS probe ($\lambda_1 = 0$), the even and odd fermion parity sectors of the SAC, $\mathcal{P}_{\text{SAC}} = (-1)^{n_\uparrow+n_\downarrow} = \pm 1$, are decoupled, see Equation 55, and Equation 57 yields $E_G^{(e)} = -\max(E_A, |B_z|)$. Importantly, the Josephson current is therefore fully blocked if the ground state is in the $\mathcal{P}_{\text{SAC}} = -1$ sector, i.e., for $|B_z| > E_A(\phi)$. For $\lambda_1 \neq 0$, however, $\mathcal{P}_{\text{SAC}}$ is not conserved anymore. This implies that the MBS can act as parity switch between the two Andreev sectors with parity $\mathcal{P}_{\text{SAC}} = \pm 1$. Near the level crossing point at $E_A \approx |B_z|$, i.e., assuming $\left|E_A^2 - B_z^2\right| \ll |\lambda_\uparrow|^2 \ll E_A^2 + B_z^2$, we obtain

$$\varepsilon_\pm \simeq \frac{1}{\sqrt{2}}\left(E_A^2 + B_z^2 \pm \lambda_1\sqrt{2(1+r)\Delta\left(E_A^2 + B_z^2\right)}\right)^{1/2}, \qquad (59)$$

which implies a nonvanishing supercurrent through the SAC even in the field-dominated regime, $|B_z| > E_A$. The MBS therefore acts as a parity switch and leaves a trace in the CPR by lifting the supercurrent blockade.

Another interpretation

Interestingly, for $\lambda_2 = \phi_2 = 0$, the S–TS–S setup in Figure 1b could also be viewed as a toy model for an S–TS junction, where the TS part corresponds to a spinful model. In that analogy, the Nambu spinor $\Psi_{S,1}$ stands for the S lead while the spinful TS wire is represented by (i) the Nambu spinor $\Psi_{S,2}$ which is responsible for the residual *s*-wave pairing correlations, and (ii) by the MF γ (or, more generally, by the Kitaev-chain spinless boundary fermion ψ) which encodes *p*-wave pairing correlations. Moreover, t_0 and λ_1 should now be understood as spin-conserving phenomenological tunnel couplings acting in the *s–s* and *s–p* wave channels, respectively. The phase difference across this effective S–TS junction is $\phi = \phi_1$ and the net S–TS tunnel coupling is given by $\lambda = \sqrt{t_0^2 + \lambda_1^2}$. Putting $\lambda_1 = 0$ in the topologically trivial phase of the TS wire, the Josephson current carried by Andreev states in the *s–s* channel is blocked when the ground state is in the odd parity sector of the SAC. For $\lambda_1 \neq 0$, the MBS-mediated switching between odd and even parity sectors will now be activated and thereby lift the supercurrent blockade.

Conventional midgap level

A similar behavior as predicted above for the MBS-induced parity switch between $\mathcal{P}_{\mathrm{SAC}} = \pm 1$ sectors could also be expected from a conventional fermionic subgap state tunnel-coupled to the SAC. Such a subgap state may be represented, e.g., by a single-level quantum dot in the Coulomb blockade regime. In particular, for a midgap (zero-energy) level with the fermion operator d, the Hamiltonian H_{at} in Equation 50 has to be replaced with

$$\tilde{H}_{\mathrm{at}} = \sum_{\sigma=\uparrow,\downarrow=\pm} \sigma B_z \Psi_\sigma^\dagger \Psi_\sigma + \left(\delta_A \Psi_\uparrow^\dagger \Psi_\downarrow^\dagger + \mathrm{h.c.}\right) + \sum_\sigma \left(\lambda_\sigma \Psi_\sigma^\dagger d + \mathrm{h.c.}\right). \tag{60}$$

In the even total parity basis (Equation 54), the matrix representation of the Hamiltonian is then instead of Equation 55 given by

$$\mathcal{H}_{\mathrm{at}}(\phi_1,\phi_2) = \begin{pmatrix} 0 & \delta_A^* & 0 & 0 \\ \delta_A & 0 & \lambda_\downarrow & -\lambda_\uparrow \\ 0 & \lambda_\downarrow^* & B_z & 0 \\ 0 & -\lambda_\uparrow^* & 0 & -B_z \end{pmatrix}. \tag{61}$$

Assuming $|\lambda_\uparrow| = |\lambda_\downarrow| \equiv \lambda$, Equation 56 then yields the eigenenergies $\pm\varepsilon_\pm$ with

$$\varepsilon_\pm = \frac{1}{\sqrt{2}} \begin{pmatrix} E_A^2 + B_z^2 + 2\lambda^2 \\ \pm\sqrt{\left(E_A^2 - B_z^2\right) + 4\lambda^2 \left(E_A^2 + B_z^2 + \lambda^2\right)} \end{pmatrix}^{1/2}. \tag{62}$$

Remarkably, the ABS spectra in Equation 62 and Equation 57 are rather similar for $\lambda^2 = \max\left(E_A^2, B_z^2\right)$. However, the MBS will automatically be located at zero energy and thus represents a generic situation.

Conclusion

We close this paper by summarizing our main findings. We have studied the Josephson effect in different setups involving both conventional *s*-wave BCS superconductors (S leads) and topologically nontrivial 1D *p*-wave superconductors (TS leads) with Majorana end states. The TS wires have been described either by a spinless theory applicable in the deep topological regime, which has the advantage of allowing for analytical progress but makes it difficult to establish contact to experimental control parameters, or by a spinful nanowire model as suggested in [2,3]. We have employed a unified imaginary-time Green's function approach to analyze the equilibrium properties of such devices, but a Keldysh generalization is straightforward and allows one to study also nonequilibrium applications.

For S–TS tunnel junctions, we find that in the topological phase of the TS wire, the supercurrent is mainly carried by above-gap continuum contributions. We confirm the expected supercurrent blockade [31] in the deep topological regime (where the spinless theory is fully valid and thus no residual *s*-wave pairing exists), while for realistic parameters, a small but finite critical current is found. To good approximation, the Josephson current obeys the usual 2π-periodic sinusoidal current–phase relation. The dependence of the critical current on the bulk Zeeman field driving the TS wire through the topological phase transition shows a kink-like feature at the critical value, which is caused by a sudden drop of the Andreev state contribution.

The supercurrent blockade in the deep topological phase could be lifted by adding a magnetic impurity to the junction, also allowing for the presence of a local magnetic field **B**. Such a magnetic impurity arises from a spin-degenerate quantum dot (QD), and we have studied the corresponding S–QD–TS problem for both the spinless and the spinful TS wire model. Based on analytical results valid in the cotunneling regime as well as numerical results within the mean-field approximation, we predict φ_0-junction behavior (anomalous Josephson effect) for the current–phase relation when the TS wire is in the topological phase.

As a final example for devices combining conventional and topological superconductors, we have shown that S–TS–S devices allow for a Majorana-induced parity switch between Andreev state sectors with different parity in a superconducting atomic contact. This observation could be useful for future microwave spectroscopy experiments of Andreev qubits in such contacts.

Acknowledgements

We acknowledge funding by the Deutsche Forschungsgemeinschaft (Grant No. EG 96/11-1) and by the Spanish MINECO through Grant No. FIS2014-55486-P and through the "María de Maeztu" Programme for Units of Excellence in R&D (MDM-2014-0377).

References

1. Kitaev, A. Yu. *Phys.-Usp.* **2001,** *44,* 131. doi:10.1070/1063-7869/44/10S/S29
2. Lutchyn, R. M.; Sau, J. D.; Das Sarma, S. *Phys. Rev. Lett.* **2010,** *105,* 077001. doi:10.1103/physrevlett.105.077001
3. Oreg, Y.; Refael, G.; von Oppen, F. *Phys. Rev. Lett.* **2010,** *105,* 177002. doi:10.1103/physrevlett.105.177002
4. Alicea, J.; Oreg, Y.; Refael, G.; von Oppen, F.; Fisher, M. P. A. *Nat. Phys.* **2011,** *7,* 412. doi:10.1038/nphys1915
5. Alicea, J. *Rep. Prog. Phys.* **2012,** *75,* 076501. doi:10.1088/0034-4885/75/7/076501
6. Leijnse, M.; Flensberg, K. *Semicond. Sci. Technol.* **2012,** *27,* 124003. doi:10.1088/0268-1242/27/12/124003
7. Beenakker, C. W. J. *Annu. Rev. Condens. Matter Phys.* **2013,** *4,* 113. doi:10.1146/annurev-conmatphys-030212-184337
8. Aasen, D.; Hell, M.; Mishmash, R. V.; Higginbotham, A.; Danon, J.; Leijnse, M.; Jespersen, T. S.; Folk, J. A.; Marcus, C. M.; Flensberg, K.; Alicea, J. *Phys. Rev. X* **2016,** *6,* 031016. doi:10.1103/physrevx.6.031016
9. Landau, L. A.; Plugge, S.; Sela, E.; Altland, A.; Albrecht, S. M.; Egger, R. *Phys. Rev. Lett.* **2016,** *116,* 050501. doi:10.1103/physrevlett.116.050501
10. Plugge, S.; Landau, L. A.; Sela, E.; Altland, A.; Flensberg, K.; Egger, R. *Phys. Rev. B* **2016,** *94,* 174514. doi:10.1103/physrevb.94.174514
11. Plugge, S.; Rasmussen, A.; Egger, R.; Flensberg, K. *New J. Phys.* **2017,** *19,* 012001. doi:10.1088/1367-2630/aa54e1
12. Aguado, R. *Riv. Nuovo Cimento Soc. Ital. Fis.* **2017,** *40,* 523. doi:10.1393/ncr/i2017-10141-9
13. Mourik, V.; Zuo, K.; Frolov, S. M.; Plissard, S. R.; Bakkers, E. P. A. M.; Kouwenhoven, L. P. *Science* **2012,** *336,* 1003. doi:10.1126/science.1222360
14. Das, A.; Ronen, Y.; Most, Y.; Oreg, Y.; Heiblum, M.; Shtrikman, H. *Nat. Phys.* **2012,** *8,* 887. doi:10.1038/nphys2479
15. Albrecht, S. M.; Higginbotham, A. P.; Madsen, M.; Kuemmeth, F.; Jespersen, T. S.; Nygård, J.; Krogstrup, P.; Marcus, C. M. *Nature* **2016,** *531,* 206. doi:10.1038/nature17162
16. Deng, M. T.; Vaitiekenas, S.; Hansen, E. B.; Danon, J.; Leijnse, M.; Flensberg, K.; Nygård, J.; Krogstrup, P.; Marcus, C. M. *Science* **2016,** *354,* 1557. doi:10.1126/science.aaf3961
17. Gül, Ö.; Zhang, H.; de Vries, F. K.; van Veen, J.; Zuo, K.; Mourik, V.; Conesa-Boj, S.; Nowak, M. P.; van Woerkom, D. J.; Quintero-Pérez, M.; Cassidy, M. C.; Geresdi, A.; Koelling, S.; Car, D.; Plissard, S. R.; Bakkers, E. P. A. M.; Kouwenhoven, L. P. *Nano Lett.* **2017,** *17,* 2690. doi:10.1021/acs.nanolett.7b00540
18. Albrecht, S. M.; Hansen, E. B.; Higginbotham, A. P.; Kuemmeth, F.; Jespersen, T. S.; Nygård, J.; Krogstrup, P.; Danon, J.; Flensberg, K.; Marcus, C. M. *Phys. Rev. Lett.* **2017,** *118,* 137701. doi:10.1103/physrevlett.118.137701
19. Zhang, H.; Gül, Ö.; Conesa-Boj, S.; Nowak, M. P.; Wimmer, M.; Zuo, K.; Mourik, V.; de Vries, F. K.; van Veen, J.; de Moor, M. W. A.; Bommer, J. D. S.; van Woerkom, D.; Car, D.; Plissard, S. R.; Bakkers, E. P. A. M.; Quintero-Pérez, M.; Cassidy, M. C.; Koelling, S.; Goswami, S.; Watanabe, K.; Taniguchi, T.; Kouwenhoven, L. P. *Nat. Commun.* **2017,** *8,* 16025. doi:10.1038/ncomms16025
20. Nichele, F.; Drachmann, A. C. C.; Whiticar, A. M.; O'Farrell, E. C. T.; Suominen, H. J.; Fornieri, A.; Wang, T.; Gardner, G. C.; Thomas, C.; Hatke, A. T.; Krogstrup, P.; Manfra, M. J.; Flensberg, K.; Marcus, C. M. *Phys. Rev. Lett.* **2017,** *119,* 136803. doi:10.1103/physrevlett.119.136803
21. Suominen, H. J.; Kjaergaard, M.; Hamilton, A. R.; Shabani, J.; Palmstrøm, C. J.; Marcus, C. M.; Nichele, F. *Phys. Rev. Lett.* **2017,** *119,* 176805. doi:10.1103/physrevlett.119.176805
22. Gazibegovich, S.; Car, D.; Zhang, H.; Balk, S. C.; Logan, J. A.; de Moor, M. W. A.; Cassidy, M. C.; Schmits, R.; Xu, D.; Wang, G.; Krogstrup, P.; Op het Veld, R. L. M.; Shen, J.; Bouman, D.; Shojaei, B.; Pennachio, D.; Lee, J. S.; van Veldhoven, P. J.; Koelling, S.; Verheijen, M. A.; Kouwenhoven, L. P.; Palmstrøm, C. J.; Bakkers, E. P. A. M. *Nature* **2017,** *548,* 434. doi:10.1038/nature23468
23. Zhang, H.; Liu, C.-X.; Gazibegovic, S.; Xu, D.; Logan, J. A.; Wang, G.; van Loo, N.; Bommer, J. D. S.; de Moor, M. W. A.; Car, D.; Op het Veld, R. L. M.; van Veldhoven, P. J.; Koelling, S.; Verheijen, M. A.; Pendharkar, M.; Pennachio, D. J.; Shojaei, B.; Lee, J. S.; Palmstrom, C. J.; Bakkers, E. P. A. M.; Das Sarma, S.; Kouwenhoven, L. P. *Nature* **2018,** *556,* 74–79. doi:10.1038/nature26142
24. Deng, M. T.; Vaitiekénas, S.; Prada, E.; San-José, P.; Nygård, J.; Krogstrup, P.; Aguado, R.; Marcus, C. M. *arXiv* **2017,** No. 1712.03536.
25. Laroche, D.; Bouman, D.; van Woerkom, D. J.; Proutski, A.; Murthy, C.; Pikulin, D. I.; Nayak, C.; van Gulik, R. J. J.; Nygård, J.; Krogstrup, P.; Kouwenhoven, L. P.; Geresdi, A. *arXiv* **2017,** No. 1712.08459.
26. Nadj-Perge, S.; Drozdov, I. K.; Li, J.; Chen, H.; Jeon, S.; Seo, J.; MacDonald, A. H.; Bernevig, B. A.; Yazdani, A. *Science* **2014,** *346,* 602. doi:10.1126/science.1259327
27. Ruby, M.; Pientka, F.; Peng, Y.; von Oppen, F.; Heinrich, B. W.; Franke, K. J. *Phys. Rev. Lett.* **2015,** *115,* 197204. doi:10.1103/physrevlett.115.197204
28. Sun, H.-H.; Zhang, K.-W.; Hu, L.-H.; Li, C.; Wang, G.-Y.; Ma, H.-Y.; Xu, Z.-A.; Gao, C.-L.; Guan, D.-D.; Li, Y.-Y.; Liu, C.; Qian, D.; Zhou, Y.; Fu, L.; Li, S.-C.; Zhang, F.-C.; Jia, J.-F. *Phys. Rev. Lett.* **2016,** *116,* 257003. doi:10.1103/physrevlett.116.257003
29. Feldman, B. E.; Randeria, M. T.; Li, J.; Jeon, S.; Xie, Y.; Wang, Z.; Drozdov, I. K.; Andrei Bernevig, B.; Yazdani, A. *Nat. Phys.* **2017,** *13,* 286. doi:10.1038/nphys3947
30. Deacon, R. S.; Wiedenmann, J.; Bocquillon, E.; Domínguez, F.; Klapwijk, T. M.; Leubner, P.; Brüne, C.; Hankiewicz, E. M.; Tarucha, S.; Ishibashi, K.; Buhmann, H.; Molenkamp, L. W. *Phys. Rev. X* **2017,** *7,* 021011. doi:10.1103/physrevx.7.021011
31. Zazunov, A.; Egger, R. *Phys. Rev. B* **2012,** *85,* 104514. doi:10.1103/physrevb.85.104514

32. Kwon, H.-J.; Sengupta, K.; Yakovenko, V. M. *Eur. Phys. J. B* **2004,** *37,* 349. doi:10.1140/epjb/e2004-00066-4
33. Bratus, E. N.; Shumeiko, V. S.; Wendin, G. *Phys. Rev. Lett.* **1995,** *74,* 2110. doi:10.1103/physrevlett.74.2110
34. Averin, D.; Bardas, A. *Phys. Rev. Lett.* **1995,** *75,* 1831. doi:10.1103/physrevlett.75.1831
35. Cuevas, J. C.; Martín-Rodero, A.; Levy Yeyati, A. *Phys. Rev. B* **1996,** *54,* 7366. doi:10.1103/physrevb.54.7366
36. Nazarov, Y.; Blanter, Y. *Quantum Transport: Introduction to Nanoscience;* Cambridge University Press: Cambridge, United Kingdom, 2010.
37. Peng, Y.; Pientka, F.; Vinkler-Aviv, Y.; Glazman, L. I.; von Oppen, F. *Phys. Rev. Lett.* **2015,** *115,* 266804. doi:10.1103/physrevlett.115.266804
38. Ioselevich, P. A.; Ostrovsky, P. M.; Feigel'man, M. V. *Phys. Rev. B* **2016,** *93,* 125435. doi:10.1103/physrevb.93.125435
39. Sharma, G.; Tewari, S. *Phys. Rev. B* **2016,** *93,* 195161. doi:10.1103/physrevb.93.195161
40. Zazunov, A.; Egger, R.; Levy Yeyati, A. *Phys. Rev. B* **2016,** *94,* 014502. doi:10.1103/physrevb.94.014502
41. Setiawan, F.; Cole, W. S.; Sau, J. D.; Das Sarma, S. *Phys. Rev. B* **2017,** *95,* 174515. doi:10.1103/PhysRevB.95.174515
42. Setiawan, F.; Cole, W. S.; Sau, J. D.; Das Sarma, S. *Phys. Rev. B* **2017,** *95,* 020501. doi:10.1103/physrevb.95.020501
43. Zazunov, A.; Egger, R.; Alvarado, M.; Levy Yeyati, A. *Phys. Rev. B* **2017,** *96,* 024516. doi:10.1103/physrevb.96.024516
44. Deb, O.; Sengupta, K.; Sen, D. *arXiv* **2017,** No. 1712.03726.
45. Buzdin, A. *Phys. Rev. Lett.* **2008,** *101,* 107005. doi:10.1103/physrevlett.101.107005
46. Zazunov, A.; Egger, R.; Jonckheere, T.; Martin, T. *Phys. Rev. Lett.* **2009,** *103,* 147004. doi:10.1103/physrevlett.103.147004
47. Schrade, C.; Hoffman, S.; Loss, D. *Phys. Rev. B* **2017,** *95,* 195421. doi:10.1103/physrevb.95.195421
48. Yokoyama, T.; Eto, M.; Nazarov, Y. V. *Phys. Rev. B* **2014,** *89,* 195407. doi:10.1103/physrevb.89.195407
49. Camjayi, A.; Arrachea, L.; Aligia, A.; von Oppen, F. *Phys. Rev. Lett.* **2017,** *119,* 046801. doi:10.1103/physrevlett.119.046801
50. Cayao, J.; San-José, P.; Black-Schaffer, A. M.; Aguado, R.; Prada, E. *Phys. Rev. B* **2017,** *96,* 205425. doi:10.1103/physrevb.96.205425
51. Cayao, J.; San-José, P.; Black-Schaffer, A. M.; Prada, E.; Aguado, R. *arXiv* **2017,** No. 1712.08127.
52. Bretheau, L.; Girit, Ç. Ö.; Pothier, H.; Esteve, D.; Urbina, C. *Nature* **2013,** *499,* 312. doi:10.1038/nature12315
53. Bretheau, L.; Girit, Ç. Ö.; Urbina, C.; Esteve, D.; Pothier, H. *Phys. Rev. X* **2013,** *3,* 041034. doi:10.1103/physrevx.3.041034
54. Janvier, C.; Tosi, L.; Bretheau, L.; Girit, Ç. Ö.; Stern, M.; Bertet, P.; Joyez, P.; Vion, D.; Esteve, D.; Goffman, M. F.; Pothier, H.; Urbina, C. *Science* **2015,** *349,* 1199. doi:10.1126/science.aab2179
55. Tarasinski, B.; Chevallier, D.; Hutasoit, J. A.; Baxevanis, B.; Beenakker, C. W. J. *Phys. Rev. B* **2015,** *92,* 144306. doi:10.1103/physrevb.92.144306
56. Glazman, L. I.; Matveev, K. A. *JETP Lett.* **1989,** *49,* 659.
57. Rozhkov, A. V.; Arovas, D. P. *Phys. Rev. Lett.* **1999,** *82,* 2788. doi:10.1103/physrevlett.82.2788
58. Vecino, E.; Martín-Rodero, A.; Levy Yeyati, A. *Phys. Rev. B* **2003,** *68,* 035105. doi:10.1103/physrevb.68.035105
59. Siano, F.; Egger, R. *Phys. Rev. Lett.* **2004,** *93,* 047002. doi:10.1103/physrevlett.93.047002
60. Choi, M.-S.; Lee, M.; Kang, K.; Belzig, W. *Phys. Rev. B* **2004,** *70,* 020502. doi:10.1103/physrevb.70.020502
61. Karrasch, C.; Oguri, A.; Meden, V. *Phys. Rev. B* **2008,** *77,* 024517. doi:10.1103/physrevb.77.024517
62. Martín-Rodero, A.; Levi Yeyati, A. *Adv. Phys.* **2011,** *60,* 899. doi:10.1080/00018732.2011.624266
63. Luitz, D. J.; Assaad, F. F.; Novotný, T.; Karrasch, C.; Meden, V. *Phys. Rev. Lett.* **2012,** *108,* 227001. doi:10.1103/physrevlett.108.227001
64. Kasumov, A. Yu.; Deblock, R.; Kociak, M.; Reulet, B.; Bouchiat, H.; Khodos, I. I.; Gorbatov, Yu. B.; Volkov, V. T.; Journet, C.; Burghard, M. *Science* **1999,** *284,* 1508. doi:10.1126/science.284.5419.1508
65. van Dam, J. A.; Nazarov, Y. V.; Bakkers, E. P. A. M.; De Franceschi, S.; Kouwenhoven, L. P. *Nature* **2006,** *442,* 667. doi:10.1038/nature05018
66. Cleuziou, J.-P.; Wernsdorfer, W.; Bouchiat, V.; Ondarçuhu, T.; Monthioux, M. *Nat. Nanotechnol.* **2006,** *1,* 53. doi:10.1038/nnano.2006.54
67. Ingerslev Jørgensen, H.; Novotný, T.; Grove-Rasmussen, K.; Flensberg, K.; Lindelof, P. E. *Nano Lett.* **2007,** *7,* 2441. doi:10.1021/nl071152w
68. Eichler, A.; Deblock, R.; Weiss, M.; Karrasch, C.; Meden, V.; Schönenberger, C.; Bouchiat, H. *Phys. Rev. B* **2009,** *79,* 161407. doi:10.1103/physrevb.79.161407
69. Delagrange, R.; Luitz, D. J.; Weil, R.; Kasumov, A.; Meden, V.; Bouchiat, H.; Deblock, R. *Phys. Rev. B* **2015,** *91,* 241401. doi:10.1103/physrevb.91.241401
70. Zazunov, A.; Levy Yeyati, A.; Egger, R. *Phys. Rev. B* **2011,** *84,* 165440. doi:10.1103/physrevb.84.165440
71. Peng, Y.; Bao, Y.; von Oppen, F. *Phys. Rev. B* **2017,** *95,* 235143. doi:10.1103/physrevb.95.235143
72. Brunetti, A.; Zazunov, A.; Kundu, A.; Egger, R. *Phys. Rev. B* **2013,** *88,* 144515. doi:10.1103/physrevb.88.144515
73. Szombati, D. B.; Nadj-Perge, S.; Car, D.; Plissard, S. R.; Bakkers, E. P. A. M.; Kouwenhoven, L. P. *Nat. Phys.* **2016,** *12,* 568. doi:10.1038/nphys3742
74. Leijnse, M.; Flensberg, K. *Phys. Rev. Lett.* **2011,** *107,* 210502. doi:10.1103/physrevlett.107.210502
75. Sticlet, D.; Bena, C.; Simon, P. *Phys. Rev. Lett.* **2012,** *108,* 096802. doi:10.1103/physrevlett.108.096802
76. Prada, E.; San-Jose, P.; Aguado, R. *Phys. Rev. B* **2012,** *86,* 180503. doi:10.1103/physrevb.86.180503
77. Prada, E.; Aguado, R.; San-Jose, P. *Phys. Rev. B* **2017,** *96,* 085418. doi:10.1103/physrevb.96.085418
78. Hoffman, S.; Chevallier, D.; Loss, D.; Klinovaja, J. *Phys. Rev. B* **2017,** *96,* 045440. doi:10.1103/physrevb.96.045440
79. Martin-Rodero, A.; Levy Yeyati, A. *J. Phys.: Condens. Matter* **2012,** *24,* 385303. doi:10.1088/0953-8984/24/38/385303
80. Balatsky, A. V.; Vekhter, I.; Zhu, J.-X. *Rev. Mod. Phys.* **2006,** *78,* 373. doi:10.1103/revmodphys.78.373
81. Zazunov, A.; Shumeiko, V. S.; Bratus', E. N.; Lantz, J.; Wendin, G. *Phys. Rev. Lett.* **2003,** *90,* 087003. doi:10.1103/physrevlett.90.087003

A.2 Boundary Green's function approach for spinful single-channel and multichannel Majorana nanowires

M. Alvarado, A. Iks, A. Zazunov, R. Egger, and A. Levy Yeyati, Boundary Green's function approach for spinful single-channel and multichannel Majorana nanowires, Phys. Rev. B 101, 094511 (2020)

In this paper I contributed in scientific discussions, work and preparation of the manuscript. I partook in the calculation of examples for topological Josephson junctions.

Boundary Green's function approach for spinful single-channel and multichannel Majorana nanowires

M. Alvarado ,[1] A. Iks,[2] A. Zazunov ,[2] R. Egger ,[2] and A. Levy Yeyati [1]
[1]*Departamento de Física Teórica de la Materia Condensada C-V, Condensed Matter Physics Center (IFIMAC) and Instituto Nicolás Cabrera, Universidad Autónoma de Madrid, E-28049 Madrid, Spain*
[2]*Institut für Theoretische Physik, Heinrich-Heine-Universität, D-40225 Düsseldorf, Germany*

(Received 13 December 2019; revised manuscript received 29 January 2020; accepted 26 February 2020; published 11 March 2020)

The boundary Green's-function (bGF) approach has been established as a powerful theoretical technique for computing the transport properties of tunnel-coupled hybrid nanowire devices. Such nanowires may exhibit topologically nontrivial superconducting phases with Majorana bound states at their boundaries. We introduce a general method for computing the bGF of spinful multichannel lattice models for such Majorana nanowires, where the bGF is expressed in terms of the roots of a secular polynomial evaluated in complex momentum space. In many cases, those roots, and thus the bGF, can be accurately described by simple analytical expressions, while otherwise our approach allows for the numerically efficient evaluation of bGFs. We show that from the behavior of the roots many physical quantities of key interest can be inferred, e.g., the value of bulk topological invariants, the energy dependence of the local density of states, or the spatial decay of subgap excitations. We apply the method to single- and two-channel nanowires of symmetry class D or DIII. In addition, we study the spectral properties of multiterminal Josephson junctions made out of such Majorana nanowires.

DOI: 10.1103/PhysRevB.101.094511

I. INTRODUCTION

The interest in proximitized nanostructures where topological superconductor phases could be engineered is continuing to grow [1–8]. In particular, the case of one-dimensional (1D) semiconducting hybrid nanowires with strong Rashba spin-orbit interaction has been intensely studied as a potential route towards the generation of Majorana bound states (MBSs) [9–17]. Such states are of high interest for topological quantum information processing applications [4]. While a phase with broken time-reversal symmetry (class D) can be expected for the cited nanowire experiments because of the presence of a magnetic Zeeman field (we use the abbreviation "TS" for such topological superconductors below), a time-reversal invariant topological superconductor (TRITOPS) phase has been predicted from related wire constructions [18–35]. The TRITOPS phase has symmetry class DIII and is still awaiting experimental tests. The interest in hybrid nanowires goes well beyond the generation of topological phases. For instance, recent microwave spectroscopy experiments have investigated the role of spin-orbit coupling effects on the formation of Andreev bound states [36].

The physics of devices made from different types of nanowires coupled by tunneling contacts has been explored by a variety of theoretical models and techniques [1–3,5]. On one hand, minimal models restrict the Hilbert space to include only subgap bound states. This key simplification then allows for analytical progress (see, e.g., Refs. [37,38] for early contributions). On the other hand, microscopic models aim for a more detailed understanding of how material properties can influence transport observables (see, e.g., Refs. [39–46]). Recent works along this line have studied the electrostatic potential profile along the nanowire [47–49] and the effects of disorder on the phase diagram [50,51]. However, the solution of such microscopic models requires information about many model parameter values and generally can be obtained only by performing a detailed numerical analysis. In this context, theoretical approaches of *intermediate* complexity are of high interest. Such a framework allows one to describe transport properties by taking into account both subgap and continuum states while keeping the algebra sufficiently simple so as to permit analytical progress. The scattering matrix formalism is a widely known representative for this type of approach (see, e.g., Refs. [52–58]). The present paper will employ the complementary boundary Green's-function (bGF) method [59–64], which is particularly useful for analyzing nonequilibrium transport properties in different types of hybrid nanojunctions. The bGF approach also allows one to examine other electronic properties such as the tunneling density of states (DoSs) or the bulk-boundary correspondence expected for topological phases [65–67]. Furthermore, electron-phonon and/or electron-electron interaction effects can in principle also be taken into account.

In the present paper, we extend and generalize the bGF approach for 1D or quasi-1D proximitized nanowires, which has been introduced in Refs. [59–63], along several directions. First, we demonstrate that a bGF construction in terms of the roots of a secular equation extended to complex momenta (as discussed in Ref. [59] for the Kitaev chain model) can be generalized to arbitrary spinful multichannel (i.e., quasi-1D) nanowires with topologically nontrivial superconducting phases. In particular, by studying the evolution of the roots in the complex momentum plane under the variation of model parameters, one can readily detect topological transitions, determine bulk topological invariants, or compute the local density of states as a function of energy for translationally invariant cases. In addition, the same roots determine the bGF and thereby give access to the transport properties of devices made from tunnel-coupled (semi-infinite or finite-length) nanowires. In particular, their knowledge also gives access to the spatial decay profile of Majorana states.

Below we investigate the roots and the corresponding bGFs for two widely used spinful single-channel nanowire models harboring topologically nontrivial phases. First, we study TS wires with broken time-reversal invariance using the model by Lutchyn *et al.* [68] and by Oreg *et al.* [69]. Second, we consider TRITOPS wires using the model of Zhang *et al.* [21]. Quasi-1D multichannel models in class D or class DIII are then constructed by coupling several wires of the respective symmetry class by tunnel couplings. We show that also such multichannel models can be efficiently tackled by our bGF method. As application, we will discuss the Josephson current-phase relation both for a multiterminal junction composed of three tunnel-coupled TS wires and for a TRITOPS-TS Josephson junction.

The remainder of this paper is organized as follows. In Sec. II, we describe a general formalism for analyzing 1D or quasi-1D lattice models of proximitized nanowires, where we only assume that the hopping amplitudes in the corresponding tight-binding model are of finite range. We show that the real-space bulk Green's function (GF) adopts a compact expression in terms of the roots of the secular polynomial of the bulk Hamiltonian extended into complex momentum space. We also show how the boundary GF can be obtained from the bulk GF by solving a Dyson equation, and we discuss general properties of the corresponding roots. In Sec. III, we consider a discretized version of the single-channel class-D model of Refs. [68,69]. We introduce a simple ansatz for the respective roots in the trivial and in the topological phase. This ansatz allows us to obtain analytical insights about the bulk spectral density and the spatial variation of MBSs. In Sec. IV, we extend the analysis to a two-channel model describing two coupled class-D wires, where we can study spin-orbit interaction effects in multichannel nanowires [70]. The phase diagram and the spectral density of this model show a richer behavior than in the single-channel case. In Sec. V, we apply our methods to single- and multichannel models for TRITOPS wires. Finally, in Sec. VI, we study the Josephson effect and the formation of Andreev bound states in phase-biased multiterminal TS junctions and for TRITOPS-TS junctions. We finally offer some conclusions in Sec. VII. Technical details have been delegated to two appendices. We often use units with $\hbar = 1$ and focus on the zero-temperature limit throughout.

II. BOUNDARY GREEN'S FUNCTION

A central aim of the present paper is to construct the bGF for different hybrid nanowire models which are described by a bulk Hamiltonian of the form

$$H_{\text{bulk}} = \frac{1}{2}\sum_k \hat{\Psi}_k^\dagger \hat{\mathcal{H}}(k)\hat{\Psi}_k, \tag{1}$$

corresponding to an infinitely long and translationally invariant (quasi-)1D chain with lattice spacing a. Here, $\hat{\mathcal{H}}(k)$ is an $N \times N$ Bogoliubov–de Gennes (BdG) Hamiltonian in reciprocal space, and the $\hat{\Psi}_k$ are fermionic Nambu spinor fields. Specific examples for these spinor fields will be given in the subsequent sections. The number N may include the Nambu index, the spin degree of freedom, and channel indices for multichannel models. Using $\hat{\mathcal{H}}(k + 2\pi/a) = \hat{\mathcal{H}}(k)$, the BdG Hamiltonian can be expanded in a Fourier series, $\hat{\mathcal{H}}(k) = \sum_n \hat{\mathcal{V}}_n e^{inka}$, where Hermiticity implies $\hat{\mathcal{V}}_{-n} = \hat{\mathcal{V}}_n^\dagger$. For simplicity, we here consider only models with nearest-neighbor hopping, $\hat{\mathcal{V}}_n = 0$ for $|n| > 1$, but the generalization to arbitrary finite-range hopping amplitudes is straightforward.

The retarded bulk GF of the infinite chain is defined as

$$\hat{G}^R(k, \omega) = [\omega + i0^+ - \hat{\mathcal{H}}(k)]^{-1}, \tag{2}$$

where the $N \times N$ matrix structure is indicated by the hat notation. In real-space representation, the GF has the components (j and j' are lattice site indices)

$$\hat{G}^R_{jj'}(\omega) = \frac{a}{2\pi}\int_{-\pi/a}^{\pi/a} dk\, e^{i(j-j')ka}\,\hat{G}^R(k, \omega). \tag{3}$$

By the identification $z = e^{ika}$, this integral is converted into a complex contour integral:

$$\hat{G}^R_{jj'}(\omega) = \frac{1}{2\pi i}\oint_{|z|=1}\frac{dz}{z} z^{j-j'}\hat{G}^R(z, \omega). \tag{4}$$

Introducing the roots $z_n(\omega)$ of the secular polynomial in the complex-z plane,

$$P(z, \omega) = \det[\omega - \hat{\mathcal{H}}(z)] = \frac{1}{z^N}\prod_{n=1}^{2N}[z - z_n(\omega)], \tag{5}$$

the contour integral (4) can be written as a sum over the residues of all roots inside the unit circle:

$$\hat{G}^R_{jj'}(\omega) = \sum_{|z_n|<1}\frac{z_n^{j-j'}\hat{A}(z_n, \omega)}{\prod_{m\neq n}(z_n - z_m)}, \tag{6}$$

where $\hat{A}(z, \omega)$ is the cofactor matrix of $[\omega - \mathcal{H}(z)]z$. For notational simplicity, we omit the superscript "R" in retarded GFs from now on.

Given the real-space components of the bulk GF in Eq. (6), we next employ Ref. [59] (see also Ref. [71]) to derive the bGF characterizing a *semi-infinite* nanowire. To that effect, we add an impurity potential ϵ localized at lattice site $j = 0$. Taking the limit $\epsilon \to \infty$, the infinite chain is cut into disconnected semi-infinite chains with $j < -1$ (left side, L) and $j > 1$ (right side, R). Using the Dyson equation, the local GF components of the cut nanowire follow as [59]

$$\hat{\mathcal{G}}_{jj}(\omega) = \hat{G}_{jj}(\omega) - \hat{G}_{j0}(\omega)[\hat{G}_{00}(\omega)]^{-1}\hat{G}_{0j}(\omega). \tag{7}$$

The bGFs for the left and right semi-infinite chain, respectively, are with Eq. (7) given by

$$\hat{\mathcal{G}}_L(\omega) = \hat{\mathcal{G}}_{-1,-1}(\omega), \quad \hat{\mathcal{G}}_R(\omega) = \hat{\mathcal{G}}_{11}(\omega). \tag{8}$$

We note that by proceeding along the lines of Refs. [60,72] one can also compute reflection matrices from the corresponding bGF:

$$\hat{r}_{L/R} = \lim_{\omega\to 0} \frac{\mathbb{1} - i\hat{\mathcal{V}}^\dagger_{\pm 1}\hat{\mathcal{G}}_{L/R}(\omega)\hat{\mathcal{V}}_{\pm 1}}{\mathbb{1} + i\hat{\mathcal{V}}^\dagger_{\pm 1}\hat{\mathcal{G}}_{L/R}(\omega)\hat{\mathcal{V}}_{\pm 1}}. \tag{9}$$

This relation allows one to express topological invariants of the bulk Hamiltonian [66,67] in terms of bGFs.

The roots $z_n(\omega)$ play an important role in what follows. In particular, their knowledge allows us to construct both the bulk and the boundary GFs. In simple cases, this can be done analytically, and otherwise this route offers an efficient numerical scheme. The roots can also provide detailed information about the decay of subgap states localized at the boundaries of semi-infinite wires, and they allow one to compute topological invariants of the bulk system. Let us therefore summarize some general properties of these roots.

(i) Hermiticity of the BdG Hamiltonian implies that every root $z_n(\omega)$ is accompanied by a root $1/z_n^*(\omega)$, where "$*$" denotes complex conjugation.

(ii) Electron-hole symmetry of the BdG Hamiltonian implies that $z_n(\omega) = z_n^*(-\omega)$. In the presence of an additional symmetry $\hat{\mathcal{H}}(k) = \hat{U}\hat{\mathcal{H}}(-k)\hat{U}^\dagger$ with a unitary matrix $\hat{U}$, for every root $z_n(\omega)$, also $z_n^*(\omega)$ must be a root.

(iii) As a consequence of (i) and (ii), $\prod_{n=1}^{2N} z_n(\omega) = 1$.

(iv) Topological phase transitions can occur once a pair of zero-energy roots hits the unit circle, $|z_n(0)| = 1$, which corresponds to the closing and reopening of a gap in the bulk spectrum.

(v) Equations (6) and (7) imply that subgap bound states (with energy E) localized near the boundary of a semi-infinite wire decay into the bulk in a manner controlled by $\max(|z_n(E)| < 1)$.

We illustrate the usefulness of these properties in the following sections for different models of proximitized (quasi-) 1D nanowires.

III. SPINFUL SINGLE-CHANNEL HYBRID NANOWIRES

As a first example, we consider the spinful single-channel model of Refs. [68,69] for a proximitized semiconductor nanowire. This model has been extensively studied as a prototype for 1D wires harboring a TS phase with broken time-reversal invariance. We use the Nambu bispinor $\hat{\Psi}_k^T = (c_{k\uparrow}, c_{k\downarrow}, c^\dagger_{-k\downarrow}, -c^\dagger_{-k\uparrow})$, i.e., $N = 4$ in Eq. (1). Here, $c_{k\sigma}$ is a fermionic annihilation operator for momentum k and spin $\sigma =\uparrow, \downarrow$, and the bulk BdG Hamiltonian in Eq. (1) takes the form

$$\mathcal{H}(k) = \epsilon_k\sigma_0\tau_z + V_x\sigma_x\tau_0 + \alpha_k\sigma_z\tau_z + \Delta\sigma_0\tau_x, \tag{10}$$

where $\sigma_{x,y,z}$ and $\tau_{x,y,z}$ are Pauli matrices in spin and Nambu (electron-hole) space, respectively, with the identity matrices σ_0 and τ_0. Regularizing the continuum model of Refs. [68,69] by imposing a finite lattice spacing a, the kinetic energy $\epsilon_k = 2t[1 - \cos(ka)] - \mu$ includes the chemical potential μ and the nearest-neighbor hopping amplitude t. Furthermore, V_x encapsulates a magnetic Zeeman field oriented along the wire axis, $\alpha_k = \alpha\sin(ka)$ describes the spin-orbit interaction, and Δ refers to the proximity-induced on-site pairing amplitude. The bulk dispersion relation, $E = E_{k,\pm} \geqslant 0$, then follows from [68,69]

$$E^2_{k,\pm} = \Delta^2 + \alpha_k^2 + V_x^2 + \epsilon_k^2 \pm 2\sqrt{\Delta^2V_x^2 + \left(\alpha_k^2 + V_x^2\right)\epsilon_k^2}. \tag{11}$$

This model exhibits a topological transition at $V_x = V_c = \sqrt{\Delta^2 + \mu^2}$, where the TS phase is realized for $V_x > V_c$.

Although it is not essential for the subsequent discussion, the parameters t and α can be assigned values appropriate for InAs nanowires [59]. To that end, we put $t = \hbar^2/(2m^*a^2)$, where m^* is the effective mass, and $\alpha = \hbar u/a$, where u is the spin-orbit parameter [69]. This parameter depends on material properties and can be tuned by an external electric field. Putting $a = 10$ nm and using typical InAs material parameters, we estimate $t \approx 10$ meV and $\alpha \approx 4$ meV [59]. On the other hand, a proximity gap of order $\Delta \approx 0.2$ meV represents the case of a nanowire in good contact with a superconducting Al layer. (We will use this value in the figures below unless noted otherwise.) The only remaining free variables are then given by V_x and μ.

Using Eq. (5) and $z = e^{ika}$, the roots $z_n(\omega)$ for this model satisfy the condition

$$\begin{aligned}
&2\Delta^2\left[\tilde{\alpha}^2(z) + \epsilon^2(z) - V_x^2 - \omega^2\right] \\
&+ 2\tilde{\alpha}^2(z)\left[V_x^2 - \omega^2 - \epsilon^2(z)\right] + \tilde{\alpha}^4(z) + V_x^4 + \Delta^4 \\
&+ [\omega^2 - \epsilon^2(z)]^2 - 2V_x^2[\omega^2 + \epsilon^2(z)] = 0,
\end{aligned} \tag{12}$$

with the functions

$$\tilde{\alpha}(z) = -i\alpha(z - z^{-1})/2, \quad \epsilon(z) = -t(z + z^{-1} - 2) - \mu. \tag{13}$$

Equation (12) can be written as

$$\sum_{n=1}^{4} C_n(\omega)\left(z^n + \frac{1}{z^n}\right) + C_0(\omega) = 0, \tag{14}$$

where the real coefficients $C_n(\omega)$ are given in Appendix A. Clearly, Eq. (14) is consistent with the general properties (i) and (ii) listed in Sec. II. Alternatively, Eq. (14) can be expressed as an eighth-order polynomial equation:

$$\sum_{m=0}^{8} a_m(\omega)z^m = 0, \tag{15}$$

where the coefficients a_m are trivially related to the C_n and we can impose the normalization conditions $a_0 = a_8 = 1$.

The resulting roots z_n can be grouped into two different classes associated with the two pairing gaps Δ_1 and Δ_2 in the bulk spectrum [68,69] [see Fig. 1(a)]. In the limit $\Delta \to 0$, these gaps Δ_1 and Δ_2 will also vanish. For $\Delta = 0$, we find from Eq. (12) that the zero-frequency roots $z_n(\omega = 0)$ simplify to $e^{\pm ik_1a}$ and $e^{\pm ik_2a}$, with

$$k_{1,2} \simeq \cos^{-1}\left(\frac{2t(2t-\mu)}{\alpha^2 + 4t^2} + \pm\frac{\sqrt{V_x^2(\alpha^2 + 4t^2) + \alpha^4 + 4t\mu\alpha^2 - \alpha^2\mu^2}}{\alpha^2 + 4t^2}\right). \tag{16}$$

At these momenta, the dispersion relation becomes gapless for $\Delta = 0$ [see Fig. 1(a)]. We observe from Eq. (16) that k_1 (corresponding to the $+$ sign) becomes purely imaginary for

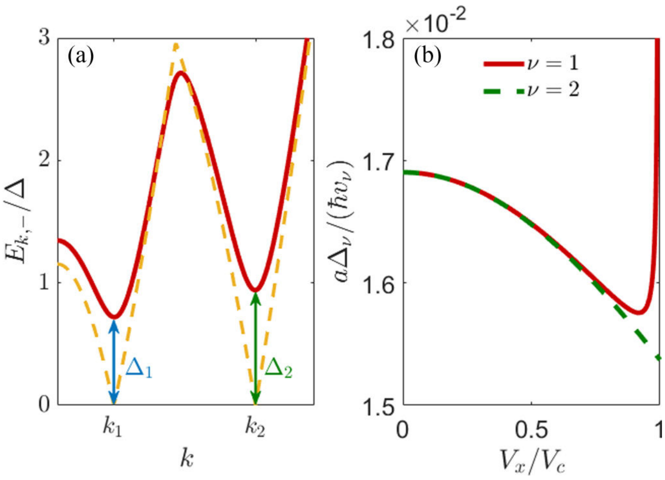

FIG. 1. Bulk dispersion relation of the spinful single-channel Majorana wire model [68,69]. (a) $E_{k,-}$ vs k [see Eq. (11)] for the topologically trivial regime $V_x < V_c$ (solid red curve), indicating the two pairing gaps Δ_1 and Δ_2 at $k = k_1$ and k_2, respectively [see Eq. (16)]. We use $\mu = 5$ meV, $\Delta = 2$ meV, and $V_x = 0.5V_c$. All other parameters are specified in the main text. The dashed yellow curve is for $\Delta = 0$. (b) Evolution of the two gaps (normalized to the velocities $v_{1,2}$) vs Zeeman parameter V_x for $\Delta = 0.2$ meV and $\mu = 2$ meV. We note that Δ_1 and v_1 simultaneously vanish as $V_x \to V_c$.

$V_x > V_c$. We will then first discuss the topologically trivial regime $V_x < V_c$.

Figure 1(a) shows that the low-energy physics will be dominated by the regions with $|k| \approx k_1$ and k_2. The pairing gaps $\Delta_{1,2} = |E_{k_{1,2},-}|$ then follow by substituting $k_{1,2}$ into the bulk dispersion relation (11). In particular, we find that Δ_1 closes and reopens when ramping V_x through the topological transition at $V_x = V_c$. An approximate expression for the roots is obtained by linearizing the $\Delta = 0$ dispersion relation in Eq. (11) for electrons and holes near $k = k_1$ and k_2. Defining the respective velocities as $v_{\nu=1,2} = |\partial_k E_{k=k_\nu,-}|_{\Delta=0}$, the effective low-energy Nambu Hamiltonian valid near the respective momentum k_ν can be written as

$$\mathcal{H}_{\mathrm{eff},\nu=1,2}(k) \simeq \begin{pmatrix} v_\nu(k-k_\nu) & \Delta_\nu \\ \Delta_\nu & -v_\nu(k-k_\nu) \end{pmatrix}, \tag{17}$$

and similarly for $k \approx -k_\nu$. Using $ika = \ln z$, the condition $\det[\omega - \mathcal{H}_{\mathrm{eff},\nu}(z)] = 0$ can readily be solved. In effect, the roots are given by

$$z_\nu(\omega) \simeq \left(1 \pm \frac{a}{v_\nu}\sqrt{\Delta_\nu^2 - \omega^2}\right) e^{ik_\nu a}, \tag{18}$$

plus the complex conjugate values. Inspired by Eq. (18), we propose the following ansatz for the roots $z_n(\omega)$ located *inside* the unit circle:

$$z_\nu(\omega) = \left(1 - \tau_\nu\sqrt{\Delta_\nu^2 - \omega^2}\right) e^{i\delta_\nu}, \tag{19}$$

where $\tau_{1,2}$ and $\delta_{1,2}$ are phenomenological coefficients. In addition, the complex conjugate root $z_\nu^*(\omega)$ is a solution. This ansatz is expected to work well in the topologically trivial regime $V_x < V_c$. For small Δ and $|\omega|$, Eq. (18) implies the limiting behavior $\tau_\nu = a/v_\nu$ and $\delta_\nu = k_\nu a$. In addition, we also impose the condition

$$\tau_1\Delta_1 = \tau_2\Delta_2 = \eta \ll 1, \tag{20}$$

where η is a small parameter. In the small-Δ case with $\tau_\nu \approx a/v_\nu$, Eq. (20) implies that the effective pairing gap Δ_ν is inversely proportional to the corresponding density of states $\propto 1/v_\nu$. Figure 1(b) shows that this condition is accurately fulfilled as long as V_x stays well below V_c. However, Eq. (20) becomes less precise for $V_x \to V_c$. In Appendix A, we provide more refined analytical expressions that determine the parameters η and δ_ν in our ansatz for the roots [see Eqs. (19) and (20)].

Next we turn to the topologically nontrivial regime $V_x > V_c$, where the momentum k_1 in Eq. (16) becomes purely imaginary. We should then replace $\delta_1 \to i\delta_1$ in the above ansatz for the roots. As a consequence, the $z_{\nu=1}(\omega)$ roots become real valued, and the ansatz for $V_x > V_c$ takes the form

$$z_{1,\pm}(\omega) = \left(1 \pm \tau_1\sqrt{\Delta_1^2 - \omega^2}\right) e^{-\delta_1},$$
$$z_{2,\pm}(\omega) = \left(1 - \tau_2\sqrt{\Delta_2^2 - \omega^2}\right) e^{\pm i\delta_2}, \tag{21}$$

where both δ_1 and δ_2 are real positive. We thus have only a single pair of complex conjugate roots (z_2) near the unit circle for $V_x > V_c$. Accurate analytical results for the δ_ν and τ_ν parameters can be obtained by solving a cubic equation (see Appendix A). As illustrated in Figs. 2(c) and 2(d), Eq. (21) captures the low-energy behavior of the roots rather well, especially in cases where electron-hole symmetry is approximately realized.

For this model of symmetry class D, the $\mathbb{Z}_2$ bulk topological invariant takes the form [1]

$$Q = \frac{\mathrm{sgn}\,\mathrm{Pf}\,\hat{\mathcal{H}}(k=0)}{\mathrm{sgn}\,\mathrm{Pf}\,\hat{\mathcal{H}}(k=\pi/a)} = \pm 1. \tag{22}$$

Interestingly, the number N_p of complex conjugate root pairs near (but inside) the unit circle is in correspondence with the topological invariant, $Q = (-1)^{N_p}$. These roots can be unambiguously identified as the ones approaching the unit circle from inside in the limit $\Delta \to 0$, corresponding to the Fermi points in the normal phase. For an odd (even) number of pairs, the phase is thus topologically nontrivial with $Q = -1$ (trivial with $Q = 1$). The upper panels in Fig. 2 illustrate the distribution of the roots inside the unit circle for the cases $V_x < V_c$ and $V_x > V_c$. We observe that upon entering the topologically nontrivial regime the complex conjugate z_1 roots coalesce to form an almost degenerate root pair $z_{1,\pm}$ [see Eq. (21)] located on the real axis inside the unit circle. The roots on the real axis correspond to additional bands at high energies above Δ. At the same time, a single pair of complex conjugate roots (z_2) remains near (but inside) the unit circle, as one expects for a topologically nontrivial phase. As remarked above, this change in the structure of the roots across the transition is consistent with the corresponding change in the topological invariant. The transition between both regions happens when the Pfaffian, or equivalently the Hamiltonian determinant, at $k = 0$ vanishes. Using the relation $\det \hat{\mathcal{H}}(k=0) = \prod_{n=1}^{8}[1 - z_n(0)]$, we thus reproduce property (iv) in Sec. II, which signals the phase transition. It is also worth mentioning that the bulk invariant (22) can

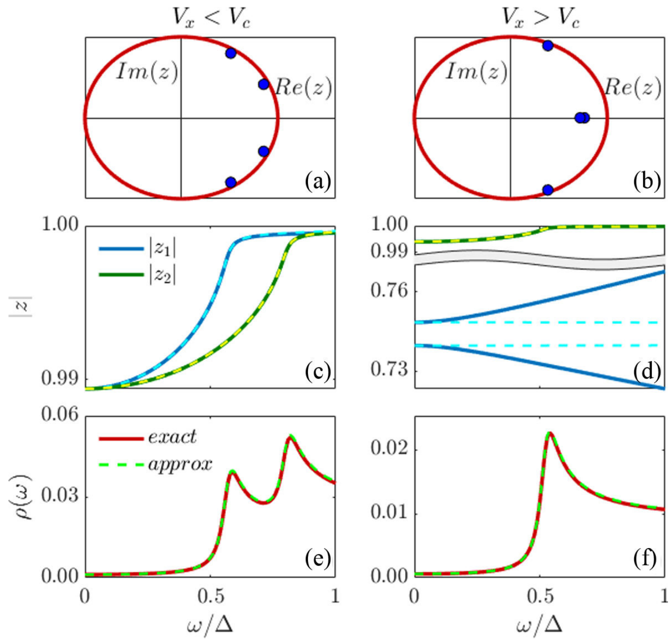

FIG. 2. Behavior of the roots $z_n(\omega)$ for the spinful single-channel Majorana wire model [68,69]. We use $V_x = 0.5V_c$ and $1.2V_c$ as representatives for topologically trivial and nontrivial cases, respectively, with $\mu = 5$ meV and other parameters as specified in the main text. Upper panels: Roots $z_n(\omega = 0)$ (black dots) inside the unit circle (red) for (a) $V_x < V_c$ and (b) $V_x > V_c$. For illustrative purposes, we use $\Delta = 1$ meV in panels (a) and (b). For additional information, see Supplemental Material [73]. Middle panels: Modulus of the roots inside the unit circle vs ω/Δ for (c) $V_x < V_c$ and (d) $V_x > V_c$. Solid curves represent numerically exact results and dashed curves follow from Eqs. (19) and (21), respectively. Bottom panels: Energy dependence of the local bulk DoS, $\rho(\omega)$ (in meV^{-1}), for (e) $V_x < V_c$ and (f) $V_x > V_c$. The solid red curves depict numerically exact results using Eq. (3) and the dashed green curves show approximate results obtained from Eq. (25).

be directly expressed in terms of bGFs for the semi-infinite wire: Using $Q = \det \hat{r}_L = \det \hat{r}_R$ (see Ref. [72]), the reflection matrices $\hat{r}_{L/R}$ and therefore also Q can be obtained from the bGFs [see Eq. (9)].

The knowledge of the roots also gives access to other electronic properties of interest. For instance, we can obtain a compact expression for the energy-dependent local DoS at, say, lattice site $j = 0$ of the translation-invariant chain:

$$\rho(\omega) = -\frac{1}{\pi}\mathrm{Im}\,\mathrm{Tr}[\hat{G}_{00}(\omega)]. \tag{23}$$

We focus on the low-energy limit, where one can expand the cofactor matrix $\hat{A}(z, \omega)$ in Eq. (6) to linear order in ω. The local GF then follows as

$$\hat{G}_{00}(\omega) \simeq \sum_{|z_n|<1} \frac{\hat{A}(z_n, \omega) + \omega\hat{A}'(z_n, \omega)}{\prod_{m\neq n}(z_n - z_m)}, \tag{24}$$

where $\hat{A}'(z_n, \omega) = \frac{d}{d\omega}\hat{A}(z_n(\omega), \omega)$. From our ansatz in Eqs. (19) and (21), the sum in Eq. (24) can be reconstructed. A simple approximate expression follows for small Δ in the low-energy limit, where one needs to keep just the first-order terms $\propto \tau_\nu\sqrt{\Delta_\nu^2 - \omega^2}$ in the denominator. We then obtain

$$\hat{G}_{00}(\omega) \approx \sum_{\nu=1,2} \frac{\hat{A}_\nu + \omega\hat{A}'_\nu}{\sqrt{\Delta_\nu^2 - \omega^2}}, \tag{25}$$

where $\hat{A}_\nu$ and $\hat{A}'_\nu$ are specified in Appendix A. We note that for $V_x > V_c$ the main contribution to Eq. (25) stems from the residues associated to z_2. The results for $\rho(\omega)$ depicted in Figs. 2(e) and 2(f) demonstrate that Eq. (25) accurately reproduces numerically exact calculations, both below and above the topological transition.

Next we turn to the case of a semi-infinite chain in the topological phase, $V_x > V_c$. Using the Dyson equation in Eq. (7) and taking into account the behavior of the roots of the infinite chain discussed above, we can deduce the spatial decay profile of the zero-energy Majorana end state into the bulk. Noting that the GF components $\hat{G}_{j,0}$ and $\hat{G}_{0,j}$ in Eq. (7) are $\propto |z|^j$, we observe that for $V_x > V_c$ the decay is dominated by the z_2 roots since $|z_2| > |z_1|$. Moreover, the decay profile exhibits fast oscillations due to the complex phase δ_2 in Eq. (21), which for $\mu \gg \Delta$ can be approximated as $\delta_2 \simeq k_F a$ with $k_F \equiv k_2$. In this approximation, the local DoS of the $\omega = 0$ MBS thus has the spatial profile

$$\rho_j(\omega = 0) \propto |z_2(0)|^{2j} \cos^2 (jk_F a + \chi_0), \tag{26}$$

where χ_0 describes a phase shift in the $2k_F$ oscillations. Equation (26) reproduces the numerically exact results obtained from Eq. (7) rather well, as illustrated in Fig. 3. The dashed curve shows that the envelope function is accurately described by $|z_2(0)|^{2j}$, corresponding to an exponential decay into the bulk of the chain.

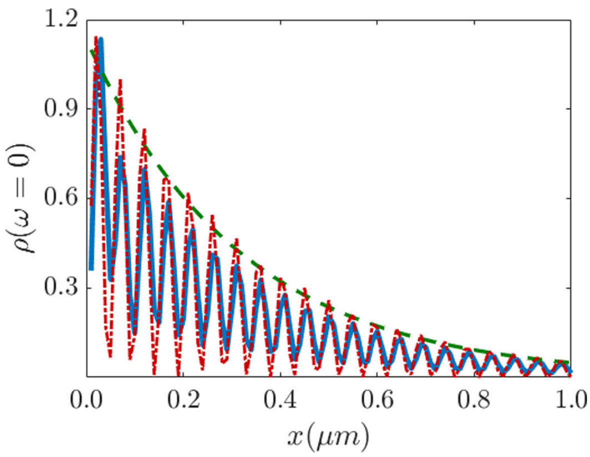

FIG. 3. Spatial variation of the local DoS, $\rho_j(0)$ (in meV^{-1}), vs distance from the boundary, $x = ja$ (in μm), for the $\omega = 0$ Majorana state in a semi-infinite TS wire with $\mu = 1$ meV and $V_x = 2V_c$. The solid blue curve gives numerically exact results obtained from Eq. (7). Red-dotted and green-dashed curves show Eq. (26) with and without $2k_F$ oscillations, respectively.

IV. TWO-CHANNEL CLASS-D NANOWIRE

We next examine the case of spinful multichannel hybrid nanowires with broken time-reversal symmetry. The bGF approach could in principle be applied to nanowire models

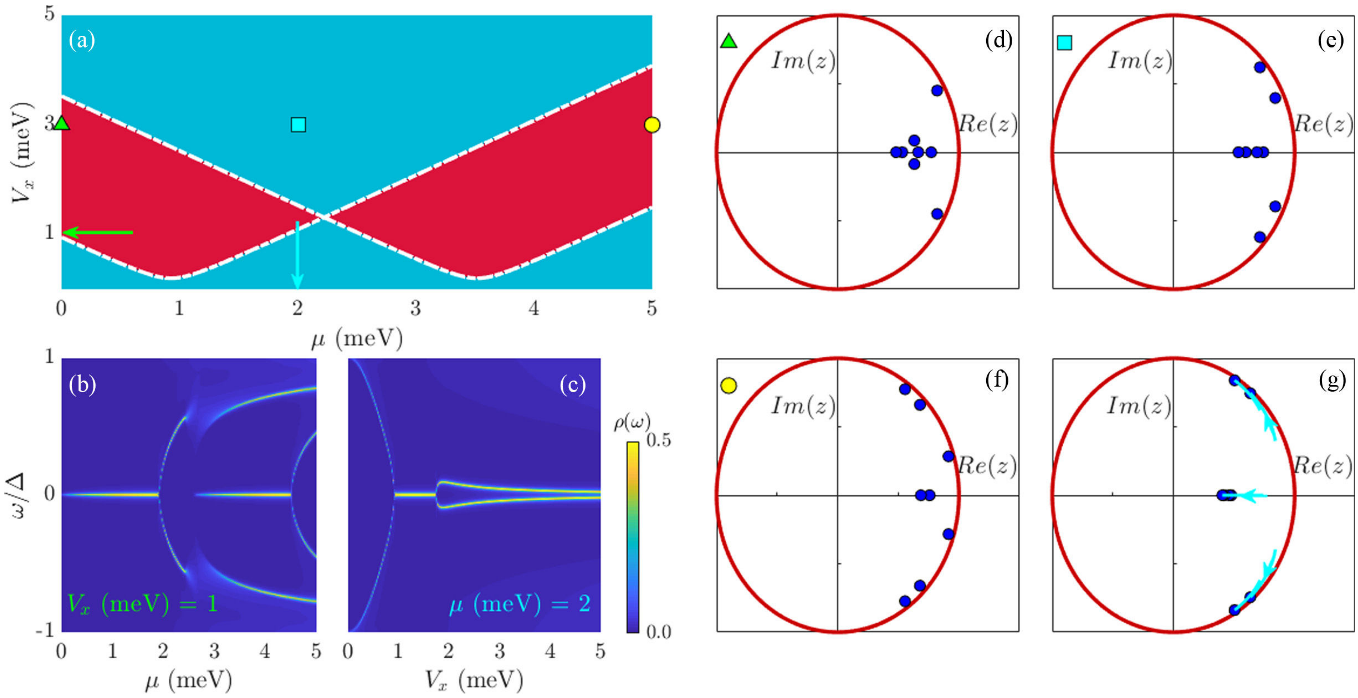

FIG. 4. Two-channel spinful Majorana wire model of class D [see Eq. (27)] with parameters as explained in the main text. Panel (a) shows the bulk phase diagram in the μ-V_x plane. Topological nontrivial (trivial) phases are shown in red (blue). Panels (b) and (c) show the energy dependence of the local DoS, $\rho_{j=1}(\omega)$ (in meV^{-1}), at the boundary of a semi-infinite two-channel wire along the trajectories marked by arrows in panel (a). Panels (d)–(f) illustrate the roots $z_n(0)$ inside the unit circle at the three points indicated in panel (a) by a triangle (d), a square (e), and a circle (f), respectively. For additional insights, see Supplemental Material [73]. Panel (g) shows the evolution of the roots within the topologically trivial regime as V_x increases from 3 to 8 meV at constant chemical potential $\mu = 2$ meV. In panels (d)–(g), we use $\Delta = 1$ meV.

with an arbitrary number of channels. In practice, however, the techniques in Sec. II are less efficient once the degree $2N$ of the secular polynomial (5) becomes very large. We here restrict ourselves to the two-channel case with $N = 8$, which can be realized for two single-channel nanowires coupled by tunneling terms. The resulting model already exhibits many of the features expected for generic multichannel nanowires [74,75].

Our model Hamiltonian is given by

$$\hat{\mathcal{H}}_{2\text{ch}}(k) = \begin{pmatrix} \hat{\mathcal{H}}(k) & \hat{T} \\ \hat{T}^\dagger & \hat{\mathcal{H}}(k) \end{pmatrix}, \tag{27}$$

where the 2×2 structure refers to wire space. We consider two identical spinful single-channel Majorana wires described by the model of Refs. [68,69] with $\hat{\mathcal{H}}(k)$ in Eq. (10). The interwire tunnel couplings are modeled by

$$\hat{T} = -t_y\sigma_0\tau_z + i\alpha_y\sigma_x\tau_z + \Delta_y\sigma_0\tau_x, \tag{28}$$

where t_y and α_y are spin-conserving and spin-flipping hopping amplitudes, respectively. The coupling α_y may arise due to the presence of a Rashba spin-orbit coupling produced by an electric field along the z direction. As in Sec. III, we write $t_y = \hbar^2/(2m^* a_y^2)$ and $\alpha_y = \hbar u/a_y$, with the minimal distance a_y between the wires. In the concrete examples shown below, we assume $a_y = 3a$, which corresponds to a subband separation of ≈ 3 meV. The interwire coupling (28) also includes a nonlocal interwire pairing amplitude Δ_y. For the present class-D case, however, we find that allowing for a small $\Delta_y \neq 0$ does not lead to significant changes in the phase diagram. We thus put $\Delta_y = 0$ in this section.

One can characterize the phase diagram of a translationally invariant two-channel wire by using the bulk topological invariant in Eq. (22) with the replacement $\hat{\mathcal{H}}(k) \to \hat{\mathcal{H}}_{2\text{ch}}(k)$. The Pfaffian at $k = 0$ is here given by

$$\begin{aligned} \text{Pf}\,\hat{\mathcal{H}}_{2\text{ch}}(0) = \alpha_y^4 &+ \left[(\mu - 3t_y)^2 - V_x^2 + \Delta^2\right] \\ &\times \left[(\mu - t_y)^2 - V_x^2 + \Delta^2\right] \\ &+ 2\alpha_y^2\left[-(\mu - 3t_y)(\mu - t_y) - V_x^2 + \Delta^2\right]. \end{aligned} \tag{29}$$

The boundaries of the topological phase correspond to a vanishing Pfaffian at $k = 0$, where Eq. (29) implies the two critical Zeeman fields

$$\begin{aligned} V_{c,\pm} = \big(\alpha_y^2 + \mu^2 - 4\mu t_y + 5t_y^2 + \Delta^2 + \\ \pm 2|\mu - 2t_y|\sqrt{t_y^2 + \alpha_y^2}\big)^{1/2}. \end{aligned} \tag{30}$$

The resulting phase diagram in the μ-V_x plane is illustrated in Fig. 4(a). We observe that the two-channel model (27) exhibits a richer phase diagram than in the single-channel case (see also Refs. [74,75]).

We next construct the bGF of a semi-infinite wire by determining the roots of the secular polynomial in Eq. (5), which here is a 16th-order polynomial equation that we solve numerically. Figures 4(b) and 4(c) illustrate the evolution of the energy-dependent local DoS, $\rho_1(\omega)$, at the boundary, i.e., taken at site $j = 1$ of a semi-infinite two-channel wire. We consider two different trajectories in the μ-V_x plane as indicated by the arrows in Fig. 4(a). For constant V_x [panel (b)], there are both topologically nontrivial and trivial regions as μ is varied. In the topologically nontrivial regions, we observe a zero-energy peak in the local DoS, signaling the presence of MBSs. This $\omega = 0$ peak is absent in the trivial regime. For fixed μ [panel (c)], the topologically nontrivial phase is reached for intermediate values of V_x. For larger V_x, even though the system is in a trivial phase, we find low-energy Andreev bound states that approach zero energy as V_x increases. This effect has also been described in Ref. [75].

Additional insights follow by analyzing the evolution of the roots $z_n(\omega = 0)$ inside the unit circle in the complex momentum plane. In Figs. 4(d)–4(f), we illustrate their distribution for three different points in the phase diagram. For panels (d) and (f), the system is in a topological phase and, as expected, one finds an *odd* number of pairs of complex conjugate roots close to the unit circle. As in Sec. III, the roots on the real axis correspond to additional bands at higher energies well above Δ. Panel (e) instead corresponds to a topologically trivial phase with an *even* number of conjugate root pairs near the unit circle. Finally, Fig. 4(g) illustrates the evolution of the roots in the topologically trivial regime as the Zeeman parameter V_x increases. We find that both roots near the unit circle in the first quadrant become almost degenerate for large V_x. Such a behavior effectively amounts to having two replicas of a single-channel TS wire, which in turn helps to explain why Andreev bound states approach the zero-energy limit for the strong Zeeman field [see Fig. 4(c) and Ref. [75]].

V. TRITOPS NANOWIRES

Next we turn to models for hybrid nanowires of symmetry class DIII. Such TRITOPS wires constitute another interesting system with topologically nontrivial phases. Below we first study single-channel wires and subsequently turn to the two-channel case.

A. Single-channel case

Many different proposals for physical realizations of single-channel TRITOPS wires have been put forward in the recent past [18–35]. For concreteness, we will here focus on the model introduced by Zhang *et al.* [21]. Using the spin-Nambu basis with $N = 4$ in Sec. II, the Hamiltonian is given by

$$\hat{\mathcal{H}}_{\mathrm{DIII}}(k) = \epsilon_k \sigma_0 \tau_z + \alpha_k \sigma_z \tau_z + \Delta_k \sigma_0 \tau_x, \tag{31}$$

where in this section we use

$$\begin{aligned} \epsilon_k &= -2t\cos(ka) - \mu, \quad \alpha_k = 2\alpha\sin(ka), \\ \Delta_k &= 2\Delta\cos(ka). \end{aligned} \tag{32}$$

Again t corresponds to a nearest-neighbor hopping amplitude, μ is the chemical potential, a is the lattice spacing, and α is the spin-orbit coupling strength. The parameter Δ corresponds to a nearest-neighbor pairing interaction. In the examples below, we use $a = 10$ nm, $t = 10$ meV, and $\alpha = 4$ meV as in Secs. III and IV.

By a simple rearrangement of the spin-Nambu spinor $\hat{\Psi}_k$, one can block diagonalize the Hamiltonian in Eq. (31), $\hat{\mathcal{H}}_{\mathrm{DIII}} = \mathrm{diag}(\hat{\mathcal{H}}_-, \hat{\mathcal{H}}_+)$. To that end, upon replacing $\hat{\Psi}_k^T \to (c_{k\uparrow}, c_{-k\downarrow}^\dagger, c_{k\downarrow}, -c_{-k\uparrow}^\dagger)$, we arrive at the 2×2 block Hamiltonians

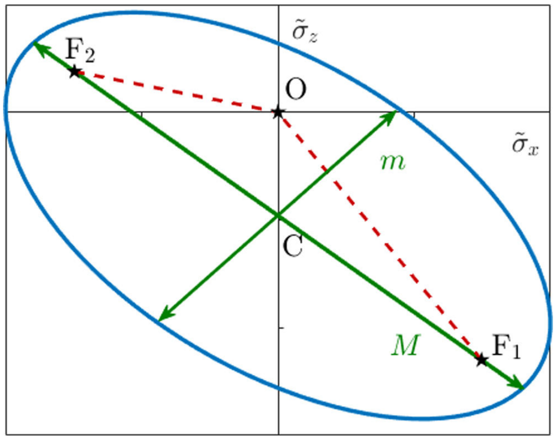

FIG. 5. Curve traced out by $\beta_-(k)$ in the $\tilde{\sigma}_x$-$\tilde{\sigma}_z$ plane for a single-channel TRITOPS wire in a topologically nontrivial phase [see Eqs. (33) and (34)] with $t = 0.5$, $\alpha = 0.8$, $\Delta = 1$, and $\mu = 1.04$ (all in meV). The evolution of the bulk Hamiltonian $\hat{\mathcal{H}}_-(k)$ upon traversal of the Brillouin zone is described by an ellipse containing the origin (O). For details, see main text and Appendix B.

$$\hat{\mathcal{H}}_\pm(k) = (\epsilon_k \mp \alpha_k)\tilde{\sigma}_z + \Delta_k \tilde{\sigma}_x = \beta_\pm(k)\cdot\tilde{\sigma}, \tag{33}$$

where $\tilde{\sigma}$ is the vector of $\tilde{\sigma}_{x,y,z}$ Pauli matrices in the respective 2×2 space obtained after block diagonalization. Each Hamiltonian $\hat{\mathcal{H}}_\pm(k)$ corresponds to a Dirac-type model where

$$\beta_\pm(k) = \begin{pmatrix} 2\Delta\cos(ka) \\ 0 \\ -\mu - 2t\cos(ka) \pm 2\alpha\sin(ka) \end{pmatrix} \tag{34}$$

is a vector field mapping the first Brillouin zone onto a closed curve.

At this stage, we can apply the formalism of Ref. [76] for analyzing the roots of the secular polynomial of Dirac-like Hamiltonians. By projecting $\hat{\mathcal{H}}_\pm$ to the $\tilde{\sigma}_x$-$\tilde{\sigma}_z$ plane, we obtain an elliptic curve as illustrated in Fig. 5. According to the arguments in Ref. [76], if the ellipse encloses the origin of the $\tilde{\sigma}_x$-$\tilde{\sigma}_z$ plane, we know that for a semi-infinite wire $\hat{\mathcal{H}}_\pm(k)$ will generate an edge state with energy equal to the modulus of the component of $\beta_\pm(k)$ perpendicular to this plane. In our case, $[\beta_\pm(k)]_y = 0$ implies that we have a pair of zero-energy boundary states in the topological phase. In addition, this argument also shows that there are no finite-energy Andreev bound states in the trivial phase (where the ellipse does not contain the origin). For the case in Fig. 5, where the origin is displaced along the $\tilde{\sigma}_z$ axis, the topological transition occurs at $ka = \pm\pi/2$ and $|\mu| = 2\alpha$ [see Eq. (34)]. This conclusion is consistent with the fact that at the topological transition one finds roots at $z = e^{ika} = \pm i$ (see also Ref. [77]), in agreement with property (v) in Sec. II.

More generally, by determining the roots $z_n(\omega)$, we can again construct the bGF of a semi-infinite wire. In particular, we thereby obtain the class-DIII bulk topological invariant via the reflection matrices in Eq. (9). In the present case, the invariant is given by $Q = \mathrm{Pf}(i\hat{r}_{L,R})$ [72]. Furthermore, using the results of Refs. [76,77], an analytical expression for the

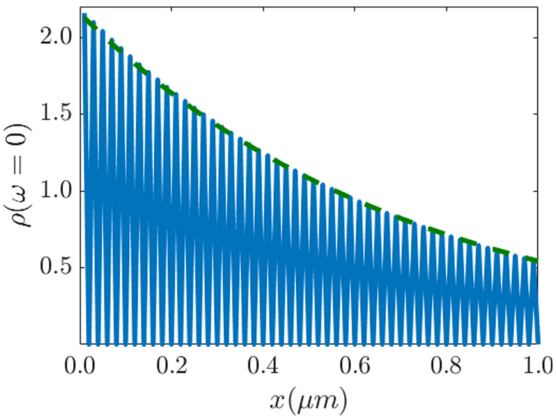

FIG. 6. Spatial variation of the local DoS at zero energy (in meV^{-1}), corresponding to Majorana end states of a semi-infinite TRITOPS wire in its topological phase [see Eq. (31)] for $\mu = 0$ (blue solid curve). The green dashed curve shows an exponential decay on the length scale $\lambda_e = -\frac{a}{2}\ln|z_{\max}|$ [see Eq. (B6)].

largest-modulus zero-frequency root, $z_{\max}$, inside the unit circle can be computed from purely geometrical considerations for the ellipse in Fig. 5 (see Appendix B for details). The length scale governing the spatial decay profile of the pair of Majorana states localized near the boundary of a semi-infinite TRITOPS wire then follows as $\lambda_e = -\frac{a}{2}\ln|z_{\max}|$ [see Eq. (B6) in Appendix B]. The validity of this expression is confirmed in Fig. 6, where we show numerically exact results for the spatial variation of the local DoS at $\omega = 0$ together with the prediction obtained from Eq. (B6).

B. Two-channel case

As in Sec. IV, we can also extend the TRITOPS model to the two-channel case by coupling two single-channel wires. More general multichannel wire constructions are also possible but will not be pursued here. The corresponding Hamiltonian is with Eq. (31) given by

$$\hat{\mathcal{H}}_{\mathrm{DIII,2ch}}(k) = \begin{pmatrix} \hat{\mathcal{H}}_{\mathrm{DIII}}(k) & \hat{T}_{\mathrm{DIII}} \\ \hat{T}^{\dagger}_{\mathrm{DIII}} & \hat{\mathcal{H}}_{\mathrm{DIII}}(k) \end{pmatrix}, \tag{35}$$

where the interwire tunneling couplings are modeled in a similar manner as in Eq. (28):

$$\hat{T}_{\mathrm{DIII}} = -t_y\sigma_0\tau_z + i\alpha_y\sigma_y\tau_z + \Delta_y\sigma_0\tau_z. \tag{36}$$

We here allow for spin-conserving (t_y) and spin-flipping (α_y) hopping processes, as well as for nonlocal pairing terms (Δ_y). Below, t_y and α_y are parametrized as specified in Sec. IV.

The resulting phase diagram is illustrated in Fig. 7(a). To make analytical progress, from now on we consider the case $\Delta_y = 0$ and determine the conditions for gap closings, and thus for phase transition curves in the two-channel TRITOPS case. The gap closes again for $ka = \pm\pi/2$ as in Sec. V A but now for the chemical potential set to one of the critical values

$$|\mu_\pm| = \sqrt{\alpha_y^2 + (t_y \pm 2\alpha)^2}. \tag{37}$$

where the topological invariant is related to the product of the signs of the effective pairing amplitude at different Fermi

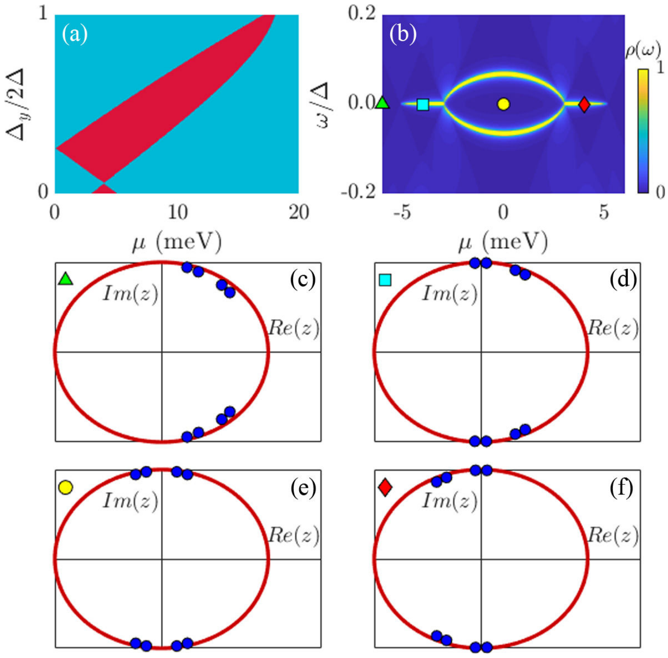

FIG. 7. Two-channel TRITOPS nanowire [see Eq. (35)], with parameters as explained in the main text. Panel (a) shows the phase diagram in the μ-Δ_y plane, with the topologically nontrivial (trivial) phase in red (blue). (b) Local DoS, $\rho_{j=1}(\omega)$ (in meV^{-1}), at the boundary of a semi-infinite wire in the μ-ω plane for $\Delta_y = 0$. Panels (c) to (f) depict the roots $z_n(\omega = 0)$ inside the unit circle for different μ as indicated by the respective symbol in panel (b). We use $\Delta = 1$ meV in panels (c)–(f).

points [66]. As the critical momenta are as in Sec. V A, the pairing function is directly determined by $\Delta\cos(ka)$ [see Eq. (31)]. For this reason, the topologically nontrivial (trivial) phase has an odd (even) number of Fermi points between $ka = 0$ and $\pi/2$.

The bGF can again be computed from the roots of the secular polynomial. The latter also determine the behavior of the edge modes of a semi-infinite two-channel TRITOPS wire in different regions of the phase diagram. By continuity, the condition of having an odd number of Fermi points with $0 < k_F < \pi/2a$ corresponds to an odd number N_p of roots near the unit circle in the first quadrant. Our results for the roots are illustrated in Figs. 7(c)–7(f). As expected, N_p is odd for panels (d) and (f), where panel (b) shows that Majorana end states are present and thus a topological phase is realized. By contrast, panels (c) and (e) show topologically trivial cases with even N_p.

VI. PHASE-BIASED TOPOLOGICAL JOSEPHSON JUNCTIONS

In this section, we consider different examples for the equilibrium supercurrent-phase relation in two- and three-terminal Josephson junctions made of nanowires in topologically nontrivial superconducting phases. These wires are coupled together by tunnel junctions. We start in Sec. VI A with the case of a trijunction of TS nanowires (see also Ref. [61]) and then turn to TRITOPS-TS Josephson junctions in Sec. VI B.

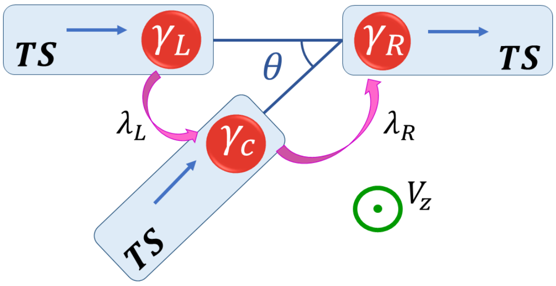

FIG. 8. Three-terminal junction of spinful TS nanowires (see Sec. III), with two parallel wires (L, R) and a central (C) wire at angle θ. The red dots indicate MBSs with Majorana operators $\gamma_{L,R,C}$ near the junction, with tunnel couplings $\lambda_{L,R}$ connecting the L and R wires to the C wire. We assume that no direct tunnel coupling between the L and R wires is present. A Zeeman field V_z is applied perpendicular to the plane containing the three wires. Blue arrows show the positive momentum direction in each wire.

A. Three-terminal TS junctions

We first consider a three-terminal junction formed by spinful single-channel nanowires in the TS phase. For a schematic layout, see Fig. 8. Such devices have been suggested, e.g., for Majorana braiding implementations [78–80], for the engineering of artificial topological Weyl semimetal phases [81,82], and for the observation of giant shot-noise features induced by the single zero-energy MBS localized at the trijunction [83]. While most previous studies have been based on minimal models or on spinless Kitaev chain models, a more realistic description using the spinful nanowire model of Refs. [68,69] discussed in Sec. III is desirable. In particular, one can then assess the role of the spin degree of freedom and the effects of various microscopic parameters such as the angle θ in Fig. 8. We assume that each wire is sufficiently long such that the overlap between MBSs located at different ends of the same wire is negligibly small.

We model each nanowire in the setup of Fig. 8 in terms of the spinful single-channel Hamiltonian of Eq. (10). All three wires lie in a plane, with two of them aligned (L and R in Fig. 8) and the third (the central wire, C, in Fig. 8) at an arbitrary angle θ to the other two. We here assume that the Zeeman field V_z is oriented perpendicular to the plane (see Ref. [1]). For simplicity, we consider identical material parameters for the three wires which are chosen such that the TS phase is realized.

Let us next discuss the unitary rotations necessary to adapt the bGFs of Sec. III to a common reference frame for all three wires in Fig. 8. We first perform a $\pi/2$ rotation of the spin axis around the y axis, which connects the intrinsic coordinate system of the L and R wires to the common reference frame. Defining

$$R(\vartheta) = [\sigma_0 \cos(\vartheta/2) - i\sigma_y \sin(\vartheta/2)]\tau_0, \tag{38}$$

the corresponding rotation matrix, $R_y = R(\vartheta = \pi/2)$, transforms a Zeeman field along the x direction (see Sec. III) into a Zeeman field along the negative z direction (as in Fig. 8). The bGFs for the L and R wires in Fig. 8 are thus given by

$$\hat{\mathcal{G}}'_{L/R} = R_y \hat{\mathcal{G}}_{L,R} R_y^{-1}, \tag{39}$$

with $\hat{\mathcal{G}}_{L,R}$ as described in Sec. III. For the C lead, we additionally have to rotate by the angle θ around the global z axis. The corresponding rotation matrix, $R_z(\theta)$, follows from Eq. (38) with the replacements $\sigma_y \to \sigma_z$ and $\vartheta \to \theta$. We thereby obtain

$$\hat{\mathcal{G}}_C = R_z(\theta) R_y \hat{\mathcal{G}}_L R_y^{-1} R_z^{-1}(\theta). \tag{40}$$

In what follows, we rewrite $\hat{\mathcal{G}}'_{L/R} \to \hat{\mathcal{G}}_{L/R}$ to keep the notation simple.

The coupling between the L and R wires and the C wire is modeled by a spin-conserving tunneling term,

$$H_T = \frac{1}{2} \sum_{\nu=L,R} \hat{\Psi}_\nu^\dagger \hat{\lambda}_\nu \hat{\Psi}_C + \text{H.c.}, \quad \hat{\lambda}_\nu = \lambda_\nu \sigma_0 \tau_z e^{i\tau_z \phi_\nu/2}, \tag{41}$$

where $\hat{\Psi}_{L,R,C}$ are boundary spinor fields and ϕ_ν is the phase of the superconducting order parameter in the respective wire. We choose a gauge with $\phi_C = 0$ and real-valued tunnel couplings λ_ν. The physical properties of the trijunction are then determined by the full bGF,

$$\hat{\mathcal{G}}_{3\mathrm{TS}} = \begin{pmatrix} \hat{\mathcal{G}}_L^{-1} & \hat{\lambda}_L & 0 \\ \hat{\lambda}_L^\dagger & \hat{\mathcal{G}}_C^{-1} & \hat{\lambda}_R \\ 0 & \hat{\lambda}_R^\dagger & \hat{\mathcal{G}}_R^{-1} \end{pmatrix}^{-1}, \tag{42}$$

where the 3×3 structure refers to wire space. From Eq. (42), the energy dependence of the local DoS at the junction will be given by

$$\rho_{3\mathrm{TS}}(\omega) = -\frac{1}{\pi} \mathrm{Im}\,\mathrm{Tr}[\hat{\mathcal{G}}_{3\mathrm{TS}}(\omega)]. \tag{43}$$

Figure 9 shows the phase dependence of $\rho_{3\mathrm{TS}}(\omega)$ obtained by numerical evaluation of Eqs. (42) and (43) for a trijunction with $\phi_L = -\phi_R = \phi$ and $\phi_C = 0$. (This is the series configuration in the parlance of Ref. [61].)

Deep in the topological regime, the low-energy properties of the trijunction are well described by a minimal model keeping only the MBSs at the junction. To show this from the above bGFs, we first derive an effective Hamiltonian for each wire that only keeps track of the respective MBS:

$$H_{\mathrm{eff},\nu} = \lim_{\omega \to 0} \hat{\mathcal{G}}_\nu^{-1}(\omega). \tag{44}$$

Using Eq. (44) and recalling that the z_2 roots dominate for $V_x > V_c$, we can read off the boundary spinors for each of the wires ($\nu = L, R, C$; see Ref. [61]):

$$\hat{\Psi}_L \simeq \sqrt{\frac{\Delta_2}{t}} \begin{pmatrix} 0 \\ 1 \\ -i \\ 0 \end{pmatrix} \gamma_L, \quad \hat{\Psi}_R \simeq \sqrt{\frac{\Delta_2}{t}} \begin{pmatrix} 0 \\ -i \\ 1 \\ 0 \end{pmatrix} \gamma_R,$$

$$\hat{\Psi}_C \simeq \sqrt{\frac{\Delta_2}{t}} R_z(\theta) \begin{pmatrix} 0 \\ 1 \\ -i \\ 0 \end{pmatrix} \gamma_C, \tag{45}$$

where the Majorana operators γ_ν satisfy the anticommutation relations $\{\gamma_\nu, \gamma_{\nu'}\} = \delta_{\nu\nu'}$. The pairing gap Δ_2 has been defined in Sec. III [see also Fig. 1 and Eq. (20)].

Next, we project the tunneling Hamiltonian (41) to the Majorana sector by means of Eq. (45). We thereby arrive at

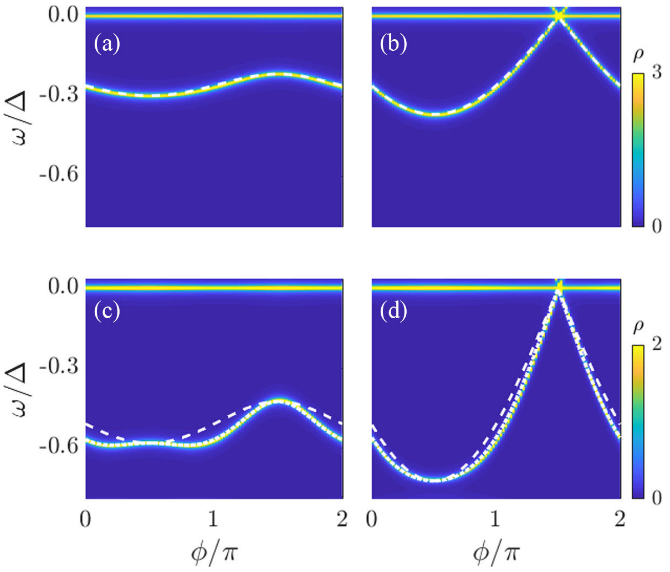

FIG. 9. Phase dependence of the subgap spectrum of the trijunction of TS wires in Fig. 8, with the superconducting phases $\phi_L = -\phi_R = \phi$ and $\phi_C = 0$. The TS wires are modeled as spinful nanowires with $\mu = 2$ meV, $V_z = 3V_c$, and symmetric couplings, $\lambda_L = \lambda_R = \lambda$. For other parameters, see Sec. III. Panel (a) [(b)] is for $\lambda = 2$ meV and $\theta = \pi/2$ [$\theta = \pi/10$]. Panel (c) [(d)] is for $\lambda = 5$ meV and $\theta = \pi/2$ [$\theta = \pi/10$]. From blue to yellow, $\rho_{3\mathrm{TS}}(\omega)$ (in meV^{-1}) gradually increases, where Eq. (43) has been evaluated in a numerically exact manner. White dotted [dashed] curves show the approximate Andreev bound state dispersion relation in Eq. (54) [Eq. (51)].

a minimal model Hamiltonian,

$$H_{\mathrm{mm}} = -i\Omega_L(\phi)\gamma_L\gamma_C - i\Omega_R(\phi)\gamma_R\gamma_C, \tag{46}$$

with the energies

$$\Omega_L(\phi) = \frac{2\Delta_2\lambda_L}{t}\sin\left(\frac{\phi+\theta}{2}\right),$$
$$\Omega_R(\phi) = -\frac{2\Delta_2\lambda_R}{t}\cos\left(\frac{\phi-\theta}{2}\right). \tag{47}$$

Equation (46) is easily diagonalized by rotating the $\gamma_{L,R}$ operators to new Majorana operators $\tilde{\gamma}_{L,R}$,

$$\begin{pmatrix}\gamma_L\\ \gamma_R\end{pmatrix} = \begin{pmatrix}\sin\kappa & -\cos\kappa\\ \cos\kappa & \sin\kappa\end{pmatrix}\begin{pmatrix}\tilde{\gamma}_L\\ \tilde{\gamma}_R\end{pmatrix}, \tag{48}$$

with $\sin\kappa = \Omega_L/\Omega$ and

$$\Omega(\phi) = \sqrt{\Omega_L^2(\phi) + \Omega_R^2(\phi)}. \tag{49}$$

We thereby arrive at

$$H_{\mathrm{mm}} = -i\Omega(\phi)\tilde{\gamma}_L\gamma_C, \tag{50}$$

where the decoupled Majorana operator $\tilde{\gamma}_R$ describes the remaining zero-energy state [83]. The eigenstates of Eq. (50) correspond to Andreev bound states with the phase-dependent subgap energy [see Eq. (47)]:

$$E_\pm(\phi) = \pm\tfrac{1}{2}\sqrt{\Omega_L^2(\phi) + \Omega_R^2(\phi)}. \tag{51}$$

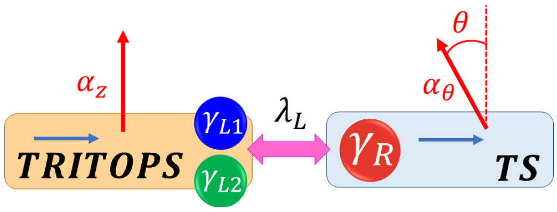

FIG. 10. Sketch of a TRITOPS-TS Josephson junction. Colored dots indicate MBSs corresponding to the Majorana operators $\gamma_{L1,L2,R}$. The tunnel coupling λ_L connects both wires, where blue arrows shows the positive momentum direction in each wire. The spin-orbit axes on both sides are tilted by the relative angle θ.

The phase derivative $\partial_\phi E_-(\phi)$ then yields the Josephson current-phase relation. As illustrated in Fig. 9, Eq. (51) reproduces our numerically exact bGF calculations for small tunnel couplings $\lambda_{L,R}$.

However, for intermediate-to-large values of the tunnel couplings, the Andreev bound-state dispersion may deviate from Eq. (51) [see, e.g., the "bump"-like features in Fig. 9(c)]. Such deviations are due to the fact that the Majorana operators γ_L and γ_R will become connected through the virtual excitation of continuum quasiparticle states with above-gap energy $E > \Delta$. Within our minimal model, this physics can be taken into account by adding an effective coupling λ_{LR} between the L and R wires. For $\lambda_\nu \ll \Delta$, we estimate $\lambda_{LR} \simeq \lambda_L\lambda_R/\Delta$. The corresponding tunneling term is given by

$$H_{T,LR} = \tfrac{1}{2}\lambda_{LR}\hat{\Psi}_L^\dagger\sigma_0 e^{i\tau_z\phi}\tau_z\hat{\Psi}_R + \mathrm{H.c.} \tag{52}$$

Using the Majorana spinors in Eq. (45) together with Eq. (46), we arrive at an improved version of the minimal model Hamiltonian:

$$H_{\mathrm{mm}} = -i\Omega_L(\phi)\gamma_L\gamma_C - i\Omega_R(\phi)\gamma_R\gamma_C - i\Omega_{LR}(\phi)\gamma_L\gamma_R,$$
$$\Omega_{LR}(\phi) = \frac{2\Delta_2\lambda_{LR}}{t}\cos\phi. \tag{53}$$

One can easily show that Eq. (53) still predicts a decoupled zero-energy MBS at the trijunction. The hybridization between the remaining two Majorana states yields Andreev bound states with the dispersion relation

$$E_\pm(\phi) = \pm\tfrac{1}{2}\sqrt{\Omega_L^2(\phi) + \Omega_R^2(\phi) + \Omega_{LR}^2(\phi)}. \tag{54}$$

Of course, for $\lambda_{LR} \to 0$, we recover Eq. (51). Only by including the Ω_{LR} term in Eq. (54), however, the bumps found in the numerically exact dispersion in Fig. 9(c) can be accurately reproduced.

We conclude that the minimal model in Eq. (53), which has been derived from the bGF approach, captures the basic physics of the Josephson effect in the three-terminal TS junction shown in Fig. 8. In particular, the dependence of the current-phase relation on the angle θ between the wires resulting from the subgap spectrum in Fig. 8 will be correctly reproduced.

B. TRITOPS-TS junction

We next consider the two-terminal Josephson junction in Fig. 10 between a TRITOPS wire [see Eq. (33) in Sec. V A] and a TS nanowire [see Eq. (10) in Sec. III]. Denoting the respective boundary spin-Nambu spinors by $\hat{\Psi}_L$ and $\hat{\Psi}_R$, respectively, the tunneling Hamiltonian is given by

$$H_T = \tfrac{1}{2}\lambda_L \hat{\Psi}_L^\dagger\, \sigma_0 e^{i\tau_z\phi/2}\tau_z \hat{\Psi}_R + \text{H.c.}, \tag{55}$$

where ϕ is the superconducting phase difference across the junction and we assume a real-valued tunnel coupling λ_L. Below we assume for simplicity that the pairing gap Δ is identical for both nanowires. We will allow for a relative angle θ between the directions of the spin-orbit field in each wire (see the schematic device layout in Fig. 10). One could vary θ by changing the orientation of a local electric field applied to the TS wire only, which in turn will affect the corresponding Rashba spin-orbit field. In addition, we need a Zeeman field to induce the topological phase in the TS nanowire (see Sec. III), while no Zeeman field should be present on the time-reversal invariant TRITOPS side. To achieve this goal, one may use mesoscopic ferromagnets for inducing a Zeeman field only locally [84].

To account for the angle θ, we then apply the unitary transformation $R_y(\theta)$ to the bGF describing the TS nanowire. This rotation simultaneously affects the spin-orbit and the Zeeman field directions in the TS wire such that both directions can never be parallel to each other. The junction spectral properties then follow again from a Dyson equation as in Eq. (41). Assuming that both wires have model parameters putting them deeply into the respective topological regime, we can compare our numerically exact results for the subgap spectral properties to the corresponding predictions of a minimal model Hamiltonian. The latter is obtained by retaining only the MBS degrees of freedom indicated in Fig. 10. To that end, the approximate expression for the boundary spinors can again be derived from the respective bGFs as in Sec. VI A. Those spinors involve the Majorana operators $\gamma_{L1,L2,R}$ in Fig. 10 and are given by

$$\hat{\Psi}_L \simeq \sqrt{\frac{\Delta}{t}}\begin{pmatrix}1\\0\\i\\0\end{pmatrix}\gamma_{L1} + \sqrt{\frac{\Delta}{t}}\begin{pmatrix}0\\i\\0\\1\end{pmatrix}\gamma_{L2},$$

$$\hat{\Psi}_R \simeq \sqrt{\frac{\Delta_2}{t}}R_y(\theta)\begin{pmatrix}i\\-i\\1\\1\end{pmatrix}\gamma_R. \tag{56}$$

The resulting minimal model Hamiltonian is

$$H_{\min} = -i[w_1(\phi)\gamma_{L1} + w_2(\phi)\gamma_{L2}]\gamma_R \tag{57}$$

with the energies

$$w_1(\phi) = \frac{2\lambda_L\sqrt{\Delta\Delta_2}}{t}\cos\frac{\phi}{2}\cos\frac{\theta}{2},$$

$$w_2(\phi) = -\frac{2\lambda_L\sqrt{\Delta\Delta_2}}{t}\sin\frac{\phi}{2}\sin\frac{\theta}{2}. \tag{58}$$

The structure of H_{mm} in Eq. (57) is similar to the minimal model (46) for the TS trijunction in Sec. VI A without any coupling between the $\gamma_{L1,L2}$ operators. The subgap spectrum is therefore characterized by a decoupled zero-energy Majorana state, and the hybridization of the two other Majorana operators yields the Andreev bound-state dispersion:

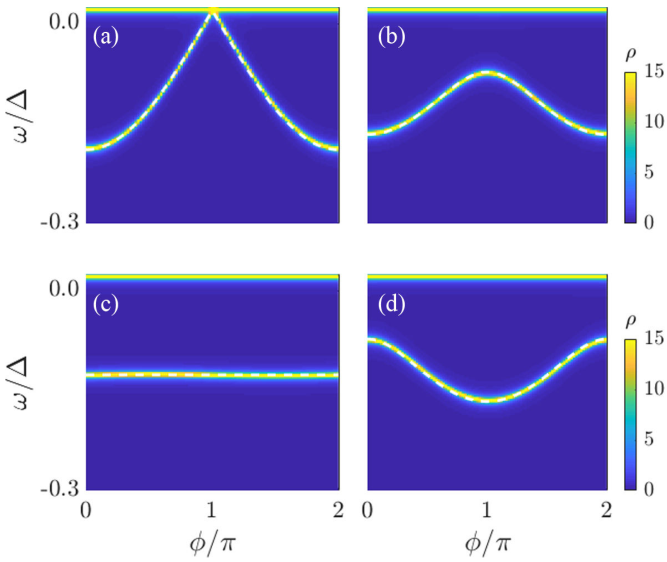

FIG. 11. Phase-dependent subgap spectrum of a TRITOPS-TS Josephson junction for different values of the tilt angle θ in Fig. 10. The spinful single-channel model parameters are as described in Secs. III and V, with $\mu = 1$ meV, $\lambda_L = 2$ meV, and $V_x = 1.5V_c$ on the TS side. The tilt angle is $\theta = 0$ in panel (a), $\theta = 0.3\pi$ in panel (b), $\theta = \pi/2$ in panel (c), and $\theta = 0.7\pi$ in panel (d). From blue to yellow, the color code indicates increasing DoS values at the junction, $\rho(\omega)$ (in meV^{-1}). White dashed curves show the Andreev bound states (59).

$$E_\pm(\phi) = \pm\tfrac{1}{2}\sqrt{w_1^2(\phi) + w_2^2(\phi)}. \tag{59}$$

We compare Eq. (59) to numerically exact results for the subgap spectral properties of the TRITOPS-TS junction in Fig. 11. Clearly, the general subgap spectrum is rather well described by the minimal model (57). In contrast to the case of a triterminal TS junction, for TRITOPS-TS junctions it is not necessary to take into account higher-order tunneling processes for obtaining accurate agreement with numerically exact bGF calculations (but see Ref. [85]).

VII. CONCLUDING REMARKS

In the present paper, we have generalized the boundary Green's-function approach of Refs. [59,61] to quasi-1D spinful models of Majorana nanowires. For single-channel class-D and class-DIII wire models, we have obtained an analytical understanding of the behavior of the roots of the corresponding secular polynomial in complex momentum space. This advance helps physical intuition and allows for a practical and numerically efficient method for computing the bGF, and thereby also physical observables. The method has also been extended to spinful multichannel models, where it appears to allow for more efficient numerical bGF calculations than the alternative recursive technique [60,77]. Let us remark that the computational complexity of the method is only limited by the ability to evaluate the roots of a polynomial. Typically, the numerical demands are therefore much smaller than those for a recursive calculation of the bGF.

Given the efficient construction of the bGF put forward in this paper, one can now apply the general bGF approach [59] to study the transport properties of many different hybrid devices composed of Majorana nanowires and/or conventional metals or superconductor electrodes. In Sec. VI, we have provided two examples for such devices, namely, phase-biased trijunctions of TS wires and TRITOPS-TS junctions. In both cases, we have carried out an analysis of the subgap Andreev (or Majorana) state dispersion at zero temperature.

We believe that this approach offers many interesting perspectives for future research. In particular, one can study nonequilibrium transport properties away from the linear-response regime, and one can also include electron-electron or electron-phonon effects, at least on a perturbative level. We are confident that the results of our paper can also be helpful for the interpretation of transport experiments carried out on hybrid devices containing nanowires with topologically nontrivial superconducting phases.

ACKNOWLEDGMENTS

We thank L. Arrachea and T. Martin for discussions. This project has been funded by the Deutsche Forschungsgemeinschaft under Germany's Excellence Strategy, Cluster of Excellence Matter and Light for Quantum Computing (ML4Q) EXC Grant No. 2004/1-390534769; by the Spanish Ministry of Economy, Industry, and Competitiveness through Grant No. FIS2017-84860-R; and by the María de Maeztu Programme for Units of Excellence in Research and Development Grant No. MDM-2014-0377.

APPENDIX A: SPINFUL SINGLE-CHANNEL MODEL

In this Appendix, we provide technical details pertaining to our discussion of the spinful single-channel Majorana wire model [68,69] in Sec. II. First, the explicit form of the coefficients $C_n(\omega)$ in Eq. (14) is given by

$$\begin{aligned}
C_0 &= \frac{3\alpha^4}{8} + \Delta^4 + \mu^4 - 8\mu^3 t + 36\mu^2 t^2 - 80\mu t^3 \\
&\quad + 70t^4 - 2\mu^2 V_x^2 + 8\mu t V_x^2 - 12t^2 V_x^2 V_x^4 \\
&\quad - 2\big(\mu^2 - 4\mu t + 6t^2 + V_x^2\big)\omega^2 + \omega^4 \\
&\quad + 2\Delta^2\big(\mu^2 - 4\mu t + 6t^2 - V_x^2 - \omega^2\big) \\
&\quad + \alpha^2\big[\Delta^2 - \mu^2 + 4\mu t - 5t^2 + V_x^2 - \omega^2\big], \\
C_1 &= -(\mu - 2t)t\big[\alpha^2 - 4\big(\Delta^2 + \mu^2 - 4\mu t \\
&\quad + 7t^2 - V_x^2 - \omega^2\big)\big], \\
C_2 &= \big\{-\alpha^4 + 8t^2\big(\Delta^2 + 3\mu^2 - 12\mu t + 14t^2 - V_x^2 - \omega^2\big) \\
&\quad + 2\alpha^2\big[-\Delta^2 + (\mu - 2t)^2 - V_x^2 + \omega^2\big]\big\}/4, \\
C_3 &= (t\mu - 2t^2)(\alpha^2 + 4t^2), \quad C_4 = [t^2 + (\alpha/2)^2]^2. \qquad \text{(A1)}
\end{aligned}$$

It is convenient to renormalize these coefficients such that C_4 appears as a common factor of the polynomial.

The C_n coefficients in turn determine the coefficients $a_m(\omega)$ appearing in the eighth-order polynomial equation (15). The roots $z_n(\omega)$ therefore have to satisfy the Vieta relations

$$\begin{aligned}
S_k(z_1, \ldots, z_8) &= \sum_{i_1 < i_2 < \cdots < i_k} z_{i_1} z_{i_2} \cdots z_{i_k} \\
&= (-1)^{8-k} \frac{a_k}{a_8}. \qquad \text{(A2)}
\end{aligned}$$

Using the condition (20) and the ansatz (19), the first three invariants are given by $S_1 = 2AB$, $S_2 = 2(A^2 - 2)(1 + C) + 4B^2$, and $S_3 = 2AB(A^2 - 1) + 4ABC$ with

$$\begin{aligned}
A &= 1 - \eta + \frac{1}{1 - \eta}, \quad B = \cos(\delta_1) + \cos(\delta_2), \\
C &= 2\cos(\delta_1)\cos(\delta_2). \qquad \text{(A3)}
\end{aligned}$$

As a consequence, the parameter C obeys a cubic equation that can be solved analytically,

$$w_3 + w_2 C + w_1 C^2 + C^3 = 0, \qquad \text{(A4)}$$

with the coefficients

$$\begin{aligned}
w_1 &= 1 - \frac{S_3}{S_1}, \\
w_2 &= \frac{S_2}{4} - \frac{S_3}{S_1} - \frac{1}{4} + \left(\frac{S_3}{2S_1}\right)^2, \\
w_3 &= -\frac{S_2 S_3}{8S_1} - \frac{S_2}{8} + S_1^2 - \frac{1}{4} + \left(\frac{S_3}{2S_1}\right)^2. \qquad \text{(A5)}
\end{aligned}$$

For $V_x < V_c$, the physical solution of Eq. (A5) is given by

$$C = -2\sqrt{-Q}\cos(\theta_0/3) - w_1/3, \qquad \text{(A6)}$$

with

$$\begin{aligned}
\theta_0 &= \cos^{-1}\left(-\frac{R}{\sqrt{-Q^3}}\right), \\
Q &= \frac{3a_2 - w_1^2}{9}, \\
R &= \frac{9w_1 w_2 - 27w_3 - 2w_1^3}{54}. \qquad \text{(A7)}
\end{aligned}$$

For $V_x > V_c$, the solution is given by $C = P_1 - Q/P_1 - w_1/3$ (assuming $P_1 \neq 0$), with

$$P_1 = \mathrm{sgn}(R)(|R| + \sqrt{R^2 + Q^3})^{1/3}. \qquad \text{(A8)}$$

The coefficients A and B then follow from

$$A^2 = \frac{S_3}{S_1} + 1 - 2C, \quad B = \frac{S_1}{2A}. \qquad \text{(A9)}$$

Finally, the parameters in our ansatz [see Eqs. (19) and (21)] can be determined from the relations

$$\begin{aligned}
\cos\delta_1 &= \frac{B + \sqrt{B^2 - 2C}}{2}, \\
\cos\delta_2 &= \frac{B - \sqrt{B^2 - 2C}}{2}, \\
\eta &= 1 - \frac{A}{2} + \sqrt{\frac{A^2}{4} - 1}. \qquad \text{(A10)}
\end{aligned}$$

We proceed by providing the detailed form of the matrices $\hat{A}_\nu$ and $\hat{A}'_\nu$ in Eq. (25). Using the definition in the main text, for $V_x < V_c$, they are with $z_\nu(\omega)$ in Eq. (19) given by

$$\hat{A}_\nu = \frac{\hat{A}(z_\nu)}{b_\nu} + \frac{\hat{A}(z_\nu^*)}{b_\nu^*}, \quad \hat{A}'_\nu = \frac{\hat{A}'(z_\nu)}{b_\nu} + \frac{\hat{A}'(z_\nu^*)}{b_\nu^*}, \tag{A11}$$

where an expansion of $\prod_{z_\nu \neq z_m}(z_\nu - z_m)$ to first order in $\tau_\nu\sqrt{\Delta_\nu^2 - \omega^2}$ yields

$$b_\nu = 32e^{3i\delta_\nu}\tau_\nu \sin^2(\delta_\nu)[\cos(\delta_2) - \cos(\delta_1)]^2. \tag{A12}$$

Explicitly, the components of the symmetric 4×4 matrix $\hat{A}$ in Eq. (A11), $\hat{A}_{ij} = \hat{A}_{ji}$, follow from

$$\begin{aligned}
\hat{A}_{11}(z) &= -\hat{A}_{33}(z) = z^3V_x^2[\epsilon(z) - \tilde{\alpha}(z)] \\
&\quad + z^3[\epsilon(z) + \tilde{\alpha}(z)]\{-\Delta^2 - [\epsilon(z) - \tilde{\alpha}(z)]^2\}, \\
\hat{A}_{22}(z) &= -\hat{A}_{44}(z) = z^3V_x^2[\epsilon(z) + \tilde{\alpha}(z)] \\
&\quad + z^3[\epsilon(z) - \tilde{\alpha}(z)]\{-\Delta^2 - [\epsilon(z) + \tilde{\alpha}(z)]^2\}, \\
\hat{A}_{12}(z) &= \hat{A}_{34}(z) = z^3V_x\left[\Delta^2 + \epsilon^2(z) - \tilde{\alpha}^2(z) - V_x^2\right], \\
\hat{A}_{13}(z) &= z^3\Delta\left\{V_x^2 - \Delta^2 - [\epsilon(z) - \tilde{\alpha}(z)]^2\right\}, \\
\hat{A}_{14}(z) &= -\hat{A}_{23}(z) = 2z^3V_x\Delta\tilde{\alpha}(z), \\
\hat{A}_{24}(z) &= z^3\Delta\left\{V_x^2 - \Delta^2 - [\epsilon(z) + \tilde{\alpha}(z)]^2\right\}.
\end{aligned} \tag{A13}$$

Similarly, by taking a derivative with respect to ω, the nonvanishing matrix elements of the symmetric matrix $\hat{A}'_{ij} = \hat{A}'_{ji}$ follow as

$$\begin{aligned}
\hat{A}'_{11}(z) &= \hat{A}'_{33}(z) = -z^3\left\{\Delta^2 + [\epsilon(z) - \alpha(z)]^2 + V_x^2\right\}, \\
\hat{A}'_{22}(z) &= \hat{A}'_{44}(z) = -z^3\left\{\Delta^2 + [\epsilon(z) + \alpha(z)]^2 + V_x^2\right\}, \\
\hat{A}'_{12}(z) &= -\hat{A}'_{34}(z) = 2z^3V_x\epsilon(z), \\
\hat{A}'_{14}(z) &= \hat{A}'_{23}(z) = 2z^3V_x\Delta.
\end{aligned} \tag{A14}$$

In the topologically nontrivial phase, $V_x > V_c$, trigonometric functions associated with the roots $z_{1,\pm}$ in Eq. (21) turn into hyperbolic functions. The matrices with $\nu = 1$ in Eq. (A11) are then replaced by

$$\begin{aligned}
\hat{A}_1 &= \frac{\hat{A}(z_{1,+})}{\tilde{b}_1} - \frac{\hat{A}(z_{1,-})}{\tilde{b}_1}, \\
\hat{A}'_1 &= \frac{\hat{A}'(z_{1,+})}{\tilde{b}_1} - \frac{\hat{A}'(z_{1,-})}{\tilde{b}_1},
\end{aligned} \tag{A15}$$

with the quantities

$$\begin{aligned}
\tilde{b}_1 &= 32e^{-3\delta_1}\tau_1 \sinh^2(\delta_1)[\cos(\delta_2) - \cosh(\delta_1)]^2, \\
\tilde{b}_2 &= 32e^{3i\delta_2}\tau_2 \sin^2(\delta_2)[\cos(\delta_2) - \cosh(\delta_1)]^2.
\end{aligned} \tag{A16}$$

The $\nu = 2$ matrices follow from Eq. (A11) with the replacement $b_2 \to \tilde{b}_2$. Finally, we note that for very large V_x one approaches the Kitaev limit of the nanowire, and the relevant residues come from the z_2 roots only.

APPENDIX B: TRITOPS WIRES

According to Theorem 1 of Ref. [76], the largest-modulus root $z_{\max}$ inside the unit circle can be determined from the relative position of the origin inside the ellipse discussed in Sec. V A. For that purpose, we first determine the major (M) and minor (m) axes of the ellipse in Fig. 5. Using Eq. (34) and focusing on the case of $\hat{\mathcal{H}}_-(k)$, the defining equation of the ellipse is given by

$$B^T\begin{pmatrix} (t^2 + \alpha^2)/\Delta^2 & t/\Delta \\ t/\Delta & 1 \end{pmatrix}B = 4\alpha^2 \tag{B1}$$

with $B^T = (\beta_{-,x}, \beta_{-,z} + \mu)$. From the eigenvalues of the 2×2 matrix in Eq. (B1),

$$\lambda_\pm = \frac{t^2 + \Delta^2 + \alpha^2}{2\Delta^2} \pm \frac{\sqrt{(t^2 + \Delta^2)^2 + 2(t^2 - \Delta^2)\alpha^2 + \alpha^4}}{2\Delta^2}, \tag{B2}$$

we obtain

$$m = 4\alpha/\sqrt{\lambda_+}, \quad M = 4\alpha/\sqrt{\lambda_-}. \tag{B3}$$

The distance between the foci of the ellipse then follows as $f = \sqrt{M^2 - m^2}$.

To obtain the distance $l = |OF_1| + |OF_2|$ between the foci and the origin (corresponding to the red dashed line in Fig. 5), we first compute the rotation angle θ of the ellipse using the eigenvectors of the conic section matrix:

$$\begin{aligned}
\cos\theta &= \frac{1}{\sqrt{1 + X^2/(2t\Delta)^2}}, \\
X &= \Delta^2 - t^2 - \alpha^2 \\
&\quad - \sqrt{(t^2 + \Delta^2)^2 + 2(t^2 - \Delta^2)\alpha^2 + \alpha^4}.
\end{aligned} \tag{B4}$$

As a consequence, l follows from the relation

$$|OF_{1,2}| = \sqrt{(f/2)^2 + \mu^2 \pm \mu f \sin\theta}. \tag{B5}$$

The largest-modulus root inside the unit circle is then given by (see Refs. [76,77])

$$|z_{\max}| = \frac{l + \sqrt{l^2 - f^2}}{M + m}. \tag{B6}$$

The same result follows for the other block, $\hat{\mathcal{H}}_+(k)$. As discussed in Sec. V A, Eq. (B6) determines the decay length of Majorana end states into the bulk of a TRITOPS wire.

[1] J. Alicea, Rep. Prog. Phys. **75**, 076501 (2012).
[2] M. Leijnse and K. Flensberg, Semicond. Sci. Technol. **27**, 124003 (2012).
[3] C. W. J. Beenakker, Annu. Rev. Condens. Matter Phys. **4**, 113 (2013).
[4] S. Das Sarma, M. Freedman, and C. Nayak, npj Quantum Inf. **1**, 15001 (2015).
[5] R. Aguado, Riv. Nuovo Cimento **40**, 523 (2017).
[6] M. Sato and Y. Ando, Rep. Prog. Phys. **80**, 076501 (2017).
[7] R. M. Lutchyn, E. P. A. M. Bakkers, L. P. Kouwenhoven, P. Krogstrup, C. M. Marcus, and Y. Oreg, Nat. Rev. Mater. **3**, 52 (2018).
[8] H. Zhang, D. E. Liu, M. Wimmer, and L. P. Kouwenhoven, Nat. Commun. **10**, 5128 (2019).

[9] V. Mourik, K. Zuo, S. M. Frolov, S. R. Plissard, E. P. A. Bakkers, and L. P. Kouwenhoven, Science **336**, 1003 (2012).
[10] S. M. Albrecht, A. P. Higginbotham, M. Madsen, F. Kuemmeth, T. S. Jespersen, J. Nygård, P. Krogstrup, and C. M. Marcus, Nature (London) **531**, 206 (2016).
[11] M. T. Deng, S. Vaitiekenas, E. B. Hansen, J. Danon, M. Leijnse, K. Flensberg, J. Nygård, P. Krogstrup, and C. M. Marcus, Science **354**, 1557 (2016).
[12] F. Nichele, A. C. C. Drachmann, A. M. Whiticar, E. C. T. O'Farrell, H. J. Suominen, A. Fornieri, T. Wang, G. C. Gardner, C. Thomas, A. T. Hatke, P. Krogstrup, M. J. Manfra, K. Flensberg, and C. M. Marcus, Phys. Rev. Lett. **119**, 136803 (2017).
[13] H. J. Suominen, M. Kjaergaard, A. R. Hamilton, J. Shabani, C. J. Palmstrøm, C. M. Marcus, and F. Nichele, Phys. Rev. Lett. **119**, 176805 (2017).
[14] S. Gazibegovich, D. Car, H. Zhang, S. C. Balk, J. A. Logan, M. W. A. de Moor, M. C. Cassidy, R. Schmits, D. Xu, G. Wang, P. Krogstrup, R. L. M. Op het Veld, J. Shen, D. Bouman, B. Shojaei, D. Pennachio, J. S. Lee, P. J. van Veldhoven, S. Koelling, M. A. Verheijen, L. P. Kouwenhoven, C. J. Palmstrøm, and E. P. A. M. Bakkers, Nature (London) **548**, 434 (2017).
[15] H. Zhang, C. X. Liu, S. Gazibegovic, D. Xu, J. A. Logan, G. Wang, N. van Loo, J. D. S. Bommer, M. W. A. de Moor, D. Car, R. L. M. Op het Veld, P. J. van Veldhoven, S. Koelling, M. A. Verheijen, M. Pendharkar, D. J. Pennachio, B. Shojaei, J. S. Lee, C. J. Palmstrom, E. P. A. M. Bakkers, S. Das Sarma, and L. P. Kouwenhoven, Nature (London) **556**, 74 (2018).
[16] A. Fornieri, A. M. Whiticar, F. Setiawan, E. P. Marín, A. C. C. Drachmann, A. Keselman, S. Gronin, C. Thomas, T. Wang, R. Kallaher, G. C. Gardner, E. Berg, M. J. Manfra, A. Stern, C. M. Marcus, and F. Nichele, Nature (London) **569**, 89 (2019).
[17] S. Vaitiekenas, M. T. Deng, P. Krogstrup, and C. M. Marcus, arXiv:1809.05513.
[18] C. L. M. Wong and K. T. Law, Phys. Rev. B **86**, 184516 (2012).
[19] S. Nakosai, Y. Tanaka, and N. Nagaosa, Phys. Rev. Lett. **108**, 147003 (2012).
[20] S. Deng, L. Viola, and G. Ortiz, Phys. Rev. Lett. **108**, 036803 (2012).
[21] F. Zhang, C. L. Kane, and E. J. Mele, Phys. Rev. Lett. **111**, 056402 (2013).
[22] A. Keselman, L. Fu, A. Stern, and E. Berg, Phys. Rev. Lett. **111**, 116402 (2013).
[23] E. Dumitrescu and S. Tewari, Phys. Rev. B **88**, 220505(R) (2013).
[24] S. B. Chung, J. Horowitz, and X.-L. Qi, Phys. Rev. B **88**, 214514 (2013).
[25] S. Nakosai, J. C. Budich, Y. Tanaka, B. Trauzettel, and N. Nagaosa, Phys. Rev. Lett. **110**, 117002 (2013).
[26] A. Haim, A. Keselman, E. Berg, and Y. Oreg, Phys. Rev. B **89**, 220504(R) (2014).
[27] E. Gaidamauskas, J. Paaske, and K. Flensberg, Phys. Rev. Lett. **112**, 126402 (2014).
[28] J. Klinovaja, A. Yacoby, and D. Loss, Phys. Rev. B **90**, 155447 (2014).
[29] C. Schrade, A. A. Zyuzin, J. Klinovaja, and D. Loss, Phys. Rev. Lett. **115**, 237001 (2015).
[30] A. Haim, E. Berg, K. Flensberg, and Y. Oreg, Phys. Rev. B **94**, 161110(R) (2016).
[31] Y. Kim, D. E. Liu, E. Gaidamauskas, J. Paaske, K. Flensberg, and R. M. Lutchyn, Phys. Rev. B **94**, 075439 (2016).
[32] E. Mellars and B. Béri, Phys. Rev. B **94**, 174508 (2016).
[33] A. Camjayi, L. Arrachea, A. Aligia, and F. von Oppen, Phys. Rev. Lett. **119**, 046801 (2017).
[34] C. Schrade and L. Fu, Phys. Rev. Lett. **120**, 267002 (2018).
[35] A. Haim and Y. Oreg, Phys. Rep. **825**, 1 (2019).
[36] L. Tosi, C. Metzger, M. F. Goffman, C. Urbina, H. Pothier, Sunghun Park, A. L. Yeyati, J. Nygård, and P. Krogstrup, Phys. Rev. X **9**, 011010 (2019).
[37] K. Flensberg, Phys. Rev. B **82**, 180516(R) (2010).
[38] M. Leijnse and K. Flensberg, Phys. Rev. B **84**, 140501(R) (2011).
[39] S. Das Sarma, J. D. Sau, and T. D. Stanescu, Phys. Rev. B **86**, 220506(R) (2012).
[40] E. Prada, P. San-Jose, and R. Aguado, Phys. Rev. B **86**, 180503(R) (2012).
[41] D. Rainis, L. Trifunovic, J. Klinovaja, and D. Loss, Phys. Rev. B **87**, 024515 (2013).
[42] T. D. Stanescu and S. Tewari, J. Phys.: Condens. Matter **25**, 233201 (2013).
[43] J. Cayao, E. Prada, P. San-Jose, and R. Aguado, Phys. Rev. B **91**, 024514 (2015).
[44] T. D. Stanescu and S. Das Sarma, Phys. Rev. B **97**, 045410 (2018).
[45] Y. Huang, J. D. Sau, T. D. Stanescu, and S. Das Sarma, Phys. Rev. B **98**, 224512 (2018).
[46] C. Reeg, O. Dmytruk, D. Chevallier, D. Loss, and J. Klinovaja, Phys. Rev. B **98**, 245407 (2018).
[47] A. E. G. Mikkelsen, P. Kotetes, P. Krogstrup, and K. Flensberg, Phys. Rev. X **8**, 031040 (2018).
[48] A. E. Antipov, A. Bargerbos, G. W. Winkler, B. Bauer, E. Rossi, and R. M. Lutchyn, Phys. Rev. X **8**, 031041 (2018).
[49] S. D. Escribano, A. Levy Yeyati, Y. Oreg, and E. Prada, Phys. Rev. B **100**, 045301 (2019).
[50] G. W. Winkler, A. E. Antipov, B. van Heck, A. A. Soluyanov, L. I. Glazman, M. Wimmer, and R. M. Lutchyn, Phys. Rev. B **99**, 245408 (2019).
[51] A. Haim and A. Stern, Phys. Rev. Lett. **122**, 126801 (2019).
[52] A. R. Akhmerov, J. P. Dahlhaus, F. Hassler, M. Wimmer, and C. W. J. Beenakker, Phys. Rev. Lett. **106**, 057001 (2011).
[53] F. Pientka, G. Kells, A. Romito, P. W. Brouwer, and F. von Oppen, Phys. Rev. Lett. **109**, 227006 (2012).
[54] M. Houzet, J. S. Meyer, D. M. Badiane, and L. I. Glazman, Phys. Rev. Lett. **111**, 046401 (2013).
[55] P. A. Ioselevich, P. M. Ostrovsky, and M. V. Feigel'man, Phys. Rev. B **93**, 125435 (2016).
[56] F. Setiawan, W. S. Cole, J. D. Sau, and S. Das Sarma, Phys. Rev. B **95**, 174515 (2017).
[57] C. Reeg and D. L. Maslov, Phys. Rev. B **95**, 205439 (2017).
[58] E. Nakhmedov, B. D. Suleymanli, O. Z. Alekperov, F. Tatardar, H. Mammadov, A. A. Konovko, A. M. Saletsky, Yu. M. Shukrinov, K. Sengupta, and B. Tanatar, arXiv:1911.09289.
[59] A. Zazunov, R. Egger, and A. Levy Yeyati, Phys. Rev. B **94**, 014502 (2016).
[60] Y. Peng, Y. Bao, and F. von Oppen, Phys. Rev. B **95**, 235143 (2017).
[61] A. Zazunov, R. Egger, M. Alvarado, and A. L. Yeyati, Phys. Rev. B **96**, 024516 (2017).
[62] A. Komnik and S. Heinze, Phys. Rev. B **96**, 155103 (2017).

[63] A. Zazunov, A. Iks, M. Alvarado, A. Levy Yeyati, and R. Egger, Beilstein J. Nanotechn. **9**, 1659 (2018).
[64] M. Istas, C. Groth, and X. Waintal, Phys. Rev. Research **1**, 033188 (2019).
[65] A. M. Essin and V. Gurarie, Phys. Rev. B **84**, 125132 (2011).
[66] X.-L. Qi, T. L. Hughes, and S.-C. Zhang, Phys. Rev. B **81**, 134508 (2010).
[67] S. Tewari and J. D. Sau, Phys. Rev. Lett. **109**, 150408 (2012).
[68] R. M. Lutchyn, J. D. Sau, and S. Das Sarma, Phys. Rev. Lett. **105**, 077001 (2010).
[69] Y. Oreg, G. Refael, and F. von Oppen, Phys. Rev. Lett. **105**, 177002 (2010).
[70] S. Park and A. L. Yeyati, Phys. Rev. B **96**, 125416 (2017).
[71] L. Arrachea, G. S. Lozano, and A. A. Aligia, Phys. Rev. B **80**, 014425 (2009).
[72] I. C. Fulga, F. Hassler, and A. R. Akhmerov, Phys. Rev. B **85**, 165409 (2012).
[73] See Supplemental Material at http://link.aps.org/supplemental/10.1103/PhysRevB.101.094511 for two movies that illustrate the motion of the roots in the complex plane. The first movie refers to a single-channel wire with varying ratio V_x/V_c for the parameters in Figs. 2(a) and 2(b). The second movie is for the two-channel case with varying chemical potential μ using the parameters in Fig. 4.
[74] R. M. Lutchyn, T. D. Stanescu, and S. Das Sarma, Phys. Rev. Lett. **106**, 127001 (2011).
[75] B. D. Woods, J. Chen, S. M. Frolov, and T. D. Stanescu, Phys. Rev. B **100**, 125407 (2019).
[76] R. S. K. Mong and V. Shivamoggi, Phys. Rev. B **83**, 125109 (2011).
[77] A. A. Aligia and L. Arrachea, Phys. Rev. B **98**, 174507 (2018).
[78] J. Alicea, Y. Oreg, G. Refael, F. von Oppen, and M. P. A. Fisher, Nat. Phys. **7**, 412 (2011).
[79] O. Deb, K. Sengupta, and D. Sen, Phys. Rev. B **97**, 174518 (2018).
[80] M. Trif and P. Simon, Phys. Rev. Lett. **122**, 236803 (2019).
[81] L. Peralta Gavensky, G. Usaj, and C. A. Balseiro, Phys. Rev. B **100**, 014514 (2019).
[82] J. S. Meyer and M. Houzet, arXiv:1911.07705.
[83] T. Jonckheere, J. Rech, A. Zazunov, R. Egger, A. L. Yeyati, and T. Martin, Phys. Rev. Lett. **122**, 097003 (2019).
[84] P. Wei, S. Manna, M. Eich, P. Lee, and J. Moodera, Phys. Rev. Lett. **122**, 247002 (2019).
[85] In the limit $\mu \to 0$, there is an appreciable canting angle in the TS lead [61] which transforms $\hat{\Psi}_R$ and requires one to include higher-order processes. For $V_x \to V_c$, we then find that φ_0-junction behavior is possible, with a finite supercurrent at $\phi = 0$. Moreover, higher-order processes may also cause an effective hybridization of the Majorana-Kramers pair in the TRITOPS wire. This fact explains the sinusoidal dispersion of the Andreev bound states for $\theta = \pi/2$ in Fig. 11(c).

Selbstständigkeitserklärung

Ich versichere and Eides Statt, dass die Dissertation von mir selbstständig und ohne unzulässige fremde Hilfe unter Beachtung der "Grundsätze zur Sicherung guter wisserschaftlicher Praxis an der Heinrich-Heine-Universität Düsseldorf" erstellt worden ist. Weiterhin erkläre ich, dass ich die Dissertation keiner anderen Fakultät bereits vorgelegt habe und keinerlei vorherige erfolglose Promotionsversuche vorliegen. Darüber hinaus ist mir bekannt, dass jedweder Betrugsversuch zum Nichtbestehen oder zur Aberkennung der Prüfungsleistung führen kann.

Düsseldorf, den

(Albert Iks)